

DISS. ETH No. 26120

**The two-dimensional polymerization mechanism
of an anthracene-based monomer:
A single-crystal-to-single-crystal transformation
investigated via total X-ray scattering.**

A thesis submitted to attain the degree of
DOCTOR OF SCIENCES of ETH ZURICH
(Dr. Sc. ETH Zurich)

presented by

GREGOR HOFER

MSc., Universität Wien

born on 14.01.1988

citizen of Austria

Accepted on the recommendation of

Prof. Dr. Martin Kröger (examiner)

Dr. Thomas Weber (co-examiner)

Prof. Dr. A. Dieter Schlüter (co-examiner)

Prof. Dr. Athina Anastasaki (co-examiner)

Dr. Michael Dieter Wörle (co-examiner)

2019

I was captured for life by
chemistry and by crystals.

DOROTHY HODGKIN

Abstract

Two-dimensional polymerization is a recent advance in polymer chemistry. Using the anthracene-based trifunctional monomer studied in this thesis as an example, two-dimensional polymerization is achieved by pre-organizing the monomer molecules through crystallization in a layered and *reactive packaging*. The reactive packing enables pairs of anthracene blades from adjacent molecules to face each other. Exposition of the crystal to intense blue light triggers and drives a thermally reversible photochemical reaction, thereby achieving true long-range ordered, two-dimensional polymerization through the gradual formation of anthracene dimers between individual monomer molecules. Understanding the propagation mechanisms of two-dimensional polymerization and depolymerization of these single-crystal-to-single-crystal transformations is of crucial importance for fundamental and applied research. Both processes can be suspended at any point by removing the crystal from the triggering source, resulting in X-ray hard partially polymerized crystal structures. Monomer, polymer and intermediate states were investigated using standard X-ray diffraction methods and by analyzing the diffuse X-ray scattering. The first utilizes Bragg scattering to obtain the average crystal structures, while the second uses the three-dimensional difference pair-distribution function method to study characteristics of the real crystal structures. These experiments showed that polymerization and depolymerization propagate predominantly in a random fashion, with a preference of having anthracene dimers surrounded by pairs of anthracene blades.

The properties of the average structures of the monomer, polymer, and all intermediate states were analyzed as a function of the conversion ratio. All investigated crystal structures are described in space group $R3$. The axes of the unit-cell show a particularly interesting behavior. Upon complete polymerization, the a - and c -axes have increased by about 0.15 \AA and 0.30 \AA compared to the monomer. During the first heat treatment step to induce and advance the depolymerization reaction, the a -axis expands by about 0.05 \AA , while the c -axis shrinks substantially by about 1.05 \AA . When depolymerization continues, the a -axis decreases, while the c -axis increases, and when complete depolymerization is achieved, they are of almost the same size as in the original monomer crystal.

In order to understand the propagation mechanism, it is necessary to gain knowledge about the changes in the real structure, as this provides, among other things, the spatial distribution of the dimers in the crystal during polymerization. Typically, standard X-ray diffraction experiments are not able to provide such insights. However, results from the reaction kinetics, derived from the detailed analysis of the average structure of multiple intermediate states were utilized to obtain a basic understanding of the polymerization and depolymerization propagation mechanisms. These results are interpreted using the Schmidt rules for photochemistry. They state that the reaction probability between photoreactive units is inversely related to the distance between these units. During polymerization, the distance between the unreacted anthracene blades increases by approximately 0.2 \AA , which leads to the aforementioned random propagation where anthracene dimers prefer to be surrounded by unreacted anthracene pairs. In analogy to polymerization, depolymerization propagates in a similar fashion by anthracene dimers breaking up and thereby isolating dimers from other dimers. The isolation is achieved by local stress reduction through the breaking of bonds, which increases the stability of the dimers in the immediate environment. The result of polymerization and depolymerization were supported by the *Avrami* formalism and could be modeled with Monte Carlo simulations.

The evaluation of the diffuse scattering with the three-dimensional difference pair-distribution function method provided additional insights into the real structure. Its structural properties can be expressed by correlated atomic displacements and correlated atomic substitutions. The first indicate a form of interaction between molecules, while the second describe the distribution of dimers in the crystal at a given conversion ratio. The results from analyzing the diffuse scattering confirmed the findings of the average structure analysis but provided a more detailed view on the distribution of dimers. This showed that a dimer influences the reaction probabilities of anthracene pairs up to its third neighborhood, about 45 \AA away, within the same layer. In addition, dimerization within a layer also influences the reaction probabilities of anthracene pairs in adjacent layers, making two-dimensional polymerization a three-dimensional process.

The combined results from the average and real structure analysis also showed the crucial importance of mechanisms that reduce stress during polymer growth and thus promote two-dimensional polymerization. Of particular

importance is the mobility and the flexibility of the template and solvent molecules incorporated into the structure. Stress relief is achieved by movements of the template along the c -axis and by realignment of some solvent molecules sandwiched between the layers. The correlations of the displacive disorder between the template and the monomer/polymer moieties increase with increasing conversion ratio, indicating that the template loses its ability to dissipate local stress. In addition, the found polymerization and depolymerization mechanisms do not exhibit pronounced reaction fronts. This is fortunate, because such a front would be a domain boundary that could either drastically reduce the achievable sheet size, deform the crystal lattice in such a way that (de-)polymerization propagation is prevented, or destroy the crystal by stress build-up at the reaction front.

This work presents the first detailed structural investigation of the recently discovered two-dimensional polymerization process in single-crystals. This work also contributes to the further development of the three-dimensional difference pair-distribution function method, which was able to model the complex phase transformation from monomer to polymer.

Riepilogo

Un recente progresso nella chimica dei polimeri è la polimerizzazione bidimensionale. Utilizzando il monomero trifunzionale antracenetico studiato in questa tesi, la polimerizzazione bidimensionale si ottiene preorganizzando le molecole di monomero attraverso la cristallizzazione in un imballaggio stratificato e *reattivo*. L'imballaggio reattivo permette a coppie di lame di antracene di molecole adiacenti di fronteggiarsi. L'esposizione del cristallo alla luce blu intenso innesca e alimenta una reazione fotochimica termicamente reversibile, consentendo di ottenere una polimerizzazione bidimensionale realmente dotata di ordine a lungo raggio a lungo raggio attraverso la graduale formazione di dimeri di antracene tra le singole molecole monomero. La comprensione dei meccanismi di propagazione della Polimerizzazione e depolimerizzazione bidimensionale di queste trasformazioni da monocristallo a monocristallo è di cruciale importanza per la ricerca fondamentale e applicata. Entrambi i processi possono essere sospesi in qualsiasi punto rimuovendo il cristallo dalla sorgente di innesco, ottenendo così stati intermedi resistenti ai raggi X tra il monomero e le strutture cristalline polimeriche. I monomeri, i polimeri e gli stati intermedi sono stati studiati utilizzando metodi standard di diffusione dei raggi X e analizzando la distribuzione dei raggi X diffusi dal materiale. Nel primo caso si utilizza la diffusione di Bragg (i.e. Bragg scattering) per ottenere Per ottenere informazioni riguardo alla struttura cristallina tipica utilizza. Il metodo del differenziale tridimensionale della funzione di distribuzione delle coppie per studiare le caratteristiche delle strutture cristalline reali durante la polimerizzazione e la depolimerizzazione. Questi esperimenti hanno dimostrato che la polimerizzazione e la depolimerizzazione si propagano prevalentemente a caso, con una preferenza per strutture formate da dimeri di antracene circondati da coppie di lame di antracene.

Le proprietà Della struttura tipica del monomero, del polimero e di tutti gli stati intermedi sono state analizzate in funzione al rapporto di conversione tra monomero e polimero. Tutte le strutture cristalline indagate appartengono al gruppo spaziale $R3$. Gli assi della cella-unitaria mostrano un comportamento particolarmente interessante. Con la polimerizzazione completa, gli assi a e c sono aumentati di circa 0.15 \AA e 0.30 \AA . Durante la prima fase del trattamento termico per indurre e far avanzare la reazione di de-

polimerizzazione, l'asse a -si espande di circa 0.05 \AA , mentre l'asse c -si riduce sostanzialmente di circa 1.05 \AA . Al procedere della depolimerizzazione, l'asse a diminuisce, mentre l'asse c aumenta, e quando si ottiene la depolimerizzazione completa, gli assi hanno circa le stesse dimensioni del cristallo di monomeri originario.

Per comprendere il meccanismo di propagazione, è necessario conoscere i cambiamenti nella struttura reale, in quanto questo fornisce, tra l'altro, la distribuzione spaziale dei dimeri nel cristallo durante la polimerizzazione. Tipicamente, gli esperimenti standard di diffrazione a raggi X non sono in grado di fornire tali informazioni. Tuttavia risultati dai dati sulla cinetica di reazione di reazione derivati dall'analisi dettagliata della struttura tipica di stati intermedi multipli sono stati utilizzati per ottenere una comprensione di base dei meccanismi di propagazione di polimerizzazione e depolimerizzazione. Questi risultati sono interpretati utilizzando le regole di Schmidt per la fotochimica, accettate a livello internazionale. Esse affermano che la probabilità di reazione tra unità fotoreattive è inversamente correlata alla distanza tra queste unità. Durante la polimerizzazione, la distanza tra le lame di antracene non reagito aumenta di circa 0.2 \AA , il che porta alla suddetta propagazione casuale in cui i dimeri di antracene preferiscono essere circondati da coppie di antracene non reagito. In analogia alla polimerizzazione, la depolimerizzazione si propaga per mezzo di dimeri di antracene che si spezzano e quindi isolano i dimeri da altri dimeri. L'isolamento si ottiene attraverso la riduzione dello stress locale legato alla rottura dei legami, che aumenta la stabilità dei dimeri nell'ambiente circostante. I risultati sulla polimerizzazione e sono stati supportati dal formalismo *Avrami* e potrebbero essere modellati con le simulazioni Monte Carlo.

La valutazione dello scattering diffuso, effettuata con il metodo del differenziale tridimensionale della funzione di distribuzione delle coppie, ha fornito ulteriori approfondimenti sulla struttura reale. Le sue proprietà strutturali possono essere espresse da spostamenti atomici correlati e sostituzioni atomiche correlate. I primi indicano una forma di interazione tra le molecole, mentre le seconde descrivono la distribuzione dei dimeri nel cristallo ad un dato rapporto di conversione. I risultati ottenuti dall'analisi dello scattering diffuso hanno confermato i risultati Riguardanti la struttura tipica, ma hanno fornito una visione più dettagliata della distribuzione dei dimeri. Questo ha mostrato che un dimero influenza le probabilità di reazione dell'antracene

fino al suo terzo prossimo, a circa 45 Å di distanza all'interno dello stesso strato. Inoltre, la dimerizzazione all'interno di uno strato influenza le probabilità di reazione delle coppie di antracene negli strati adiacenti, rendendo la polimerizzazione bidimensionale un processo tridimensionale.

Combinati, i risultati sulle strutture tipica e reale hanno mostrato anche l'importanza cruciale dei meccanismi che riducono gli sforzi formati durante la crescita del polimero e che quindi supportano la polimerizzazione bidimensionale. Di particolare importanza sono la mobilità e la flessibilità della struttura di supporto e delle molecole di solvente incorporate nella struttura stessa. Il rilascio degli sforzi è ottenuto attraverso movimenti della struttura di supporto lungo c e dall'inserimento di alcune molecole di solvente tra gli strati ottenuto grazie al riallineamento. Le correlazioni del disordine dislocante tra il supporto e i moti del monomero/polimero aumentano con l'aumentare del rapporto di conversione, indicando che il supporto perde la sua capacità di dissipare gli sforzi locali. Inoltre, i meccanismi di polimerizzazione e depolimerizzazione trovati non presentano fronti di reazione pronunciati. Questo è un caso fortunato, perché un tale fronte sarebbe un confine di dominio che potrebbe ridurre drasticamente le dimensioni dello strato raggiungibile, deformando il reticolo cristallino in modo tale da impedire la propagazione della (de-)polimerizzazione, o distruggendo il cristallo per accumulo di sforzi sul fronte di reazione.

In sintesi, questo lavoro presenta la prima indagine strutturale sostanziale del recentemente scoperto processo di polimerizzazione bidimensionale in monocristalli. Questo lavoro contribuisce anche all'ulteriore sviluppo del metodo del differenziale tridimensionale della funzione di distribuzione delle coppie, che è stato in grado di modellare la complessa trasformazione di fase da monomero a polimero.

Acknowledgements

First of all I would like to thank **Thomas Weber** for his support over all these years and for all his guidance. Thank you for the all insights you gave me for understanding science and knowledge. Everything that I have learned from you will shape my future for many years to come.

I am also grateful for my second advisor, **A.Dieter Schlüter**, who shared his extensive knowledge and his very different point of view — compared to mine — on polymers with me. I have always enjoyed our diverse discussions and I am grateful for your patience with my molecule-butchered approach to polymer chemistry.

Since not everything goes according to plan in academia, I want to thank **Martin Kroeger** for taking over as my advisor after everything took longer than expected. You also helped me to understand a lot about math and I have always enjoyed our discussions about the wackier parts of the math that cropped up in this project.

Many thanks to **Arkadiy Simonov** for helping me to get a grip on his program. I also want to thank you for all the interesting discussion about PDF analysis, Fourier transforms and ducks. Your guidance on all these topics was very welcome.

I am grateful for all the discussions I had with **Ella Schmidt**. Thank you for sharing your understanding of reciprocal space with me and thank you for all the fun discussions about eigenvectors and eigenvalues.

Many, many thanks to **Daniel Messmer**, who shared his lab with me for more than three years. Thank you for sharing all the joy and pain with me when parts of my project worked or when my code crashed. Thank you for the many necessary — and unnecessary — insights into the psyche of the common chemist and for everything I was able to learn from you about chemistry. Also, thanks for the cakes, muffins and correcting this thesis.

I am in debt towards the two students I had the honor to supervise, **Florian Grieder** and **Gabriele Pagani**. You have performed some invaluable tasks which gave everyone involved in this project a better understanding about the processes that happen during two-dimensional polymerization.

Thanks to **Ralph Lange**, who gave me a lot of insights into the world of polymers and chemistry in general. I enjoyed working with you and supporting you with your own PhD project, your high professionalism and outstanding work ethics — which is quite the opposite of how you usually advertise yourself — was always inspiring.

Special thanks to **Max Kory**, who provided me with a lot of valuable insights in my first days and also provided all the gorgeous crystals which have accompanied me all these years.

A lot of thanks to **Hannes Beyer**, who provided several insights using optical microscopes and AFM images for his PhD project which in turn helped me to understand the system I was investigating better.

A lot of thanks to **Julia Dshemuchadse** for helping me to get to know the world and people in science. Although I did not yet know you at the time, I still count the day lucky, when your visa issuance got delayed, otherwise we wouldn't have met.

I want to extend my thanks towards **Dmitry Chernyshov** and **Alexey Mikheykin** for their support during our measurement time at the Swiss-Norwegian Beam Lines at ESRF.

I also want to thank the rest of my thesis committee, **Athina Anastasaki**, **Jan Vermant** and **Michael Wörle**, who took the time to properly read this thesis and offered a lot of constructive criticism.

I am very grateful for the help of **Alba Sicher** in proofreading the Italian version of my abstract.

There are also many colleagues and friends connected to the former Laboratory of Crystallography to whom I want to extend my thanks for their support and friendship, namely **Magda Cichocka**, **Daniel Jung**, **Catherine Dejoie**, **Pawel Kuczera**, **Fiodar Kurdzesau**, **Roksolana Kurdzesau**, **Dmitry Logvinovich**, **Dan Miron**, **Ana Pinar**, **Dubravka Šišak-Jung**, **Stef Smeets** and **Soumyadipta Maiti**. Thank you for the nice working-atmosphere and the cakes. It is always fun to see you guys again!

Similar to the crystallography-connection, I also want to thank a bunch of chemists for similar reasons, namely **Kemal Celebi**, **Wenyang Dai**, **Bernd Deffner**, **Chiara Gstrein**, **Ralph Lange**, **Sandra Luginbühl-Serrano**,

Daniel Messmer (again), **Vivian Müller**, **Payam Payamyar**, **Stan van de Poll**, **Thomas Schweizer**, **Leon Serc**, **Marco Servalli**, **Philipp Tanner**, **Peter Walde**, **Wei Wang** and **Yingjie Zhao**, for and equally nice and comfortable working environment and the resulting friendship.

I want to thank the three wise scientists from the former Laboratory for Crystallography at ETH Zurich, **Christian Bärlocher**, **Lynne McCusker** and **Walter Steurer** who shared their vast experience, joy and the occasional cake with me and helped me to understand the world of crystallography a little bit better.

Also a lot of thanks to all of the administrative assistants, **Cornelia Aurelio**, **Vappu Hämmerli** and **Daniela Zehnder**, who helped me to navigate through ETH's bureaucracy.

I am thankful for a lot people whom I have met on conferences and who helped me understand the vast topic of crystallography little bit better, namely **Philipp Hans**, **Paul Klar**, **Ute Kolb**, **Yasar Krysiak**, **Falk Meutzner**, **Melanie Nentwich**, **Julia Polisthuk**, **Khai-Nghi Truong** and **Matthias Zschornak**.

I am also grateful for the people with whom I was able to venture through fantastic worlds after work, first through the lands Barovia with **Richard Bernitzky**, **Jay Coleman**, **Mohammad Divandari**, **Daniel Messmer** (again again), **Vivian Müller** and **Stan van de Poll** and then to a place where there might be giants with **Richard Bernitzky**, **Marc Bitterli**, **Mohammad Divandari**, **Daniel Messmer** (again again again), **Kathrin Reutter**, **Alba Sicher** and **Katrina Anne Smith-Mannschott**. You guys rock! And thanks for the countless hours of laughter.

I also want to express my deep gratitude towards **Klaudia Hradil** and **Ronald Miletich-Pawliczek**. You guided my first steps in science and pointed me towards ETH. Thank you very much for your support early on and your moral support during my work here at ETH.

I gratefully acknowledge the funding of this research via SNF grant 200021-157157.

Lydia Baumann and **Ina Böhm**, I cannot tell how much your friendship and mutual support during our PhD theses means to me.

Also a lot of thanks to my friends, **Andreas Artac**, **Walther Behr**, **Astrid Böhm** (and even Hannibal), **Tamina Buttinger-Kreuzhuber**, **Angelika Kern**, **Tanya Kochetkova**, **Gerald Pflieger**, **Veronika Plasser**, **Claudia Reissner**, **Martin Walter** and **Astrid Wittwer**, who have gave me moral support, always listened to my plight and were there for me. You are awesome!

I am so grateful to have met **Anke Müller** and for the friendship that arose from this meeting of chance. Thank you for taking me in and helping me to get a grip and footing in Switzerland.

Many thanks and lots of love goes to **Jeanette Isele**. I am so happy to have met you and I enjoy every minute with you.

Finally, I want to thank my family, **Christian Hofer**, **Margit Hofer**, **Angelika Kovar**, **Felix Kovar** and **Vince Kovar**, **Gertrude Hofer**, **Adolfine Topolansky** and **Gerhard Topolansky** for their support and trust in me in the past, present and future.

Table of contents

Abstract	ii
Riepilogo	v
Acknowledgements	viii
Table of contents	xii
List of abbreviations	xv
List of structure labels	xvi
1 Introduction and motivation	2
2 Concepts and theory	4
2.1 One-dimensional polymers	4
2.1.1 Definitions for one-dimensional polymers	4
2.1.2 Examples	5
2.2 Two-dimensional polymers	5
2.2.1 Concepts and definitions	5
2.2.2 Examples of known two-dimensional polymers	7
2.2.3 Achieving polymerization and depolymerization	8
2.2.4 Potential applications of two-dimensional polymers	8
2.2.5 Other two-dimensional materials	9
2.3 Polymer growth mechanisms	10
2.3.1 Growth mechanisms in one-dimensional polymers	10
2.3.2 Growth mechanisms in two-dimensional polymers	10
2.3.3 2D polymerization as phase transformation	11
2.3.4 Implications from published research	12
2.4 Crystalline order and disorder	13
2.4.1 Definitions for crystals and X-ray diffraction	13
2.4.2 Types of disorder	14
2.4.3 Properties derived from disorder	15
2.4.4 Three-dimensional difference pair-distribution function	15
3 The Kory-monomer and its crystal structures	20
3.1 Monomer and solvent molecules	20

3.2	Monomer crystal structure model	20
3.3	Partially polymerized crystal structure model	23
3.4	Polymer crystal structure model	23
3.5	Annealed polymer crystal structure model	24
3.6	Partially depolymerized crystal structure model	25
3.7	Fully depolymerized crystal structure model	25
3.8	The rhombille tiling	25
4	Materials, experiments, software and modeling	28
4.1	Diffraction experiments and photo-reactions	28
4.1.1	Crystal shapes and appearance	28
4.1.2	Photopolymerization	28
4.1.3	Thermal depolymerization	29
4.1.4	Used crystals and handling	29
4.1.5	Single-crystal X-ray diffraction experiments	31
4.2	Software	32
4.2.1	The Yell program	32
4.2.2	Self-written programs and scripts	32
4.2.3	Third-party software	33
4.3	Average structure modeling	33
4.3.1	Data reduction	33
4.3.2	Structure solution and refinement	34
4.4	Real structure modeling	36
4.4.1	Data selection	36
4.4.2	Data reduction	36
4.4.3	Refinement strategy	37
4.4.4	Model design principles	39
4.4.5	Displacive Disorder	42
4.4.6	Substitutional disorder	45
5	Results	48
5.1	Average crystal structure	48
5.1.1	Photopolymerization	48
5.1.2	Thermal depolymerization	52
5.1.3	Solvent molecules	55
5.1.4	Reproducibility and systematic errors	58
5.2	Real crystal structure	59

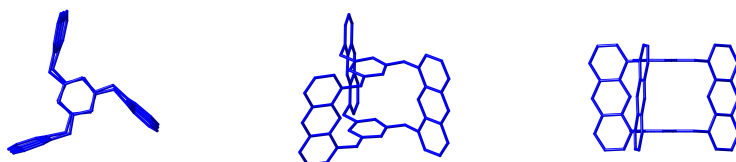
5.2.1	Features in reciprocal space	59
5.2.2	<i>Yell</i> refinement results	59
5.2.3	Displacive disorder	68
5.2.4	Substitutional disorder	77
6	2D polymerization and depolymerization	80
6.1	Insights from Bragg scattering	80
6.1.1	Structure transformation mechanics	80
6.1.2	Propagation from reaction kinetics	85
6.2	Insights from diffuse scattering	89
6.2.1	Displacive disorder	89
6.2.2	Substitutional disorder	92
7	Conclusion	98
7.1	Overview	98
7.2	Propagation mechanisms	98
7.3	Structural features promoting 2D polymerization	100
7.4	On exfoliation and single sheets	101
7.5	Modeling disorder via the 3D- Δ PDF method	102
7.6	Final remarks	103
8	Outlook	104
8.1	Monomer and polymer	104
8.2	Revisiting concepts and definitions	105
8.3	Monomer design, arrangement, and polymerization	105
8.4	3D- Δ PDF modeling	107
9	References	108
10	Appendix	118
	Attempts to recover the U^{AB} -matrix	118
	Visualizations of different growth mechanisms	119
	Correlation tables	123
	Simulated development of substitutional correlations	129
	List of figures	130
	List of tables	132
	Curriculum Vitae	133

List of abbreviations

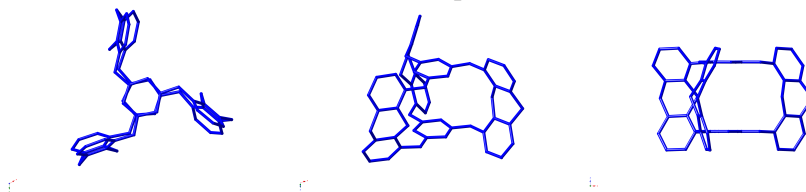
1DP	linear, one-dimensional polymer, As of the time of writing, all commercially processed polymers belong to this group
2DP	planar, two-dimensional polymer
3D-ΔPDF	three-dimensional difference pair-distribution function
ADP	atomic displacement parameter, this abbreviation is often used synonymous with anisotropic displacement parameters
DE	differential evolution
EULER	ETH's computing cluster, EULER is a German acronym for <i>Erweiterbarer, Umweltfreundlicher, Leistungsfähiger ETH-Rechner</i> , literally: extendable, environmental-friendly, powerful ETH computer
IUCr	International Union of Crystallography
MC	Monte Carlo, administrative area of the Principality of Monaco, the term <i>Monte Carlo simulation</i> refers to a broad class of algorithms involving repeated random sampling which were named after a casino in the Monte Carlo area
MDP	molecular displacement parameter, defined analogous to ADP but refers to a group of atoms
PDF	pair-distribution function
R-value	crystallographic reliability indices
scsc	single-crystal-to-single-crystal, typically a property of a phase transition
SOF	site occupation factor
TDS	thermal diffuse-scattering

List of structural elements

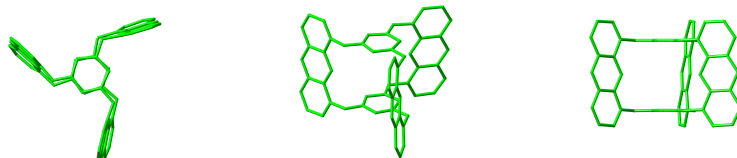
M_S monomer molecule surrounded by the solvent molecule, colored in blue in all structure representations



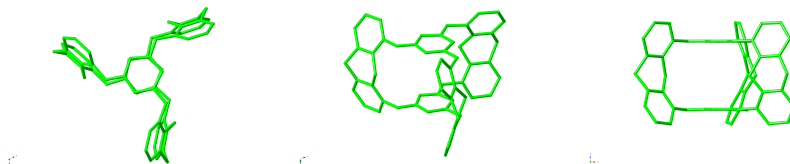
P_S polymerized counterpart to M_S and surrounded by the solvent molecule, colored in blue in all structure representations



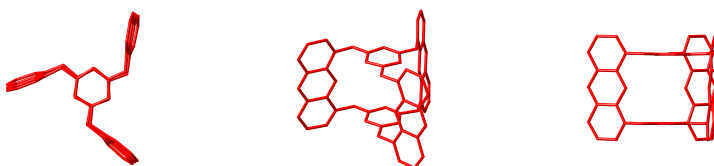
M_T monomer molecule surrounded by the template molecule, colored in green in all structure representations



P_T polymerized counterpart to M_T and surrounded by the template molecule, colored in green in all structure representations



T template molecule, surrounded by all other molecules, colored in red in all structure representations



2cpy 2-cyanopyridine, located either upright next to M_S/P_S or sandwiched between M_T/P_T and the template in a disordered arrangement



\bar{C}_n conversion ratio, ratio of anthracene dimers in a given partially polymerized structure with respect to all possible anthracene dimers

1 Introduction and motivation

Since the conceptual introduction of polymers by Staudinger in 1920, they have become a very important material class in daily life. The basic topological element of a traditional polymer is a chain. These chains are constructed from bifunctional molecules, which are connected to one another in great numbers during the growth of the polymer. The growth mechanism is a defining feature of polymers and understanding the different types of polymerization mechanisms allows further control over the properties of the final polymer.

A breakthrough in polymer chemistry was achieved by the synthesis of trifunctional molecules and their crystallization in layers with a specific molecular orientation (Kissel *et al.*, 2012). The arrangement allowed through the use of an external trigger to laterally connect the molecules to form a stack of covalently bonded, two-dimensional networks. This process is called two-dimensional polymerization. The product of two-dimensional polymerization is a two-dimensional polymer, which is a sheet-like macromolecule with a thickness of a few atoms and theoretically infinite lateral expansion. They are expected to be useful for various purposes ranging from molecular sieves to components for advanced blends. Due to the power of organic synthesis and chemical versatility of hydro-carbons, properties of two-dimensional polymers are, theoretically, highly customizable for their intended task.

The analysis of the starting crystals and the final two-dimensional polymer crystals is simple, as they are almost ideal crystals. Exposing an ideal crystal to X-rays leads to Bragg scattering, a periodic pattern from which the average crystal structure is derived. However, the bond formation during the growth of a two-dimensional polymer in a crystal can be interrupted at any time. The result is a disordered crystal which contains structural properties from both the starting material and the end-product. Disordered crystals have been known since the beginning of modern X-ray crystallography (Friedrich *et al.*, 1913; Debye, 1913; Laue, 1918), but even today, analyzing and understanding the local structure of disordered crystals is a very challenging and time-consuming task. The local structure is often important to explain chemical or physical properties of certain materials. For example, several key technologies of the modern era, such as semiconductors, are made from disordered crystals. Exposing a disordered crystal to X-rays leads to dif-

diffuse scattering superimposed on top of the Bragg scattering. Unlike Bragg scattering, diffuse scattering can occur at any position in the diffraction pattern. The distribution, shape, and relative intensities of the diffuse scattering reveal insights into the local ordering of atoms.

Due to the novelty of two-dimensional polymers, several fundamental and applied research initiatives are currently underway. One central question for understanding the nature of 2DPs is how polymerization propagates in the crystalline state. Given the unprecedented number of bond formations associated with two-dimensional polymerization, it is also important to gain insight into all the structural aspects associated with this unparalleled chemical process. This in particular concerns the propagation mechanisms of both polymerization and depolymerization in the single crystal and the understanding of the factors that enable such complex reactions. The aim of this project is the identification and detailed characterization of the two-dimensional polymerization and depolymerization mechanism of a monomer capable of two-dimensional polymerization in the single crystal. Due to the wide range of topological possibilities compared to linear polymers, different mechanisms in two-dimensional polymers are expected. For this purpose, two complementary X-ray techniques are utilized: standard single-crystal Bragg scattering experiments and the recently developed three-dimensional difference pair distribution function method for local structure determination from diffuse scattering. The former method is expected to deliver the average space-time properties during polymerization while the latter will unravel the specific mechanisms involved.

2 Concepts and theory

2.1 One-dimensional polymers

2.1.1 Definitions for one-dimensional polymers

Polymers created from bifunctional molecules are topological chains and are referred to as linear, one-dimensional polymers (1DPs)¹. The *Polymer Division* (formerly the *Commission on Macromolecular Division*) of the International Union of Pure and Applied Chemistry has published the so-called *Purple Book* (Jenkins *et al.*, 1996; Jones *et al.*, 2009) which contains recommendations regarding the definitions and nomenclature of 1DPs. In the following some important definitions from the *Purple Book* are summarized and put into the context of this work.

A **monomer molecule** is a molecule that can undergo polymerization. For 1DPs in general, it has exactly two reactive centers that participate in a polymerization reaction¹. An **oligomer molecule** is a molecule of intermediate relative molecular mass² whose structure is derived, actually or conceptually, from the monomer. Its physical properties are strongly dependent on the number of incorporated monomer molecules and therefore also different from the monomer or polymer properties. The number of incorporated monomer molecules may be indicated by greek prefixes, *e.g.* an oligomer molecule created from two monomer molecules is called a dimer. A **polymer molecule** is a molecule of high relative molecular mass², the structure of which essentially comprises the multiple repetition of units derived, actually or conceptually, from monomer or oligomer molecules. Usually, a chemical or physical stimulus is used to connect monomer molecules together to form a polymer molecule in a process called **polymerization**. Adding or removing a small number of monomer molecules to or from an already existing polymer has negligible effects on the polymer's properties. The length deviation between individual polymer chains is called **dispersity** (Stepito, 2009). **Depolymer-**

¹For practical purposes, polymeric materials are often branched or cross-linked, but further differentiation would unnecessarily complicate the matter in this context without adding useful content.

²Relative to the monomer.

ization is the process of converting a polymer into many individual monomer molecules.

2.1.2 Examples

Currently, all commercially exploited polymers belong to the group of 1DPs. They have become ubiquitous in industrial and everyday applications with a turnover on the European market alone of 350 billion euros in 2017 (PlasticsEurope, 2019). Examples would be polyethylene terephthalate (PET), which is used to produce drinking bottles, or polystyrene (PS), from which several everyday appliances are manufactured.

2.2 Two-dimensional polymers

2.2.1 Concepts and definitions

Planar, two-dimensional polymers (2DPs) are conceptually different from 1DPs as they form nets rather than chains. The field of 2DPs is comparable young; The first monomer designed for two-dimensional polymerization and its successful polymerization were reported by Kissel *et al.* (2012), although examples of 2DPs created from naturally occurring monomers have been known since the 1990s, see *Section 2.2.2*. The vastly different topology makes a straightforward application of the definitions for 1DPs difficult at best. For instance, a monomer for two-dimensional polymerization requires at least three reactive sites instead of exactly two. The novelty of the field requires that the pre-existing synthesis principles, application areas, definitions and mechanisms for 1DPs have to be critically reviewed and adjusted to the second dimension. Synthesis principles have already been covered extensively in the scientific literature (Sakamoto *et al.*, 2009; Colson and Dichtel, 2013; Xiang *et al.*, 2015; Peplow, 2016; Servalli and Schlüter, 2017; Yang *et al.*, 2017; Feng and Schlüter, 2018; Zhu *et al.*, 2018; Wang and Schlüter, 2018). While the majority of these works also touch upon the subjects of applications, definitions and mechanisms, dedicated research papers regarding definitions and mechanisms are underrepresented. Only a few works deal with mechanisms in 2DPs (Müller *et al.*, 2017; Liu *et al.*, 2017).

A particularly influential contribution to the topic of 2DPs was published by Payamyar *et al.* (2016) because it presented the currently most widely accepted definition of 2DPs, although this was not the first work attempting to do so (Colson and Dichtel, 2013; Xiang *et al.*, 2015). The definition of Payamyar *et al.* (2016) comprises five key points:

1. Planarity: 2D polymers are topologically planar sheets.
2. Repeat units: 2D polymers have repeat units rendering them crystalline in at least one conformation.
3. Covalent bonds: the repeat units of 2D polymers are connected by covalent bonds.
4. Thickness: 2D polymer molecules have the thickness of the constituent repeat unit (monolayers).
5. Separability: 2D polymers are strong enough to be free - standing under relevant gravitational conditions.

Payamyar *et al.* (2016) were also the first to speculate about the growth mechanisms in 2DPs, a topic that has not been further studied since.

In order to obtain a 2DP, a certain amount of control over the molecular orientation and arrangement is required, otherwise two-dimensional polymerization will not be possible at all (Servalli *et al.*, 2017), or the resulting sheets will have small diameters (Sakamoto *et al.*, 2009). Solution polymerization is currently not a viable option, as it does not allow control over orientation and arrangement. The currently most successful routes to obtain 2DPs are the interface (Feng and Schlüter, 2018; Müller *et al.*, 2018; Servalli *et al.*, 2018; Dong *et al.*, 2018) and the single-crystal approach (Liu and Loh, 2017; Lange *et al.*, 2017; Feng and Schlüter, 2018; Servalli *et al.*, 2018). The single-crystal approach is of particular importance for this work and is schematically explained in *Figure 2.1*. The key feature of this approach is the prearrangement of the monomer in a reactive packing, which allows the monomers to form a polymer, by crystallization. Polymerization is then carried out as a single-crystal-to-single-crystal (*scsc*) transformation. Furthermore, this approach allows structure determination via diffraction techniques of the initial monomer and final polymer state. Depending on the chemistry used in polymerization, intermediate states may also be accessible by diffraction techniques. A drawback of the single-crystal approach is

that, to obtain individual 2DP-sheets, a final dry or wet exfoliation step is required.

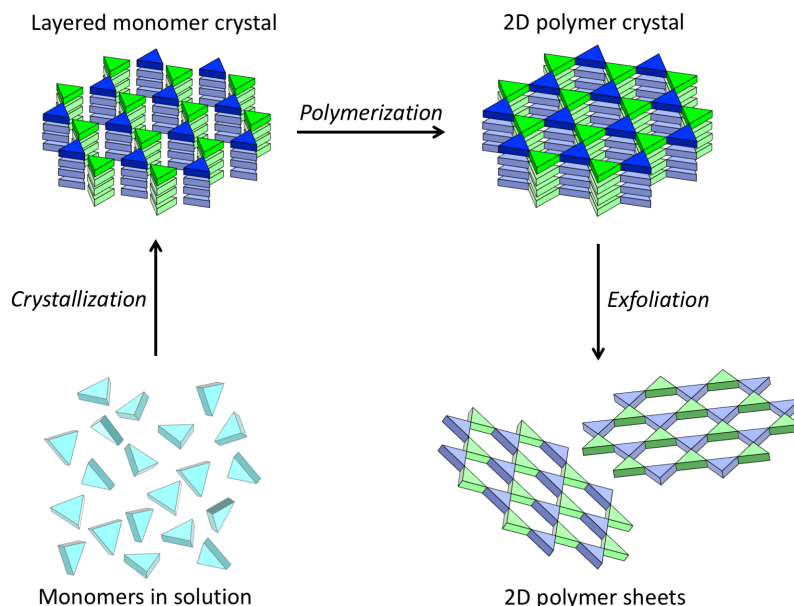


Figure 2.1: Graphical representation of the single-crystal approach. First, a monomer is pre-arranged in layers through crystallization in a reactive packing to allow polymerization exclusively within their layer. Second, polymerization is achieved by using an external trigger to obtain a layered two-dimensional polymer crystal. Finally, single 2DP-sheets are obtained through exfoliation techniques.

2.2.2 Examples of known two-dimensional polymers

There are already several examples of 2DPs obtained from a large variety of synthetic approaches. 2DPs were first mentioned by Rao *et al.* (1993), when Fullerene crystals were subjected to geologically relevant pressures and temperatures, under which they formed a layered 2DP crystal. Since then, additional structures under comparable conditions have been discovered (Oszlányi and Forro, 1995; Moret *et al.*, 2000). Graphene is another example of a 2DP, which is typically obtained by exfoliation of the naturally occurring

graphite (Novoselov *et al.*, 2004) or by vapor deposition (Choi *et al.*, 2010). Liu and Loh (2017) provided a synthetic route to 2DPs via aromatic coupling reactions.

Examples more relevant for this work exploit topochemical reactions triggered by light. They include $[4 + 4]$ cycloadditions (Kory *et al.*, 2014b; Kissel *et al.*, 2014), $[4 + 2]$ cycloadditions (Kissel *et al.*, 2012) and $[2 + 2]$ cycloadditions (Lange *et al.*, 2017). Note that the 2DPs described by Kory *et al.* (2014b) and Lange *et al.* (2017) can be synthesized on the ten to hundred gram scale under laboratory conditions and that the monomer of the polymer provided by Kory *et al.* (2014b) was also obtained in significant amounts using industrial equipment (Tanner *et al.*, 2018).

2.2.3 Achieving polymerization and depolymerization

Topochemical photoreactions (Wegner, 1971; Schmidt, 1971; Hasegawa, 1983) are very successful in realizing two-dimensional polymerization. This applies in particular to the well-studied $[4 + 4]$ photoinduced cycloaddition of anthracene (Greene *et al.*, 1955; Bouas-Laurent *et al.*, 1980; Becker *et al.*, 1985; Bouas-Laurent *et al.*, 2000, 2001; Bholá *et al.*, 2013; Payamyar *et al.*, 2014) which is used for polymerization of the monomer investigated in this work. Although polymerization can be triggered by a wide range of wavelengths, using a wavelength in tail-end of the absorption spectra (Novak *et al.*, 1993; Enkelmann *et al.*, 1993) is preferred because it allows for a mild and controlled polymerization as a *scsc* transformation. By turning-off the triggering light source at any time before a full conversion from monomer and polymer is reached, stable intermediate states are obtained.

A key feature of the anthracene cycloaddition is that is reversible with either heat treatment or a shorter irradiation wavelength. Similar to photopolymerization, depolymerization can be paused by removing the crystal from the triggering source.

2.2.4 Potential applications of two-dimensional polymers

Graphene showcases the impact of two-dimensional materials on scientific and industrial applications, ranging from biomedicine (Chung *et al.*, 2013)

to battery materials (Bae *et al.*, 2012) and solar cells (Perreault *et al.*, 2015; Zhang *et al.*, 2018). In addition to examples known from graphene, 2DPs can provide many possible applications that can be tailored to the desired application. Frequently, 2DPs are porous materials, making them ideal molecular sieves with a tunable mesh size (Zheng *et al.*, 2016; Wang *et al.*, 2017). The highly customizable surface of 2DPs allows for custom-made surfaces to achieve epitaxial crystallization of certain proteins (de Poel *et al.*, 2019). Finally, their chemical properties are exploited for holographic data storage (Müller *et al.*, 2017). In bulk, 2DPs can be utilized for gas storage and super-capacitors (Liu *et al.*, 2017).

2.2.5 Other two-dimensional materials

Two-dimensional materials such as 2DPs have several desirable properties for modern applications. It is therefore not surprising that there are many other types of two-dimensional materials. A few selected examples are briefly discussed in this chapter.

Covalent and metal-organic frameworks These materials use the modularity of two structural units, linkers and spacers, to create one-, two-, or three-dimensional structures (Cote *et al.*, 2005; Feng *et al.*, 2012). In the case of covalent organic frameworks, linkers and spacers are both organic molecules, but in metal-organic frameworks the linker is a transition metal. The former typically rely on the reversible bond formation between B - O, C - N, B - N, or B - Si (Cote *et al.*, 2005; Waller *et al.*, 2015), although rare examples based on C - C bond formation exist (Zhuang *et al.*, 2016). 2D frameworks are usually not exfoliated for applications and application studies are more focused on catalytic reactions and ion/molecule storage (Eddaoudi *et al.*, 2002; Cote *et al.*, 2005).

2D-Perovskites and PdSe₂ Strictly speaking, these materials are not two-dimensional because they violate the fourth rule introduced by Payamyar *et al.* (2016), *i.e.* they are not one repeating unit thick. However, their typical thickness is in the single-digit nanometer range for the organic-inorganic perovskites (Dou *et al.*, 2015) and in the sub-nanometer range for PdSe₂ (Oyedele *et al.*, 2017). In either case, their electronic properties make them interesting for applications in nano-scale electronics (Novoselov *et al.*, 2016).

2.3 Polymer growth mechanisms

2.3.1 Growth mechanisms in one-dimensional polymers

Polymerization in 1DPs proceeds via one of two topologically different classes of growth mechanisms, called chain growth and step growth (Flory, 1953). In step growth polymerization, all reactive sites have the same reaction probability, which leads to simultaneous growth of all chains, which can also combine. Chain growth polymerization is characterized by an active species³ which has a much higher probability of reacting with monomer molecules than monomer molecules among themselves, resulting in the growth of only a few chains at any given time.

Chain and step growth are both achievable in solution and in the solid state. Of particular interest for this work are solid-state photopolymerizations which are under investigation since the seventies of the last century (Baughman, 1974; Baughman and Chance, 1980; Hoang *et al.*, 2002; Sun, 2006; Dou *et al.*, 2014; Medishetty *et al.*, 2016). Usually, the authors concentrated on the monomer and polymer crystal structures obtained from X-ray diffraction and on kinetic studies based on methods other than X-ray diffraction. Structure investigations of partially polymerized structures, which also address the growth mechanism, are rare and often restricted to a single intermediate state, *e.g.* Grimm *et al.* (1982). In this regard, the work by Albouy *et al.* (1983) deserves special mention, because this is so far the only investigation of a growth mechanism using diffuse X-ray scattering. Works regarding depolymerization are comparable rare, *e.g.* Johnston *et al.* (2012).

2.3.2 Growth mechanisms in two-dimensional polymers

At the time of writing, no explicit research on the growth mechanisms of 2DPs has been published, so a *gedankenexperiment* was conducted to formulate simple propagation models. An essential assumption was that propagation is dependent on the reactivity between functional groups. Even slight variations in the functional group's geometry or relative arrangement, for example a variation of the distance between the groups (Schmidt, 1971; Kissel *et al.*, 2014), may change the reaction probabilities. In the following, three

³Usually an initiator molecule or an active chain end.

simple models are introduced which differ in the way how the reactivity of functional groups is influenced by the local environment. In the first case it is assumed that the reactivity of a functional group does not depend on whether or not other functional groups in the nearest neighborhood have reacted. In the other cases, it is assumed that the reaction probability is reduced or enhanced if functional groups have dimerized in the direct lateral neighborhood. In the following, these models are called *unchanged* (Figure 2.2a), *reduced* (Figure 2.2b) and *enhanced* (Figure 2.2c), respectively. The unchanged reactivity model results in a *random* growth mechanism, the reduced reactivity model in a *repulsive* growth mechanism and the enhanced reactivity in an *island* growth mechanism.

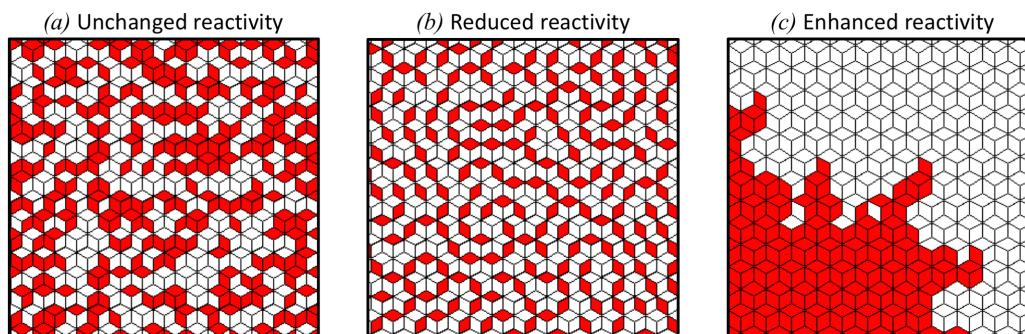


Figure 2.2: Concept drawings of simple (a) unchanged, (b) reduced and (c) enhanced reactivity models. A white rhomb represents a reactive center ready to dimerize while a red rhomb represents an already dimerized site. Please note that all models have an equal amount of reactive centers and dimers. Modified with permission from Hofer *et al.* (2018).

Note that the terms for propagation mechanisms in 1DPs, chain growth and step growth, should not be used analogous or synonymous with the here introduced terms. Besides avoiding confusion, a growth mechanism for 2DPs can be conceived which forms linear chains during an intermediate state.

2.3.3 2D polymerization as phase transformation

Since polymerization is also a phase transformation, it can be described using the *Johnson-Mehl-Avrami-Kolmogorov* model (Kolmogorov, 1937; Avrami,

1939; Johnson and Mehl, 1939; Avrami, 1940, 1941), which is frequently abbreviated as *Avrami model*. The *Avrami* equation correlates the transformation propagation Y with transformation time t via

$$Y(t) = 1 - e^{-\omega t^n} \quad (2.1)$$

where $\omega > 0$ is a system-specific constant and n is the Avrami exponent. The *Avrami* exponent is an indicator for the propagation mechanism during any phase transformation (Avrami, 1940; Hay, 1971; Gedde, 1995). Boldyreva (Boldyreva and Salikhov 1985; Boldyreva 1987*a*, 1987*b*) used the Avrami formalism along with Monte Carlo (MC) simulations to study the influence of reactivity on kinetics and spatial distribution on a square lattice of an arbitrary solid state reaction.

2.3.4 Implications from published research

The study of another 2DP by Kissel *et al.* (2014) is of particular importance although two-dimensional polymerization propagation was neither explicitly nor implicitly discussed. However, their detailed crystallographic analysis of the two-step irradiation procedure provided several important insights into the propagation mechanism, which relies on the distance differences between two anthracene blades from neighboring monomer molecules. Two of the three blades per monomer molecule are an almost equal distance away from their direct opposite blades while the third is much closer to its neighbor. Accordance with Schmidt's rules (Schmidt, 1971), anthracene pairs separated by the short distance were dimerized substantially faster than anthracene pairs separated by a longer distance, resulting in a fully ordered, dimerized intermediate state. Only a close inspection of the residual electron density maps reveals that a very small percentage of anthracene blades separated by a long distance were dimerized (Kissel *et al.*, 2014, supporting information). By using a second, much shorter wavelength, full polymerization was achieved. This example clearly shows the importance of the distance between the photo-reactive centers.

Studies revolving around 2DPs from fullerenes already utilized diffuse scattering to investigate the disorder of the monomer (Ravy *et al.*, 1996; Launois

and Moret, 2000) and an intermediate structure (Moret *et al.*, 2004). Unfortunately, the obtained intermediate structure is incompatible with two-dimensional topology because dimerization occurs across layers, which emphasizes the importance of obtaining a reactive packing in the monomer crystal. Another study on fullerene 2DPs by Moret *et al.* (2000) shows that multiple 2DP phases can coexist within the same particle.

2.4 Crystalline order and disorder

2.4.1 Definitions for crystals and X-ray diffraction

The International Union of Crystallography (*IUCr*) and its commissions are the accepted authority regarding definitions in crystallography. Unlike in chemistry, there exists no single reference publication which only contains terminology but the *IUCr* maintains an online dictionary, where it collects the definitions for the most commonly used terms. Additional papers regarding definitions are published in irregular intervals, *e.g.* Trueblood *et al.* (1996). In the following, some important definitions are summarized and contextualized for this work.

An **ideal crystal** is obtained by the infinite repetition of identical structural units in space. Any deviations from the ideal structure are called defects or **disorder**. The **real crystal** describes a crystal structure in its entirety, including all defects and disorder. The **average structure** or **Bragg structure** describes a crystal structure in terms of the average location of atoms, the average deviations⁴ from the average location of atoms, and site occupation factor (SOF)⁴ of those atoms of a given crystal and is represented by the unit cell and its contents. The atomic arrangement within the unit-cell is subjected to inversion, rotational and translational symmetry. Standard diffraction experiments give access to the average structure through **Bragg scattering** (Bragg and Bragg, 1913). However, information on the distribution of disorder is not obtainable via Bragg scattering. The local deviations from the ideal and average crystal structure give rise to **diffuse scattering** (Welberry and Weber, 2015) during diffraction experiments, from which further information on the real structure is obtained. Experiments which

⁴The average deviation and the site-occupation factors describe the average disorder.

combine information from Bragg and diffuse scattering are called **total scattering** experiments. A typical scattering experiment for structure refinement measures the total scattering. However, in the case of moderate disorder, the real structure is almost equivalent with the ideal and average structure and contributions from the diffuse scattering are therefore negligible. In cases with significant contributions from the diffuse scattering, **two-body correlations** of the real structure are obtainable. Many-body correlations are not obtainable from diffuse scattering (Welberry and Withers, 1991).

2.4.2 Types of disorder

Disorder can be present in any crystalline structure and has several aspects (Welberry and Butler, 1994; Keen and Goodwin, 2015; Welberry and Weber, 2015). These aspects are the short-range order parameters (Cowley 1950*a*, 1950*b*), the Warren size-effect (Warren *et al.*, 1951), thermal diffuse scattering (Debye, 1913; Waller, 1923) and Huang scattering (Huang, 1947). In the following, these terms are explained and sorted into three broader categories⁵ which will be used throughout the rest of this work.

Substitutional disorder describes the exchange of an atom or a group of atoms in a certain arrangement with an atom or a group of atoms with differing chemical composition or in a different arrangement. Note that exactly one of the substitution's participants can also be a void. The short-range order parameters belong to this group.

Displacive disorder describes the local deviation of an atom or a group of atoms from their average positions. That deviation is caused by either thermal motion or static displacement leading to thermal diffuse scattering or Huang scattering, respectively.

The **size effect** describes a local deviation of an atom or group of atoms from their average positions caused by an atom or group of atoms that have a different local space requirement than the average structure provides for them. The Warren size-effect belongs to this group.

In the average structure, the average substitutional disorder is contained in the SOFs. The average displacive disorder is the space-time average of

⁵Equation 2.2 to Equation 2.5 later in this chapter are the foundation for these broader categories as they do not discriminate between a single atom or group of atoms.

static and thermal displacements and expressed by the atomic displacement parameter (ADP). The size effect also contributes to the ADPs.

2.4.3 Properties derived from disorder

Disordered materials are encountered regularly in everyday life. For example, doping, the intentional introduction of disorder, of silicon forms the basis for all modern semiconductor materials. The majority of colorful gemstones rely on similar concepts to obtain their color (Nassau, 1978, 1983). In a more scientific context, Prussian blue has many applications in electro-chemistry (Neff, 1978) which rely on the disorder of cyano groups. Also, some ferroic materials function (Coates *et al.*, 2018) because of the disorder. In protein crystals, disorder and diffuse scattering is common (de Klijjn *et al.*, 2019). It is worth noting that the vast majority of studies on disorder is done using crystalline powders and that many synchrotron radiation facilities have dedicated beamlines for these experiments. However, recent advancements in instrumentation, computing power and methodology made diffuse scattering studies of single-crystals more and more common (Sangiorgio *et al.*, 2018; Paściak *et al.*, 2019).

2.4.4 Three-dimensional difference pair-distribution function

Pair-distribution function (PDF) analysis uses vector pairs between objects to describe a structure. PDF analysis has become a standard method in crystallography and materials sciences to investigate disordered materials (Young and Goodwin, 2011) but it is limited to crystalline powders and nano particles. The PDF method averages across all spatial directions, therefore only the magnitude of vectors between pairs is available and directional information is lost. Typically, the total scattering pattern is used for modeling and analysis (Billinge, 2019).

An extension of the PDF method is the three-dimensional difference pair-distribution function (3D- Δ PDF) method (Weber and Simonov, 2012; Simonov *et al.*, 2014a; Welberry and Weber, 2015) which extends the PDF theory to single-crystals. A major advantage of the 3D- Δ PDF method is that it preserves direction and magnitude of vectors between pairs which allows to resolve structures of greater complexity. Unlike standard PDF, only

the diffuse scattering is used for modeling. Therefore, the 3D- Δ PDF describes the real-structure properties as pair-correlations and highlights how the real-structure pair-correlations differ from the average structure pair-correlations.

In the following, the mathematical relation between diffuse scattering and the 3D- Δ PDF is presented, which was developed by Weber and Simonov (2012). In general, diffuse scattering arising from disorder (Welberry and Butler, 1994) is described as

$$\begin{aligned}
I_D = N \sum_{st} \sum_{lmn} c_s c_t f_s f_t^* & \left[(1 - \alpha_{lmn}^{st}) \right. \\
& \times \langle \exp \{ i2\pi (h_1 X_{lmn}^{st} + h_2 Y_{lmn}^{st} + h_3 Z_{lmn}^{st}) \} \rangle \\
& \left. - \langle \exp \{ i2\pi (h_1 X_{\infty}^{st} + h_2 Y_{\infty}^{st} + h_3 Z_{\infty}^{st}) \} \rangle \right] \\
& \times \exp \{ i2\pi (h_1 l + h_2 m + h_3 n) \}
\end{aligned} \tag{2.2}$$

which is a summation over the atom pairs consisting of type s and t and over all unique interatomic vectors lmn . The number of atom pairs in the crystal is described by N . The relative concentrations of a given atom type are given by c_s and c_t . The parameters f_s and f_t refer to atomic or molecular scattering factors with the asterisk denoting the complex conjugate. The value α_{lmn}^{st} is Cowley's short range order parameter (Cowley, 1950a). Relative atomic displacements are defined by X_{lmn}^{st} , Y_{lmn}^{st} and Z_{lmn}^{st} with terms containing ∞ in their subscript indicating that the average is taken for uncorrelated atoms, *i.e.* separated by large distances. Angle brackets refer to the averages over all atom pairs N with the same site separation. Equation 2.2 is expressed in terms of pair correlations as

$$\begin{aligned}
I_D(\mathbf{h}) = \sum_{\mathbf{R}_{uvw}} \sum_{st}^{\text{crystal cell}} & \left[p_{uvw}^{st} \langle \exp (i2\pi \mathbf{h} \mathbf{u}_{uvw}^{st}) \rangle \right. \\
& \left. - c_s c_t \langle \exp (i2\pi \mathbf{h} \mathbf{u}_s) \rangle \langle \exp (i2\pi \mathbf{h} \mathbf{u}_t) \rangle \right] \\
& \times f_s(\mathbf{h}) f_t^*(\mathbf{h}) \exp [i2\pi \mathbf{h} (\mathbf{R}_{uvw} + \mathbf{r}_{st})]
\end{aligned} \tag{2.3}$$

which is the summation over all atomic pairs st in the unit cell obtained from the average structure and all further correlated lattice vectors \mathbf{R}_{uvw} . The

joint probability p_{uvw}^{st} describes the likely hood to find an atom s separated from an atom t by the vector $\mathbf{R}_{uvw} + \mathbf{r}_{st}$, *i.e.* the vector \mathbf{R} between individual unit cells ($u, v, w \in \mathbb{Z}$), modified by \mathbf{r}_{st} which represents the separation within the average unit cell. The sum of the vectors \mathbf{R}_{uvw} and \mathbf{r}_{st} is equivalent to lmn from *Equation 2.2*. The difference of the real and average distance between the atoms s and t separated by $\mathbf{R}_{uvw} + \mathbf{r}_{st}$ is expressed by \mathbf{u}_{uvw}^{st} while \mathbf{u}_s and \mathbf{u}_t are the independent displacement distributions of these atoms. Angle brackets denote space-time averages.

The Fourier transform of *Equation 2.3* yields the 3D- Δ PDF map as

$$\begin{aligned}
 P_{\Delta}(\mathbf{x}) = & \sum_{\mathbf{R}_{uvw}}^{\text{crystal cell}} \sum_{st} \left[p_{uvw}^{st} \langle \delta(\mathbf{x} - \mathbf{u}_{uvw}^{st}) \rangle - c_s c_t \langle \delta(\mathbf{x} - \mathbf{u}_s) \rangle * \langle \delta(\mathbf{x} - \mathbf{u}_t) \rangle \right] \\
 & * \rho_s(\mathbf{x}) * \rho_t(-\mathbf{x}) * \delta(\mathbf{x} - \mathbf{R}_{uvw} - \mathbf{r}_{st})
 \end{aligned} \tag{2.4}$$

with $\langle \delta(\mathbf{x} - \mathbf{u}_s) \rangle$ and $\langle \delta(\mathbf{x} - \mathbf{u}_t) \rangle$ describing average atomic displacement distributions while $\langle \delta(\mathbf{x} - \mathbf{u}_{uvw}^{st}) \rangle$ is the joint probability density distribution that describes the deviation of real interatomic vectors from average interatomic vectors. ρ_s and ρ_t are atomic or molecular scattering densities. The asterisks represent convolution operations, which make computation inefficient. It is easier to remain in reciprocal space.

If the atomic displacements are assumed to be harmonic, *Equation 2.3* is approximated by

$$\begin{aligned}
 I_D(\mathbf{h}) = & \sum_{\mathbf{R}_{uvw}}^{\text{crystal cell}} \sum_{st} \left[p_{uvw}^{st} \exp(-\mathbf{h}^T \beta_{uvw}^{st} \mathbf{h}) \exp(i2\pi \mathbf{h} \bar{\mathbf{u}}_{uvw}^{st}) \right. \\
 & \left. - c_s c_t \exp(-\mathbf{h}^T (\beta_s + \beta_t) \mathbf{h}) \right] \\
 & \times f_s(\mathbf{h}) f_t^*(\mathbf{h}) \exp[i2\pi \mathbf{h} (\mathbf{R}_{uvw} + \mathbf{r}_{st})]
 \end{aligned} \tag{2.5}$$

where β_{uvw}^{st} quantifies the joint probability displacement density of the real structure for the atom pair st while β_s and β_t are the dimensionless displacement parameters obtainable from the average structure. The size effect is

expressed by $\bar{\mathbf{u}}_{uvw}^{st}$. The superscript T indicates the transposition. $P_{\Delta}(\mathbf{x})$ in the harmonic approximation is obtained by the Fourier transform of *Equation 2.5*.

3 The Kory-monomer and its crystal structures

For this study, the crystals obtained from the monomer described by Kory *et al.* (2014b) are used to investigate polymerization and depolymerization propagation. This chapter is intended to familiarize the reader with the average structure at various stages during polymerization. Understanding the average structure forms the basis for the detailed analysis required to understand the polymerization and depolymerization mechanisms. With the exception of *Section 3.8* and unless otherwise noted, all structural information is exclusively derived from the study of Kory *et al.* (2014b). Additional details on the average structure obtained during this study are given in *Section 5.1*.

3.1 Monomer and solvent molecules

Figure 3.1a depicts the utilized monomer molecule and *Figure 3.1b* the solvent molecule 2-cyanopyridine (2cpy) which is incorporated into the monomer and polymer crystal structures. The monomer features two triazine cores in a double-decker arrangement that are connected via oxygen bridges to three anthracene blades. These blades provide the functionality for the photochemical reaction which yields the corresponding anthracene dimers through a [4 + 4]-cycloaddition, *Figure 3.1c*. This product can undergo cycloreversion at elevated temperatures, or by using a shorter wavelength compared to polymerization, *Figure 3.1c*.

3.2 Monomer crystal structure model

The monomer crystal structure, which is described in space group $R\bar{3}$, is remarkable in that it can be viewed as a columnar and a layered structure at the same time. In the column view, the monomer molecules are arranged on top of each other along the c -axis, *Figure 3.2a*. Isolated columns belong to the subperiodic rod group $\bar{3}$ (Kopský and Litvin, 2010), where each column contains three symmetry-independent molecules. The monomer molecules are not equidistantly spaced from each other, with the largest of the three gaps being filled with disordered, sandwiched 2cpy molecules. The solvent's

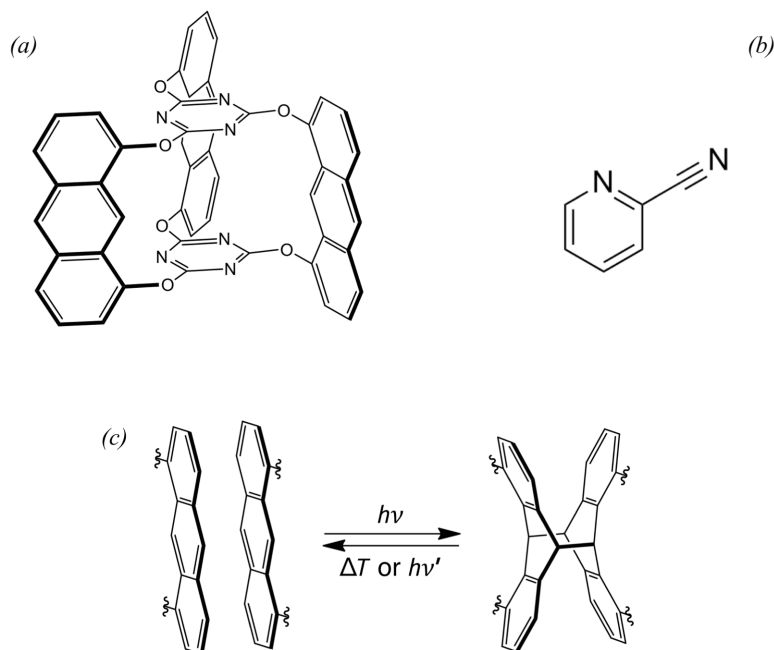


Figure 3.1: Chemical structures of (a) the monomer molecule developed by Kory *et al.* (2014b) and (b) the solvent 2-cyano-pyridine used for crystallization. (c) Two anthracene moieties undergo a thermally reversible photochemical reaction when placed face-to-face to each other. For clarity, hydrogen atoms are omitted in all structure drawings. Reproduced with permission from Hofer *et al.* (2018).

disorder is described by a three-fold symmetry-compatible excentric rotation.

In the layer view, the molecules are arranged parallel to the *ab*-plane, *Figure 3.2b*, and the three symmetry-independent monomer molecules follow the layer group symmetry $p3$ (Kopský and Litvin, 2010). Two of them assume the role of monomers, while the third serves as a template, which, in contrast to the monomer, is embedded upside down, *i.e.* it has a different sense of rotation. Symmetry-independent monomers have their triazine rings twisted against each other in opposite directions by about 8° and have different environments. The first is surrounded by solvent molecules (further referred to as M_S , shown in blue color in all figures) and the second by template molecules (further referred to as M_T , depicted in green). The packing allows anthracene

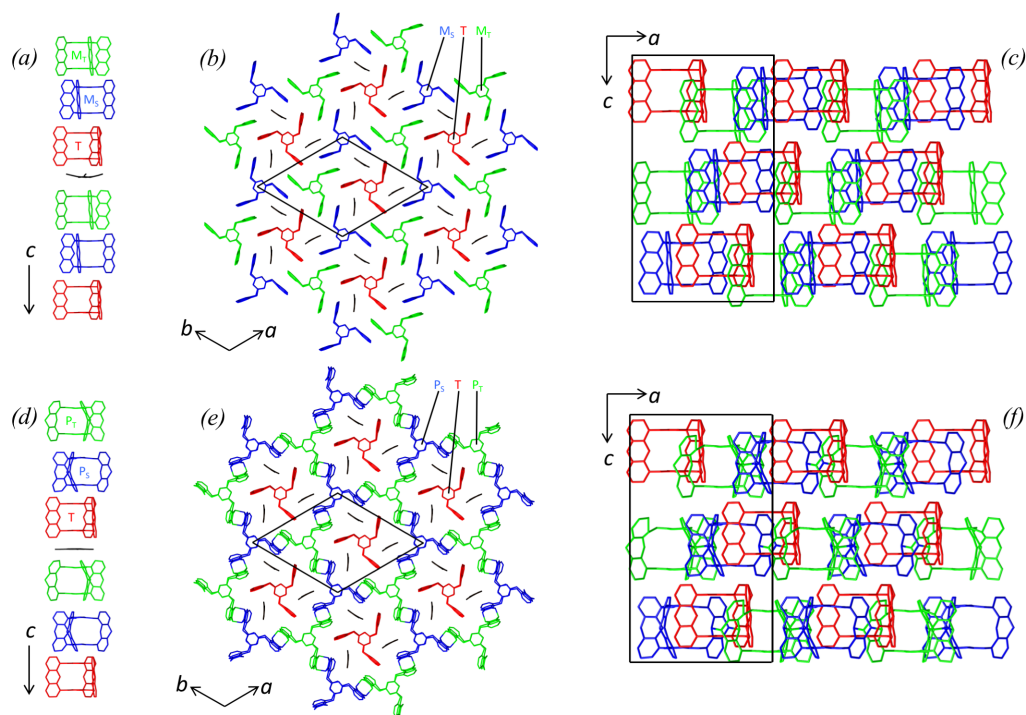


Figure 3.2: (a) Structure drawing of the monomer's column aspect. The sequence within the unit cell from top to bottom is M_T , M_S , template and solvent molecule. Note that the molecules are perfectly aligned along the threefold axis, which is in contrast to the impression left by the projection of the anthracene molecules. (b) Structure drawing of the monomer's layer aspect. M_S is located at the unit cell's vertices, M_T in the left half and the template in the right half of the unit cell. The solvent molecule is located around M_S . (c) Drawing of the full monomer crystal structure. (d) Structure drawing of the polymer's column aspect. The sequence within the unit cell is from top to bottom P_T , P_S , template and solvent molecule. (e) Structure drawing of the polymer's layer aspect. P_S is located at the unit cell's vertices, P_T in the left half and the template in the right half of the unit cell. The solvent molecule is located around P_S . (f) Drawing of the full polymer crystal structure. Modified with permission from Hofer *et al.* (2018).

blades of adjacent monomers to face each other within the critical Schmidt distance (Schmidt, 1971) for photodimerization which forms reactive centers. The pores created by monomer and template are filled with 2cpy molecules that are upright with respect to the *ab*-plane and are partially disordered. Combining column and layer aspect to the whole crystal structure, the layers are stacked in an ABC fashion, *Figure 3.2c*.

Monomer and template molecules are described in point group 3, which is against the expectation coming from quantum chemical computations (Kory *et al.*, 2014a): The conformation with the lowest energy, which coincidentally is also a desired conformation for two-dimensional polymerization, is undistorted and has point symmetry $\bar{6}$, but molecular distortions such as tilted blades and twisted cores reduce the symmetry. Kory *et al.* (2014a) could identify structures with the high-symmetry conformation, but the packings of these structures were not suitable for two-dimensional polymerization.

3.3 Partially polymerized crystal structure model

Photopolymerization gradually establishes the connectivity of M_S and M_T . By removing the crystals from the triggering light source before full conversion is reached, stable and X-ray hard intermediate states between the monomer and the polymer structure are obtained. In the average structure, the monomer and polymer sub-structures are superimposed and are described in space group $R\bar{3}$. Intermediate states are characterized by their conversion ratio (\bar{C}_n) which is the ratio of anthracene dimers formed with respect to the maximum achievable number of anthracene dimers. Kory *et al.* (2014b) presented one partially polymerized crystal structure model ($\bar{C}_n = 0.33$) with lattice parameters larger than the monomer's. Polymerization can be continued from any intermediate state all the way to full conversion to eventually obtain a 2DP crystal. Despite extensive atomic movements and further increased lattice parameters, the single crystal stays essentially intact.

3.4 Polymer crystal structure model

Eventually, all three functional groups of a particular monomer have reacted and the term monomer is no longer applicable. The result is a layered 2DP

crystal, which is still described in space group $R3$. The former monomers are of course still recognizable as moieties in the resulting 2DP. For the structural description, it is helpful to verbally and visually distinguish the moieties' two different conformations that now form the 2DP sheet by referring to the moiety formed from M_S as P_S and the one from M_T as P_T . No dimerization involving the template occurred. Worth noting is that P_S and P_T are both smaller by about 0.29 Å along the c -axis compared to their monomer counterparts, because of the kink introduced in the anthracene blades by photodimerization. They essentially maintain their sizes in the other two dimensions.

As a consequence of the lateral bond formation, the previously introduced individual columns do no longer exist as such once polymerization has finished. For structural description and comparison, the former columns are conceptually recovered by visually reducing the 2DP to its moieties P_S and P_T , *Figure 3.2d*. Each column comprises P_S , P_T , the template and the apparently unchanged sandwiched 2cpy. The rod group $\sqrt{3}$ is maintained, but the distances between template, P_S and P_T have changed compared to the monomer crystal.

The layer view shows a single 2DP sheet, *Figure 3.2e*, which is still described in layer group $p3$. The name-giving environments of M_S and M_T still exist around P_S and P_T . During polymerization, the upright 2cpys have partially reoriented themselves. *Figure 3.2f* shows the crystal structure with the combined column and layer aspects, where the sheets stack in an ABC fashion similar to the monomer structure.

3.5 Annealed polymer crystal structure model

Kory *et al.* (2014b) also presented the structure of a polymer crystal which had been annealed at 60°C and is described in space group $P3_1$, which is a subgroup of $R3$. The symmetry reduction was introduced by tilting P_S , P_T and the template with respect to the ab plane. Interestingly, the cell parameters differ significantly from the un-annealed polymerized structure, with the a -axis being larger and the c -axis being smaller by about 0.1 Å and 1.2 Å. Furthermore, the sandwiched 2cpys are completely delocalized and very weak additional reflections of undetermined origin appear.

3.6 Partially depolymerized crystal structure model

After three days of heat treatment at 453 K, the annealed polymer structure was partially depolymerized to $\bar{C}_n = 0.40$ which is comparable to the partially polymerized structure. The original space group $R3$ is recovered and the molecular arrangement is similar to the partially polymerized structure. Also, the previously delocalized 2cpys reappear at their original positions. However, the unit cell parameters differ significantly from the partially polymerized structure. The a -axis larger and the c -axis is smaller when compared to the partially polymerized crystal structure.

3.7 Fully depolymerized crystal structure model

Complete depolymerization was achieved after 21 days of heat treatment at 453 K. The molecular arrangement and unit cell parameters are comparable to the pristine monomer structure. The only major difference is that the ADPs of the depolymerized crystal structure are about two to three times larger than in the original monomer structure.

3.8 The rhombille tiling

Understanding and visualizing the distribution of reactive centers within a layer is essential when studying the growth mechanism. For this purpose, the rhombille tiling is introduced for simplification. The monomer substructure will be used as an example for constructing the rhombille tiling, *Figure 3.3a*. The reactive centers of the monomer structure are located at the lattice points of a Kagome lattice. These lattice points are visualized by either a point lattice, with each reactive center located on a lattice point (*Figure 3.3b*), or a lattice graph, where each reactive center is located at an intersection of the mesh (*Figure 3.3c*). These are equivalent constructions and can be transformed into each other. Through a Voronoi decomposition of the former or a dual tiling transformation of the latter, the rhombille tiling is obtained (*Figure 3.3d*). Each rhomb is used to describe a property of the site in the crystal structure where the rhomb is located, *e.g.* whether the two anthracene blades located at that site have reacted or not. When considering the three-dimensional distribution of the reactive centers, they can be arranged on

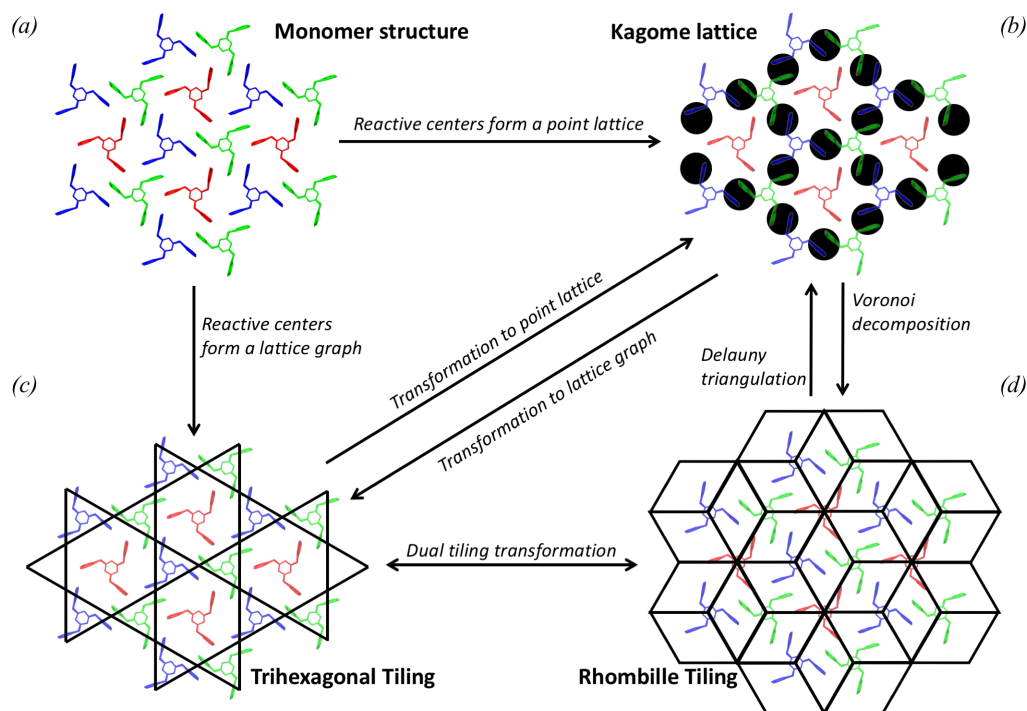


Figure 3.3: Construction of the rhombille tiling. Starting with (a) a single layer of the monomer, reactive centers are represented by constructing either (b) a point lattice or (c) a lattice graph. Note that the point lattice and lattice graph can be transformed into each other. (d) shows the rhombille tiling where each reactive center is represented by rhomb. It is derived by either applying a Voronoi decomposition to the point lattice or by forming the dual tiling of the lattice mesh. Solvent molecules omitted for clarity.

four plane-parallel sets of Kagome-lattices, one within the layer and three, distorted lattices out of the layer connected via the threefold symmetry.

Using the rhombille tiling, several geometric and topological relations between rhombs, and therefore of the overall structure, are derived. For this purpose a reference point is required. *Figure 3.4a* shows the distribution of geometric neighbors with the reference point being a dimer in the center. All rhombs with the same geometric distance from the center belong to the same neighborhood. *Figure 3.4b* shows the topological neighborhoods with respect to a dimer in the center. Rhombs are grouped into the same neighborhood if it takes an equal number of steps to reach the center along the shortest path via edge-connected rhombs. By comparing geometric and topological

4 Materials, experiments, software and modeling

4.1 Diffraction experiments and photo-reactions

4.1.1 Crystal shapes and appearance

The monomer crystal is of brownish to yellowish color which turns to pale yellow upon polymerization. The morphology is derived from a rhombohedron as shown in *Figure 4.1a*. However, these rhombohedra are very often frustum truncated parallel to the *ab*-plane, *Figure 4.1b*. For the system investigated, the threefold axis of all crystal structures runs parallel to the threefold axis of the crystal shapes leading to a very broad size distribution of obtainable sheets, *Figure 4.1c*. Furthermore the occurrence of cleavage plains in the monomer and in the polymer parallel to the *ab*-plane, *i.e.* parallel to the 2DP-sheets, are common, *Figure 4.2*. However, these cleavage planes do not hinder structure analysis. Occasionally, cracks across layers are observed, *Figure 4.2a*, which would further limit the size of obtainable sheets.

4.1.2 Photopolymerization

Photopolymerization was carried out with a custom-made light reactor with a wavelength of 465 nm. This wavelength was chosen because it is in the tail-end of the absorption spectra of anthracene (Bouas-Laurent *et al.*, 2000; Kory *et al.*, 2014b). Tail-end irradiation (Novak *et al.*, 1993; Enkelmann *et al.*, 1993) allows for a more homogeneous light distribution within the crystal during irradiation because of the reduced light absorption. The light reactor was placed in a fridge to cool the high-powered LEDs and to protect the eyes from the intense light. A dry run of the photo-reactor, where a thermometer was placed at the point where the crystals would be, showed that the temperature never exceeded 298 K. As outlined in *Section 2.2.3*, polymerization of any crystal was done step-wise in order to investigate the intermediate steps. During polymerization, crystals were attached to the sample holders which were also used for diffraction experiments.

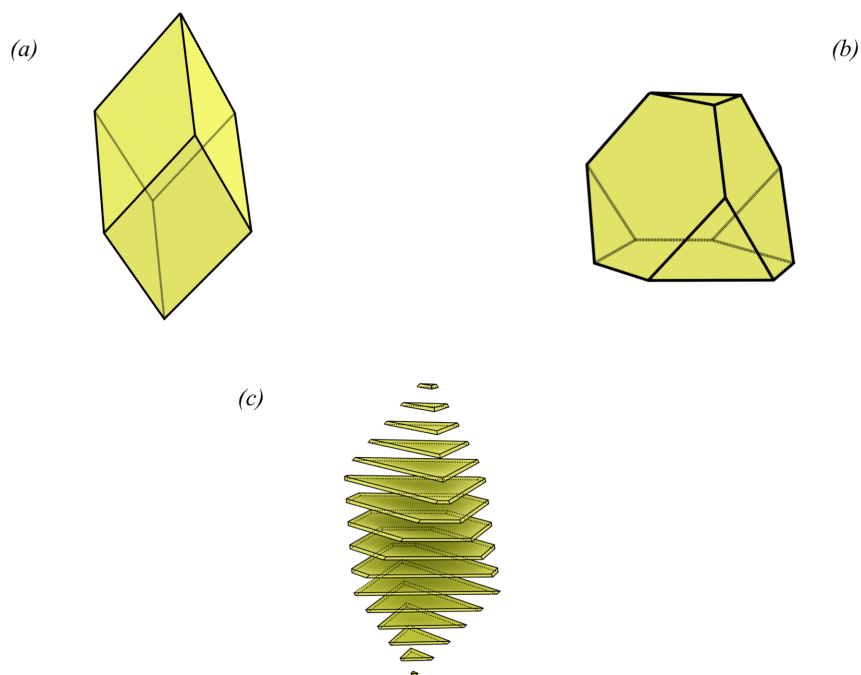


Figure 4.1: Schematic drawing of the typically encountered crystal morphologies which were either shaped like (a) a rhombohedron or (b) frustum truncated rhombohedron. (c) shows how differently sized and differently shaped 2DPs sheets are obtained from the single-crystal shown in (a).

4.1.3 Thermal depolymerization

A common furnace at a temperature of 453 K was used to achieve depolymerization, which was the same temperature as used by Kory *et al.* (2014b). No temperature ramps were used for either heating up or cooling down the crystal. Similar to polymerization, depolymerization was also done step wise, as outlined in *Section 2.2.3*, to investigate the intermediate states. For practical reasons, crystals had to be detached from the sample holders used for diffraction experiments during thermal depolymerization.

4.1.4 Used crystals and handling

To learn about the reproducibility of structural properties within and across batches, several samples were investigated. Three crystals, *CI1*, *CI2* and

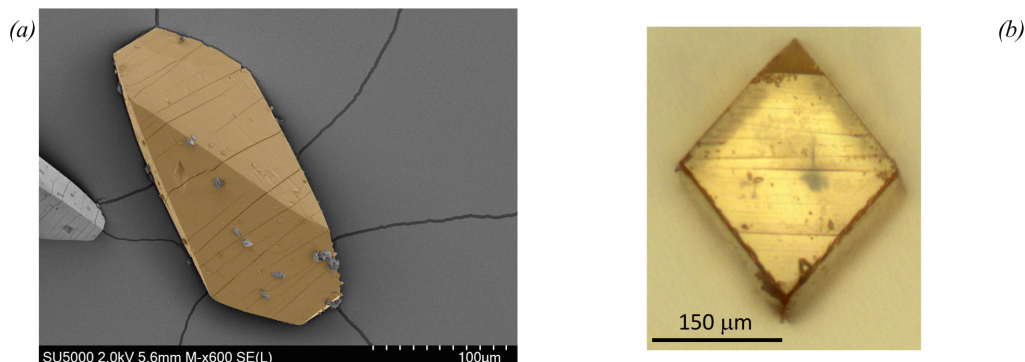


Figure 4.2: (a) scanning electron image of monomer single-crystal (highlighted in yellow) and (b) optical microscope image of a polymer single-crystal. Both images show clearly the rhombohedral-shape and cleavage plains, with (a) showing additional cracks in the crystals which cut across multiple 2DPs sheets. For demonstration purposes, crystals with an atypical large number of cleavage planes are shown. Scanning electron image provided by Gabriele Pagani.

$CI3$, were measured with in-house instruments, while three additional crystals, $CS1$, $CS2$ and $CS3$, were used in synchrotron experiments. The crystals for the in-house and synchrotron experiments were obtained from different crystallization batches. The only difference between these batches is that the latter introduced a higher number of recrystallization steps.

Table 4.1 summarizes the number of used crystals, their dimensions, measurement conditions and the deposition numbers of the average structures in the database of the *Cambridge Crystallographic Data Center*. All crystals were of frustum-truncated rhombohedral shape and chosen by their clarity and sharpness of their Bragg reflections obtained from pre-experiments. The repeated mounting and dismounting of the crystals for thermal depolymerization led to the loss of $CI2$ and $CS3$. $CI3$ was used to complete the polymerization-depolymerization cycle of $CI2$ and was lost after the experiments were finished.

Regardless of the experiment, all crystals were handled under red light whenever possible to prevent accidental and uncontrolled polymerization and measured with instruments that were shaded from ambient light. However, when investigating the change in \bar{C}_n of a separate crystal which was deliberately

Table 4.1: Summary of used crystals. Reproduced with permission from Hofer *et al.* (2018).

ID	Size [μm^3]	Temperature [K]	Polymerization	Depolymerization	2cpy monitored?	CCDC deposition	No. of data sets
<i>CI1</i>	$250 \times 200 \times 200$	100	×		×	1531119 to 1531128	10
<i>CI2</i>	$220 \times 200 \times 170$	298	×	×		1531135 to 1531153	19
<i>CI3</i>	$200 \times 180 \times 180$	298		×		1531129 to 1531134	6
<i>CS1</i>	$600 \times 350 \times 350$	100	×		×	1531155 to 1531162	8
<i>CS2</i>	$700 \times 400 \times 350$	100	×		×	1531163 to 1531169	7
<i>CS3</i>	$600 \times 200 \times 200$	100	×		×	1531170 to 1531175	6

exposed to ambient light of fluorescence lamps and sunlight for two days, no conclusive evidence of polymerization by the ambient light was found.

4.1.5 Single-crystal X-ray diffraction experiments

In-house experiments were done with an *Oxford Diffraction Xcalibur* single-crystal diffractometer in κ -geometry. It was equipped with a conventional sealed tube and MoK_α radiation was selected using a graphite monochromator. The scattered X-rays were detected with a tapered *ONYX* CCD detector. Data sets from *CI1* were collected at 100 K, but equipment failure only allowed for room temperature experiments with *CI2* and *CI3*. Note that the equipment failure only affected the temperature of the diffraction experiments, but did not have any impact on the polymerization and depolymerization conditions. The synchrotron measurements were done at the Swiss-Norwegian Beam Lines at the *European Synchrotron Radiation Facility*, which was equipped with a dipole bending magnet. The monochromatic beam ($\lambda = 0.6935 \text{ \AA}$) was focused on the sample. Bragg data sets were collected at 100 K as 360° φ -scans with step-size of 0.1° and recorded with a *DECTRIS* Pilatus 2M pixel detector (Henrich *et al.*, 2009). Diffuse scattering was collected with the same physical set-up, but with a ten-fold increased exposure time and four 360° φ -scans with a step-size of 0.1° . In total, 56

data-sets Bragg data sets and 21 data-sets diffuse scattering data sets were collected.

4.2 Software

4.2.1 The Yell program

The *Yell* program is the first general-purpose implementation of the 3D- Δ PDF method (Simonov *et al.* 2014b, 2014c) and therefore quintessential for this work. The program is designed to model and simulate the diffuse scattering and the 3D- Δ PDF function of any desired structure. It uses the Levenberg–Marquardt algorithm to refine model data against measured data. Modeling is accomplished by utilizing the three basic types of disorder (displacive disorder, the size-effect and substitutional disorder) to build models of any complexity. The used *Yell* version was 1.2.1 which had to be recompiled against CentOS Linux (release 7.5.1804) to make it functional on ETH’s computing cluster (EULER).

4.2.2 Self-written programs and scripts

Due to the novelty of the 3D- Δ PDF method and *Yell* to investigate diffuse scattering, completely standardized workflows and software pipelines for data processing and evaluation are only partially developed. Problem-specific scripts were written in the *Python* programming language (van Rossum, 1995), version 3, extended by *numpy* (Oliphant, 2006; Van Der Walt *et al.*, 2011) and *scipy* (Oliphant, 2007; Millman and Aivazis, 2011) run from the *Ipython* (Pérez and Granger, 2007) and *JupyterNotebook* (Kluyver *et al.*, 2016) platform, and *bash* version 3.2.57 (Foundation, 2019) programming languages to bridge processing gaps and to perform data analysis. For data processing, the scripts had to handle data transfer between individual programs and semi-automation of these programs. Scripts for data evaluation were written from scratch. They performed tasks such as consistency checks, mathematical conversions as well as simulations.

4.2.3 Third-party software

Data reduction, solution and refinement

Data reduction was done with *CrysalisPro* (Agilent, 2015) for in-house and synchrotron experiments, the latter requiring preprocessing with the *SNBL Toolbox* software (Dyadkin, 2015) and the *FabIO* toolkit (Knudsen *et al.*, 2013). The *OLEX2* (Dolomanov *et al.*, 2009) software suite was used as a working environment and structures were solved using the charge-flipping algorithm (Oszlányi and Sütő, 2004) as implemented in *superflip* (Palatinus and Chapuis, 2007). Structure completion was done by difference Fourier analysis and structure refinement by least-squares fitting against intensities using the program *SHELXL* (Sheldrick, 2015).

Reciprocal space visualizations and reconstructions

Inspecting and evaluation of raw data frames from measurements was done using *CrysalisPro* (Agilent, 2015) and *Albula* (Volker, 2015). Reciprocal space reconstructions for the average structure data-sets was performed in a single step by using *CrysalisPro*. For diffuse scattering data-sets, the orientation matrix was determined with *XDS* (Kabsch, 1988, 2010), the reconstruction was performed with *Meerkat* (Simonov, 2017). Finally, the results were viewed with *PDF Viewer* (Simonov, 2016).

Structure and data visualizations

Structure drawings were made with *CrystalMaker* (Palmer, 2014). Data analysis was done using *OriginPro* (OriginLab, 2015), *PLATON* (Spek, 2003, 2009), *Vesta* (Momma and Izumi, 2011) and the afore mentioned self-written scripts.

4.3 Average structure modeling

4.3.1 Data reduction

Data reduction was straight forward for the in-house experiments, but the occurrence of reflection splitting during the synchrotron experiments required additional processing. Two types of reflection splittings were encountered, one in the ω -direction and one in the 2θ -direction, with the later appearing only during measurements which were concerned with the depolymerization

of *CS2*. Both types of reflection splittings were handled in the same way. If the reflections could not be resolved, integration was done over both maxima. When the reflections could be separated, the data was handled with the multi-crystal approach as implemented in *CrystalisPro*, *i.e.* they were treated as two separate crystals.

When the split reflections in ω direction could be resolved, their typical intensities relative to the main reflections were below 10%. The second domain yielded quality indicators of $R_{\text{int}} > 20\%$, $I/\sigma < 2$ and completeness $\ll 100\%$ which did not allow usage structure analysis and only the better data set was used. However, the unit-cell of the second phase could be obtained and it yielded unit cell constants comparable to the main scattering domain within the statistical errors, indicating that the second scattering domain represents the same structure.

The observed reflection splitting during depolymerization in the 2θ -direction gave much fewer insights. Furthermore, the splitting is much more complex as additional peaks appear on both the low and high angle side of the main reflections along c^* with typical intensities of up to 15% of the main reflection. Indexation of these additional reflections using a multi-crystal model as before failed completely and no information of the additional unit cells could be obtained. Also, their distance to the main reflection increases with increasing 2θ , therefore these additional reflections are not satellite reflections. Unfortunately, no further information could be obtained from them.

4.3.2 Structure solution and refinement

All crystal structures were modeled in space group $R\bar{3}$. Since the fully polymerized crystals were not annealed, transformation to the space group $P\bar{3}_1$ as observed by Kory *et al.* (2014b) was not investigated.

Refinement of the intermediate structures posed some challenges. First, only one average monomer and one average polymer state could be distinguished regardless of the anticipation that molecules having zero, one, two, or three bonded anthracene blades. Corresponding local deviations from the average monomer and polymer states were likely captured by the ADPs. Second, the spatial proximity of the superimposed monomer and polymer

in the average structure led to strong correlations between the ADPs and SOFs. Resolving this problem was essential, since the SOFs directly affect the degree of conversion, which is obtained from the average structure as $\bar{C}_n = \text{SOF}_{\text{Polymer}} = 1 - \text{SOF}_{\text{Monomer}}$.

The measurement series of *CS1* was used to test multiple crystal structure models with different constraints and restraints to monitor their influence on the obtained ADPs and SOFs. The different structure models were evaluated by their physical plausibility, crystallographic reliability indices (R -value) and Hamilton's R -test (Hamilton, 1965). Four models were tested.

- (i) Refinement of the molecules with a rigid body model (Zucker and Schulz, 1982; Schomaker *et al.*, 1968) in the program *Jana* (Petříček *et al.*, 2014). This approach was unsuccessful because *Jana* did not succeed in locating disordered atoms correctly and refining their SOFs.
- (ii) All atoms of the monomer and polymer were described with anisotropic ADPs, which in most cases yielded physically implausible ADPs. Only the models with $\bar{C}_n \approx 0.50$ gave reasonable results.
- (iii) All atoms of the monomer and polymer were refined with isotropic ADPs, which resulted in significantly higher R -values compared to the other models.
- (iv) Only the atoms of the perceived majority of either monomer or polymer were modeled with anisotropic ADPs, while the ADPs of the minority were modeled isotropically. This approach yielded consistent and reasonable results.

For the final data evaluation, model (iv) was used with the exception of data sets where $\bar{C}_n \approx 0.50$ for which model (ii) was used because it yields the best R -value with physically plausible ADPs, presumably because monomer and polymer phases are present in equal amounts. The largest observed difference of \bar{C}_n between the different models is about six percentage points, so the choice of model has only a small influence on the overall result. The refinement of either the monomer or the fully polymerized crystal structure posed no such problems and were modeled in analogy to model (ii).

Throughout this study, the 2cpy was modeled with two rotameric states which differ by 180° , *i.e.* the ring nitrogen atom is distributed with equal probability over the 1- and 3-positions. The sandwiched 2cpy was disordered

and modeled with a three-fold symmetry compatible excentric rotation. It was found that the upright 2cpy is also disordered and modeled with changing orientations and SOFs. In the case of room temperature X-ray measurements, none of the 2cpys could be properly located. Corresponding residual electron densities were eliminated using the *Squeeze* algorithm (Rees *et al.*, 2005).

Although monomer and polymer crystal structures are both polar and chiral, the Flack parameter (Flack and Bernardinelli, 2008) did not refine to an accurate enough value to permit assumptions about the crystals chirality, which is an expected result for light element structures.

4.4 Real structure modeling

4.4.1 Data selection

For modeling and refinement purposes, only a part of the data-sets that were collected for real-crystal structure analysis was used because of time constraints. The selection of data-sets was based on the following three criteria. First, all used data-sets should be from the same crystal in order to avoid ambiguity originating from variations in crystal quality and batch quality. Second, the recorded frames should have the highest quality possible. The quality was evaluated on the basis of frames with high Bragg and diffuse scattering intensities, negligible reflection splitting and a minimum of parasitic scattering. Finally, the structure refinement results from the corresponding average structures were also taken into account. They should be as good as possible, because these results formed the basis for the real crystal structure model. The data-sets from *CS1* fit these criteria best and were therefore selected, despite some minor reflection splitting. Due to time constraints, however, it was only possible to evaluate three data sets from *CS1*, with conversion ratios of 0, 0.22 and 0.44, respectively.

4.4.2 Data reduction

During the measurements, the almost ubiquitous air scattering and scattering from the sample holder was also recorded. This provided a challenge because

background correction for diffuse scattering data is a non-standard problem. This was counteracted by collecting empty frames, *i.e.* by measuring an empty sample holder under the same conditions as for a proper measurement. The average of all empty frames yielded the background frame. This frame was normalized to the flux of each data frame and then subtracted from each data frame. However, there was still a residual convex and concave background afterwards. One of the sources of the former is most likely caused by more resin on the crystal than during the actual background measurement or uncorrelated disorder, while the latter was most likely caused by Compton scattering.

The three-dimensional reciprocal space reconstruction with *meerkat* included symmetry averaging according to Laue group $\bar{3}$. Removing the Bragg reflections and gaps in the detected areas was done by applying weights to each voxel, where all Bragg positions and detector gaps were assigned with a weight of zero and all other voxels with unit weights.

4.4.3 Refinement strategy

As the refinement of diffuse scattering in *Yell* is computationally expensive, several technical measures were taken to reduce wall-clock computation time as much as reasonable possible. As explained below, there were four main factors that contributed to the reduction in computing time.

First, the voxel size of the reciprocal space data against which the model was refined, was chosen to be $0.2 \times 0.2 \times 0.2$ units of hkl with $210 \times 210 \times 310$ voxels. This size kept memory consumption low while preserving the details of diffuse scattering. In addition, this size ensured that all significant signals in the PDF space were sufficiently resolved. The selected values covered the reciprocal space between $-21 \leq h < +21$, $-21 \leq k < +21$, and $-31 \leq l < +31$, which is about three indices less in each direction than recorded. The truncation removed areas that were not covered by the detector or did not contain significant amounts of diffuse scattering. This made it possible to cover the PDF space within the $-2.50 \leq u \leq +2.48$, $-2.50 \leq v \leq +2.48$ and $-2.50 \leq w \leq +2.48$ limits, which was sufficient to resolve all observed features.

Second, the final model would have initially required the calculation of about 400 000 atom pairs, but this number was drastically reduced by the introduction of molecular form factors⁶, which are an undocumented feature in *Yell*. Instead of modeling each individual atom, groups of atoms that behave like a rigid body are regarded as a unit with its own form factor. While molecular form factors require increased computational effort at the beginning of refinement, they reduced the number of pairs required to about 1 200, which shortens the computation time in the long run. The drawback of using molecular form factors is that the used version of *Yell* only allowed translations but not librations of molecular scatterers. That was initially thought to be problematic for the template molecule because the template's ADP suggested a crescent-type displacement which would have required librations. However, an atomistic model showed that there are no significant differences within the given displacement magnitudes in the diffuse scattering when modeling the displacement with a linear approximation versus a true libration.

Third, *Yell*'s approximate method for calculating the diffuse scattering was used, which offers a speed improvement by reducing accuracy (Simonov *et al.*, 2014b). It is based on a variation of the fast Fourier transform algorithm developed by Sayre (1951) and Ten Eyck (1977) for structure factor calculations. For that purpose, the interatomic vector between an atomic or molecular pair is split into two components. The first is the grid component and describes the 3D- Δ PDF densities that can be resolved in the data. The second is the residual component, which is the difference between the 3D- Δ PDF densities of the original vector and the grid component. A sampling box is assigned to the grid component and the Fourier transform is applied to the contents of the sampling box. The result is multiplied by the residual component and a phase factor that takes possible shifts in the grid component into account (Simonov *et al.*, 2014b). This procedure is applied to all vector pairs and the sum of the results yields the 3D- Δ PDF, from which the diffuse scattering is obtained via the inverse Fourier transform. The size of the sampling box is a critical parameter for this calculation method as all atoms of a molecular scatterer should fit inside the box. If it is too small, artifacts and refinement errors are introduced and if it is too large, computing time savings will be insignificant. Additionally, its edge length should be

⁶*Molecular form factor* is a term to describe a group of atoms that behave like a rigid body, regardless of chemical bonding.

a power of 2 to maximize the speed gain. The final size of 64 pixels (about 30 Å) was chosen based on the knowledge of size of the molecular scatterers and through trial and error as artifacts were observed when using smaller box sizes.

Finally, the used version of *Yell* is limited in memory allocation to 16 GB. The refinement of the complete model requires the least-squares algorithm to fit all of the about 4 000 model parameters, which consumes about 500 GB of memory when all parameters are optimized at the same time. This hard constraint forced the division of the model into multiple blocks so that only a subset of the 4 000 parameters were refined together. They were divided in up to 43 subsets which allowed the use of multiple computation nodes on EULER to achieve a quasi-parallelization of the refinement. Choosing these subsets was based on the proximity of signals in PDF-space and some trial and error. As a rule of thumb, parameters referring to 3D- Δ PDF signals close together were refined in the same block in order to recognize numerical correlations. However, the hard 16 GB memory constraint made this occasionally impossible, because the number of parameters influencing signals in relative close proximity to each other would have exceeded the memory limit. Choosing the wrong parameters for a block can lead to overfitting of parameters or artifacts. Although several blocks could be refined simultaneously on EULER, numerical correlations across blocks could not be resolved. In order to find numerical parameter correlations across blocks, the parameters per block were changed after each full refinement cycle.

While these measures entailed several simplifications and limitations, they reduced the wall-clock computing time by about one to two orders of magnitude. This allowed for 10 to 15 least-squares iterations per refinement to run within 16 hours on EULER to refine all model parameters. Around 25 refinement cycles for each investigated degree of conversion were required to achieve convergence of the least-squares fit.

4.4.4 Model design principles

The technical limitations described in the last chapter as well as some practical considerations had to be taken into account when creating the real crystal structure model and are explained in this chapter.

Background correction for diffuse scattering data is still a non-standard and non-trivial problem, because, unlike Bragg scattering, diffuse scattering is not restricted to integer positions in reciprocal space, which makes the separation of diffuse scattering and the background difficult. An additional dummy atom was added and the background was modeled as uncorrelated disorder. Uncorrelated substitutional disorder and uncorrelated displacive disorder of this dummy atom in the zeroth neighborhood modelled the convex and concave part of the background, respectively. The magnitude of each uncorrelated disorder was refined against the data and yielded a good fit of the residual background.

Two different kinds of molecular scatterers were defined for modeling disorder, one for displacive and one for substitutional disorder. For displacive disorder, the molecular scatterer was defined as the asymmetric unit of the monomer molecules and their polymerized counterparts, as seen in *Figure 4.3a, b*. In the context of this work, the asymmetric unit of the monomer molecule will be referred to as *blade* and the asymmetric unit of the polymerized counterpart will be referred to as *half-dimer*. A total of five such molecular scatterers were required, one each for M_S , M_T , P_S , P_T and the template. Molecular scatterers for substitutional disorder were defined by combining either two blades or two half-dimers directly opposite each other, *Figure 4.3c, d*. In the context of this work, these structural units will be referred to as *blade pair* and *dimer*, respectively. Two such molecular scatterers were required, one for the monomer and one for the polymer substructure.

Using molecular scatterers imposed some additional restrictions on the modeling process. Rotational and inversion symmetry operations for molecular scatterers are not implemented in the used *Yell* version and had to be implemented by hand. Each molecular scatterer required the definition of a molecular displacement parameter (MDP). These were calculated from the average structure by using *SHELX* (Sheldrick, 2015) through constraining the ADP matrices of all atoms belonging to the same blade or half-dimer to be equivalent. The polymer substructure of the data-set with a \bar{C}_n of 0.22 was modeled with isotropic MDPs in the average structure rather than with anisotropic MDPs as all other substructures. However, it was implemented in *Yell* with anisotropic MDPs in order to fully model the interactions with

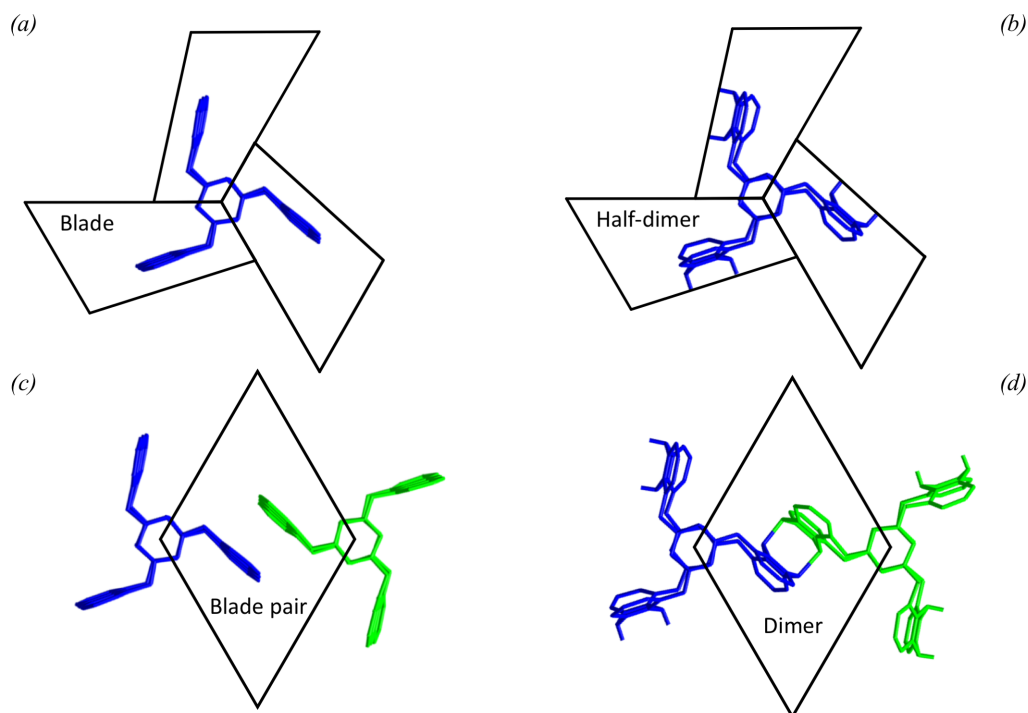


Figure 4.3: Two conceptual subdivisions of the monomer and polymer structures to model and understand the occurring disorder. For the first type of substitution, the asymmetric units of M_S , M_T , and the template are used and referred to as blade, shown exemplary for (a) M_S . Similarly, the asymmetric units of P_S , P_T are used and referred half-dimer, shown exemplary for (b) P_S . For the second type, two directly neighboring asymmetric units of different (c) monomers and (d) their polymerized counterparts were combined for usage, referred to as blade pair and dimer. Note that these two units also form the basis of the rhombille-tiling representation, see *Section 3.8*.

its neighbors. Finally, distortions within a molecular scatterer could not be modeled.

Displacive disorder could be modeled up to the third neighbor inside and outside the layer, which puts the longest interatomic vectors into the range of 40 to 45 Å which is in agreement with the observed 3D- Δ PDF densities. Substitutional disorder was modeled up to a subset of the third topological neighbors with the shortest geometrical distances within the layer. Substitutional disorder across layers was observed and modeled only in directly adjacent layers, *i.e.* in layers directly above and below. Within these layers,

correlations were modeled up to the second topological neighbor moieties, with the longest interatomic vectors ranging from 25 to 30 Å. No significant contributions from the size effect or the solvent molecules were found, and therefore neither was included in the model. Displacive and substitutional disorder were modeled with two fundamentally different strategies which are described in detail in *Section 4.4.5* and *Section 4.4.6*.

None of the solvent molecules was included in the final model, since the first *Yell* models showed that their contributions to the total diffuse scattering intensities were several magnitudes weaker than the contributions of the monomer molecules and their polymerized counterparts.

4.4.5 Displacive Disorder

Displacive disorder is the concerted movement or the absence thereof between a pair of blades, half-dimers or combinations thereof. The theory is similar to normal mode analysis (Cyvin, 1968) and is put into context for diffuse scattering analysis in the following paragraphs. Understanding displacive disorder requires the knowledge of the mean fluctuations U_{ij} of each of the pair's members, *i.e.* the average displacement of a moiety from the ideal position. U is a symmetric, positive definite matrix obtained via Bragg scattering from standard X-ray experiments and is defined as

$$U_{ij} = \langle u_i u_j \rangle = \begin{bmatrix} \langle \delta x_i^2 \rangle & \langle \delta x_i \delta y_j \rangle & \langle \delta x_i \delta z_j \rangle \\ & \langle \delta y_i^2 \rangle & \langle \delta y_i \delta z_j \rangle \\ & & \langle \delta z_i^2 \rangle \end{bmatrix} = \begin{bmatrix} U_{11} & U_{12} & U_{13} \\ & U_{22} & U_{23} \\ & & U_{33} \end{bmatrix} \quad (4.1)$$

where u_i and u_j denote small displacements for the average positions along a given axis. The terms in angle brackets denote time and space averages. The ellipsoid of joint atomic displacement between two moieties A and B is described by

$$\begin{aligned} S_{ij}^{AB} &= \langle (u_i^A - u_i^B) (u_j^A - u_j^B) \rangle \\ &= \langle u_i^A u_j^A \rangle + \langle u_i^B u_j^B \rangle - \langle u_i^A u_j^B \rangle - \langle u_j^A u_i^B \rangle \end{aligned} \quad (4.2)$$

where u^A and u^B are displacements for moiety A and B of the two correlated sites. Similar to *Equation 4.1*, the joint displacements can be expressed as covariance matrix by

$$\begin{aligned} U_{ij}^{AB} = \langle u_i^A u_j^B \rangle &= \begin{bmatrix} \langle \delta x_i^A \delta x_j^B \rangle & \langle \delta x_i^A \delta y_j^B \rangle & \langle \delta x_i^A \delta z_j^B \rangle \\ \langle \delta y_i^A \delta x_j^B \rangle & \langle \delta y_i^A \delta y_j^B \rangle & \langle \delta y_i^A \delta z_j^B \rangle \\ \langle \delta z_i^A \delta x_j^B \rangle & \langle \delta z_i^A \delta y_j^B \rangle & \langle \delta z_i^A \delta z_j^B \rangle \end{bmatrix} \\ &= \begin{bmatrix} U_{11}^{AB} & U_{12}^{AB} & U_{13}^{AB} \\ U_{21}^{AB} & U_{22}^{AB} & U_{23}^{AB} \\ U_{31}^{AB} & U_{32}^{AB} & U_{33}^{AB} \end{bmatrix} \end{aligned} \quad (4.3)$$

where U^{AB} is the correlated displacement covariance between moiety A and B . The U^{AB} matrix needs to be neither positive definite nor symmetric. Using *Equation 4.1* and *Equation 4.3* to simplify *Equation 4.2* yields

$$S_{ij}^{AB} = U_{ij}^A + U_{ij}^B - U_{ij}^{AB} - U_{ji}^{AB} \quad (4.4)$$

which is the notation used henceforth. Note that S_{ij}^{AB} is derivable from *Equation 2.5* through the term β_{uvw}^{AB} as

$$\beta_{uvw}^{AB} = 2\pi^2 a_i^* a_j^* S_{ij}^{AB} \quad (4.5)$$

where a_i^* and a_j^* are the lengths of the corresponding reciprocal space vectors. Although it would be desirable to obtain U^{AB} , diffuse scattering gives only access to the S_{ij}^{AB} matrix. When rearranging *Equation 4.4*, it is obvious that only the symmetric part of U^{AB} is unambiguously recovered. For the diagonal elements of U^{AB} this is achieved by rearranging *Equation 4.4* to

$$U_{ii}^{AB} = \frac{U_{ii}^A + U_{ii}^B - S_{ii}^{AB}}{2} \quad (4.6)$$

which uniquely provides all diagonal elements U_{ii}^{AB} . However, rearranging *Equation 4.4* to obtain the off-diagonals elements of U^{AB} yields

$$U_{ij}^{AB} + U_{ji}^{AB} = U_{ij}^A + U_{ij}^B - S_{ij}^{AB} \quad (4.7)$$

which shows that only the sum of the elements U_{ij}^{AB} and U_{ji}^{AB} is known. No further information about the off-diagonals could be gained except for the inequality

$$|U_{ij}^{AB}| \leq \sqrt{U_{ii}^A U_{jj}^B} \quad (4.8)$$

which must be fulfilled, because otherwise correlations would exceed +1 or -1. This inequality, since $|a + b| \leq |a| + |b|$, leads to

$$|U_{ij}^{AB} + U_{ji}^{AB}| \leq 2\sqrt{U_{ii}^A U_{jj}^B} \quad (4.9)$$

which must also be fulfilled.

Within the scope of this project, attempts were made to gain further insight into the properties or the relationships of the off-diagonal elements, but failed ultimately and are summarized in the appendix. For the final models, $U_{ij}^{AB} = U_{ji}^{AB}$ was assumed. The consequence of this assumption is that additional symmetry in the correlations was introduced as no other natural assumptions could be made about the asymmetry of U^{AB} . As a result, potentially independent displacements are constrained to be the same.

Parameterization of the displacive disorder in the model is straightforward. A single U^{AB} matrix with six independent parameters is required to describe the correlated displacements between a pair of blades, half-dimers and their combinations per conversion step. For the partially polymerized structures, the displacive disorder of the longest interatomic vectors was modelled with only one single value for the diagonal and one single value for the off-diagonal due to the weak signal strength. As both monomer molecules, their polymerized counterparts and the template are composed of three molecular scatterers each (*i.e.* three blades are needed to form a monomer molecule), nine U^{AB} matrices are required to describe the interactions between two monomers, their polymerized counterparts, the template, or combinations thereof. There are two exceptions to this rule. First, intra-molecular displacements required only one matrix per molecule because each molecule is located on a threefold symmetry axis. Second, between directly neighboring M_S and P_T as well as P_S and M_T only eight matrices are required because a half-dimer opposite of a blade is physically impossible. *Figure 4.4* shows examples of subsets of such pairings.

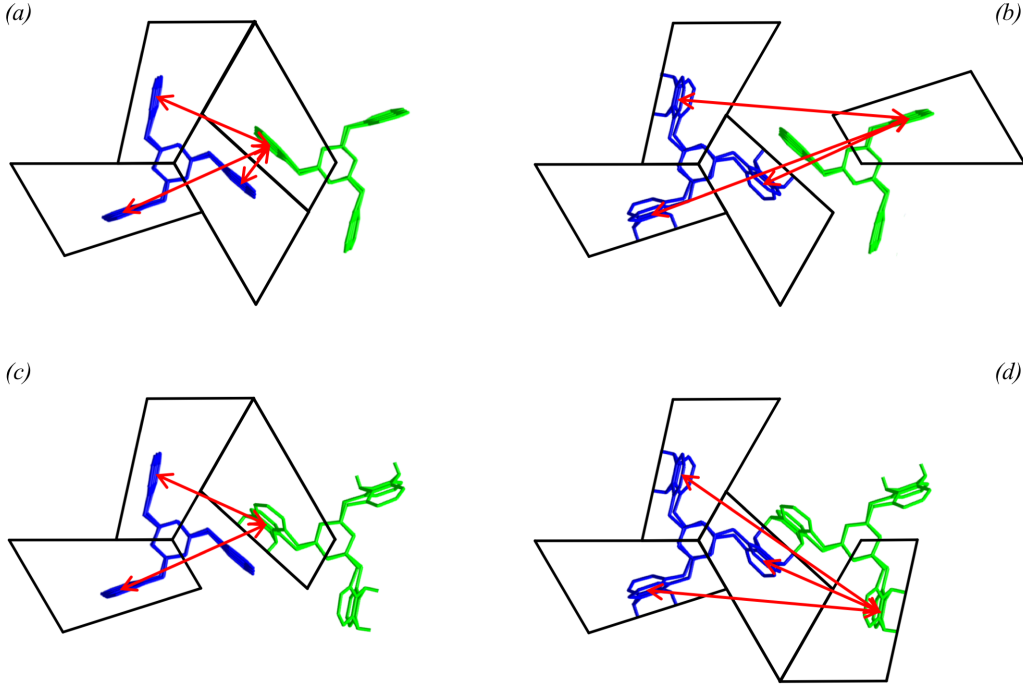


Figure 4.4: Several examples of how blades and half-dimers are paired. Some of the possible pairings are between (a) all blades of M_S with one blade of M_T , (b) all half-dimers of P_S with a single blade from M_T , (c) all possible pairings between the blades from M_S with a half dimer from P_T (note that it is physically impossible to have a blade directly next to a half-dimer and vice versa) and (d) all half-dimers of P_S with a half-dimer of P_T .

4.4.6 Substitutional disorder

Substitutional disorder is modeled via the joint probability distribution of blade pairs and dimers. This is achieved in two steps. First, a lattice vector r_{AB} is defined between each pair of sites which contain either a dimer or blade pair. Second, for each such vector r_{AB} , a joint probability matrix $J(r_{AB})$ is defined as

$$J(r_{AB}) = \begin{bmatrix} p_{DD} & p_{AD} \\ p_{DA} & p_{AA} \end{bmatrix} \quad (4.10)$$

where p_{ij} is the joint probability that both moieties i and j are present at the same time. i and j are either a blade pair (A) or a dimer (D). Joint probabilities for two entities should be consistent with the marginal probabilities

$$\begin{aligned} C_1 &= p_{11} + p_{12} = p_{11} + p_{21} \\ C_2 &= p_{22} + p_{12} = p_{22} + p_{21} \\ C_1 + C_2 &= 1 \end{aligned} \quad (4.11)$$

which can be reformulated in the context of two-dimensional polymerization as

$$\begin{aligned} \bar{C}_n &= p_{DD} + p_{AD} = p_{DD} + p_{DA} \\ 1 - \bar{C}_n &= p_{AA} + p_{AD} = p_{AA} + p_{DA} \end{aligned} \quad (4.12)$$

with \bar{C}_n being the a priori known degree of conversion. This simplifies *Equation 4.10* to

$$J(r_{AB}) = \begin{bmatrix} p_{DD} & \bar{C}_n - p_{DD} \\ \bar{C}_n - p_{DD} & 1 - 2\bar{C}_n + p_{DD} \end{bmatrix} \quad (4.13)$$

and shows that the joint probability between two correlated sites can be represented by one independent variable. p_{DD} was chosen because it describes the probability to find two dimers separated in space by r_{AB} which in turn describes the current state of polymerization propagation. One such parameter per pair of blades would be required to describe all of the occurring substitutional disorder. However, visual inspection of the experimental 3D- Δ PDF maps and statistical significance tests such as Hamilton's R-test (Hamilton, 1965) showed that the signal differences between symmetry-independent neighbors, that share the same geometrical and topological distance, were too insignificant to be of any useful meaning. Therefore, the topological super group $R\bar{3}m$, as defined in *Section 3.8*, was used for modeling instead of the geometrical space group $R3$. This allowed additional symmetry constraints on the joint probabilities and instead of the local geometrical site symmetry 1 between correlated sites, site symmetry $2/m$ was assumed, *Figure 4.5*. These

simplifications made it possible to use only eight parameters to model all of the observed substitutional disorder.

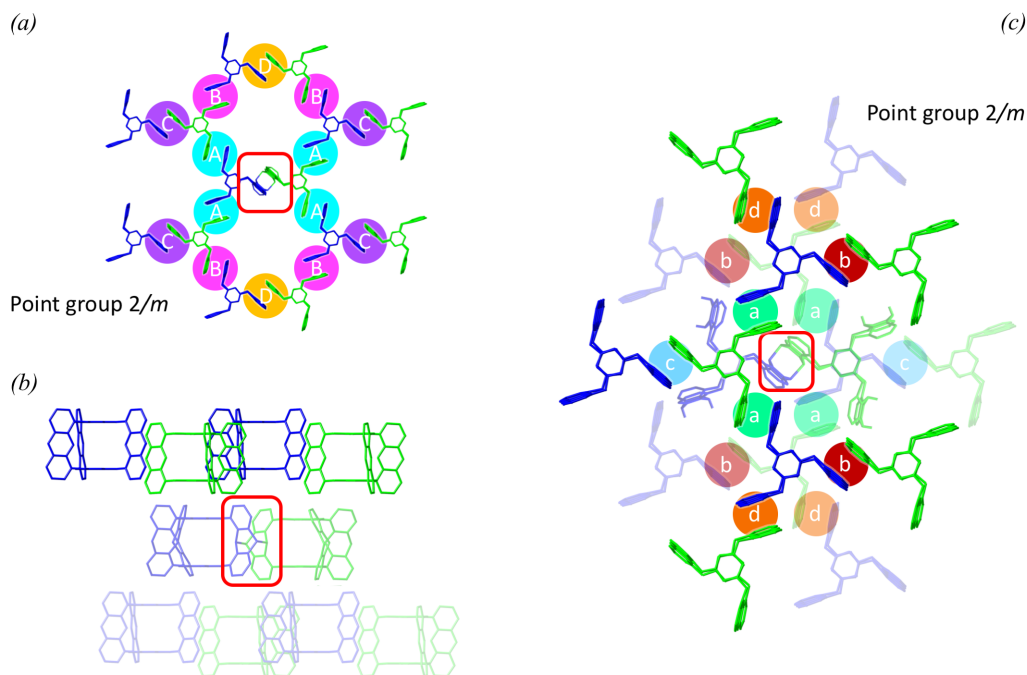


Figure 4.5: Visualization of the introduced substitutional correlation symmetry used for refinement. (a) shows the topological $2/m$ site symmetry for in-layer correlations with respect to the site highlighted by the red box, with the two-fold rotation axis running from top to bottom of the picture. Note that without considering additional layers, site symmetry $mm2$ is mimicked. (b) Side view of the local molecular arrangement above and below of the site highlighted by a red box in (a) and (c). (c) Top view of (b), highlighting the topological $2/m$ site symmetry of correlated sites. Color saturation indicates different height offsets along the c -axis. The labels 'A' to 'D' and 'a' to 'd' indicate increasing geometrical and/or topological distances of correlated sites within (upper case) and out-of layer (lower case).

5 Results

5.1 Average crystal structure

5.1.1 Photopolymerization

Refinements of the crystal structures during polymerization gave acceptable R -values^{7,8}, given the amount of disorder and overlaps: $R1 = 0.0641 / 0.131 / 0.0922$ (min / max / mean) and $wR2 = 0.184 / 0.440 / 0.302$. *Table 5.1, 5.2* show each a selection of refinement results from the in-house and synchrotron experiments, respectively.

Figures 5.1, 5.2 depict the irradiation-time dependent polymerization propagation and the associated changes in the unit-cell parameters at low and at room temperature. In contrast to the in-house measurements, complete polymerization with the crystals measured at the synchrotron facility was not achieved because the rate of polymerization turned out to be slower than expected from preceding in-house measurements, *Figures 5.1a, 5.2a*. The a -axis steadily increases upon polymerization, *Figures 5.1b, 5.2b*. The same behavior is in general visible for the c -axis, but here room temperature measurements show a sudden decrease once full conversion is achieved, *Figure 5.2c*. This behavior may also be present at low temperatures, *Figure 5.1c* data set *C11*, but due to the relatively strong variance of the lattice parameters, the effect is not so prominent. There are significant fluctuations in the unit-cell parameters, which are probably caused by systematic errors introduced by reflection splitting or because of uncertainties in the determination of \bar{C}_n , but a clear trend is visible. In first approximation, unit-cell parameters increase linearly as a function of \bar{C}_n . Only in the case of *CS3* the unit-cell parameters appear to behave differently, *i.e.* they increase exponentially.

The ADPs of all atoms increase during polymerization with respect to the fresh crystals, with the U_{33} parameter showing the largest increase by a factor of up to 2 in $M_S/M_T/P_S/P_T$ and up to 3 in the template, *Figure 5.3*. After \bar{C}_n has reached ≈ 0.70 , the ADPs of the low- and room-temperature

$${}^7R1 = \frac{\sum ||F_o| - |F_c||}{\sum |F_o|}$$
$${}^8wR2 = \left\{ \frac{\sum [w (F_o^2 - F_c^2)^2]}{\sum [w (F_o^2)^2]} \right\}^{\frac{1}{2}}$$

Table 5.1: Selected refinement data from in-house measurements. This table shows two typical low temperature measurements at low and high \bar{C}_n and two typical room temperature measurements from polymerization and depolymerization experiments. Please note that in CI2 the solvent molecules were squeezed from the structure which leads to discrepancies between CI1 and CI2 in parameters such as the empirical formula or calculated density.

	CI1	CI1	CI2	CI2
\bar{C}_n [%]	12.1	66.9	100	51.5 (depolymerization)
Empirical formula	$C_{168}H_{88}N_{26}O_{18}$	$C_{168}H_{88}N_{26}O_{18}$	$C_{144}H_{72}N_{18}O_{18}$	$C_{144}H_{72}N_{18}O_{18}$
Formula weight	2760	2760	2342	2342
Temperature K	100	100	293	293
Crystal system	trigonal	trigonal	trigonal	trigonal
Space group	$R3$ (No. 146)	$R3$ (No. 146)	$R3$ (No. 146)	$R3$ (No. 146)
a [Å]	19.3629(2)	19.4258(4)	19.5983(3)	19.5565(4)
c [Å]	28.9110(4)	29.1409(10)	29.2593(18)	28.7123(12)
Volume [Å ³]	9387.1(3)	9523.4(5)	9732.6(7)	9510.0(6)
Z	3	3	3	3
ρ_{calc} [mg mm ⁻³]	1.464	1.443	1.199	1.227
μ [mm ⁻¹]	0.099	0.097	0.081	0.083
$F(000)$	4266	4266	3618	3618
Radiation source	MoK α	MoK α	MoK α	MoK α
Wavelength [Å]	0.71073	0.71073	0.71073	0.71073
θ range for data collection	4.210 - 29.675	4.196 - 29.644	4.151 - 29.507	4.155 - 29.559
Index ranges	$-26 \leq h \leq 26$ $-26 \leq k \leq 26$ $-39 \leq l \leq 35$	$-26 \leq h \leq 26$ $-26 \leq k \leq 26$ $-36 \leq l \leq 39$	$-26 \leq h \leq 26$ $-27 \leq k \leq 26$ $-39 \leq l \leq 40$	$-26 \leq h \leq 26$ $-27 \leq k \leq 26$ $-37 \leq l \leq 38$
Reflections collected	66224	61824	68330	69723
Independent reflections	10364	10516	10853	10707
R_{int}	0.0318	0.0383	0.0748	0.0852
Parameters	776	768	541	702
Goodness-of-fit on F^2	1.030	1.299	0.809	0.763
Final R values [$I \geq 2\sigma(I)$]	$R_1 = 0.0714, wR_2 = 0.1931$	$R_1 = 0.1094, wR_2 = 0.3179$	$R_1 = 0.0648, wR_2 = 0.1832$	$R_1 = 0.0689, wR_2 = 0.1885$
Final R values (all data)	$R_1 = 0.0943, wR_2 = 0.2146$	$R_1 = 0.1645, wR_2 = 0.3641$	$R_1 = 0.1563, wR_2 = 0.2124$	$R_1 = 0.1968, wR_2 = 0.2331$
Largest diff. peak/hole [eÅ ⁻³]	0.46/-0.35	0.74/-0.36	0.19/-0.16	0.20/-0.14
Flack parameter	-0.1(3)	0.2(5)	0.2(7)	-0.2(8)

Table 5.2: Selected refinement data from synchrotron measurements. This table shows from left to right the best, two typical and the worst structure refinement data from the synchrotron experiments.

	CS1	CS1	CS2	CS3
\bar{C}_n [%]	0	88.5	32.6	70.2
Empirical formula	$C_{168}H_{88}N_{26}O_{18}$	$C_{168}H_{88}N_{26}O_{18}$	$C_{168}H_{88}N_{26}O_{18}$	$C_{168}H_{88}N_{26}O_{18}$
Formula weight	2760	2760	2760	2760
Temperature K	100	100	100	100
Crystal system	trigonal	trigonal	trigonal	trigonal
Space group	$R\bar{3}$ (No. 146)	$R\bar{3}$ (No. 146)	$R\bar{3}$ (No. 146)	$R\bar{3}$ (No. 146)
a [Å]	19.32796(10)	19.5350(3)	19.3587(2)	19.4588(4)
c [Å]	28.85800(14)	29.0439(9)	28.8970(5)	29.0665(16)
Volume [Å ³]	9336.17(11)	9598.7(4)	9378.6(3)	9531.4(7)
Z	3	3	3	3
ρ_{calc} [mg mm ⁻³]	1.472	1.432	1.465	1.442
μ [mm ⁻¹]	0.094	0.092	0.094	0.092
$F(000)$	4266	4266	4266	4266
Radiation source	Synchrotron	Synchrotron	Synchrotron	Synchrotron
Wavelength [Å]	0.6935	0.6935	0.6935	0.6935
θ range for data collection	1.818 - 32.259	1.803 - 29.701	1.816 - 32.125	1.805 - 32.198
Index ranges	$-19 \leq h \leq 19$ $-29 \leq k \leq 29$ $-43 \leq l \leq 43$	$-19 \leq h \leq 19$ $-27 \leq k \leq 27$ $-41 \leq l \leq 41$	$-28 \leq h \leq 28$ $-19 \leq k \leq 19$ $-43 \leq l \leq 43$	$-29 \leq h \leq 29$ $-19 \leq k \leq 19$ $-44 \leq l \leq 43$
Reflections collected	25513	21241	24434	24674
Independent reflections	13827	11494	13458	13829
R_{int}	0.0564	0.0268	0.0351	0.0660
Parameters	644	740	778	777
Goodness-of-fit on F^2	1.066	1.062	1.133	1.066
Final R values [$I \geq 2\sigma(I)$]	$R_1 = 0.0656, wR_2 = 0.1794$	$R_1 = 0.0897, wR_2 = 0.2873$	$R_1 = 0.0986, wR_2 = 0.3021$	$R_1 = 0.1313, wR_2 = 0.3639$
Final R values (all data)	$R_1 = 0.0677, wR_2 = 0.1841$	$R_1 = 0.1160, wR_2 = 0.3064$	$R_1 = 0.1214, wR_2 = 0.3350$	$R_1 = 0.1947, wR_2 = 0.4404$
Largest diff. peak/hole [eÅ ⁻³]	0.54/-0.65	0.46/-0.37	0.50/-0.42	0.44/-0.36
Flack parameter	-0.5(6)	0.0(8)	1.3(10)	-3.5(10)

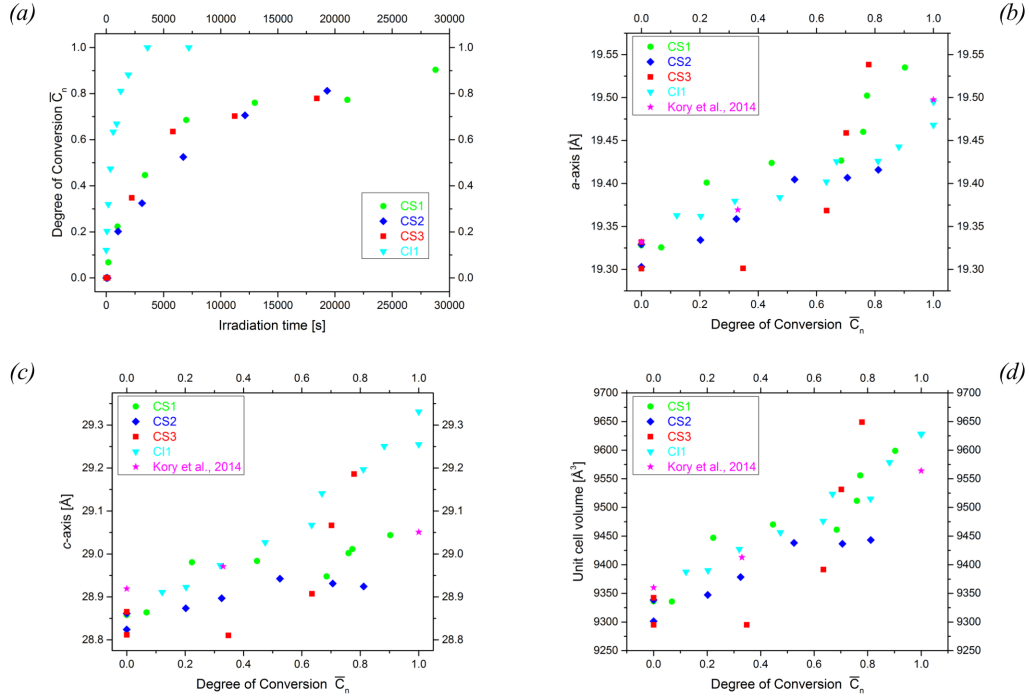


Figure 5.1: (a) Irradiation-time dependent conversion from monomer to polymer at 100 K. Changes in the (b) a -axis, (c) c -axis and (d) unit cell volume during polymerization propagation at 100 K. For comparison, the results from Kory *et al.* (2014b) are included. Figure reproduced with permission from Hofer *et al.* (2018).

measurements are of about the same magnitude. At that point, the ADPs also show the largest displacement because they decrease afterwards to a factor of 1.5 to 2 of their original value upon full conversion.

During polymerization M_S , M_T , P_S , P_T and the template also change their relative offsets along the c -axis, *Figures 5.4a,b, 5.5a,b*. Since the formation of anthracene dimers forces laterally neighbored molecules to occupy similar positions along the c -axis, polymer layers are less puckered than their monomer counterparts, *Figures 5.4c,d, 5.5c,d*. The decrease in surface roughness during polymerization correlates with an increase of the intermolecular distances in the columns, *Figures 5.4a,b, 5.5a,b*.

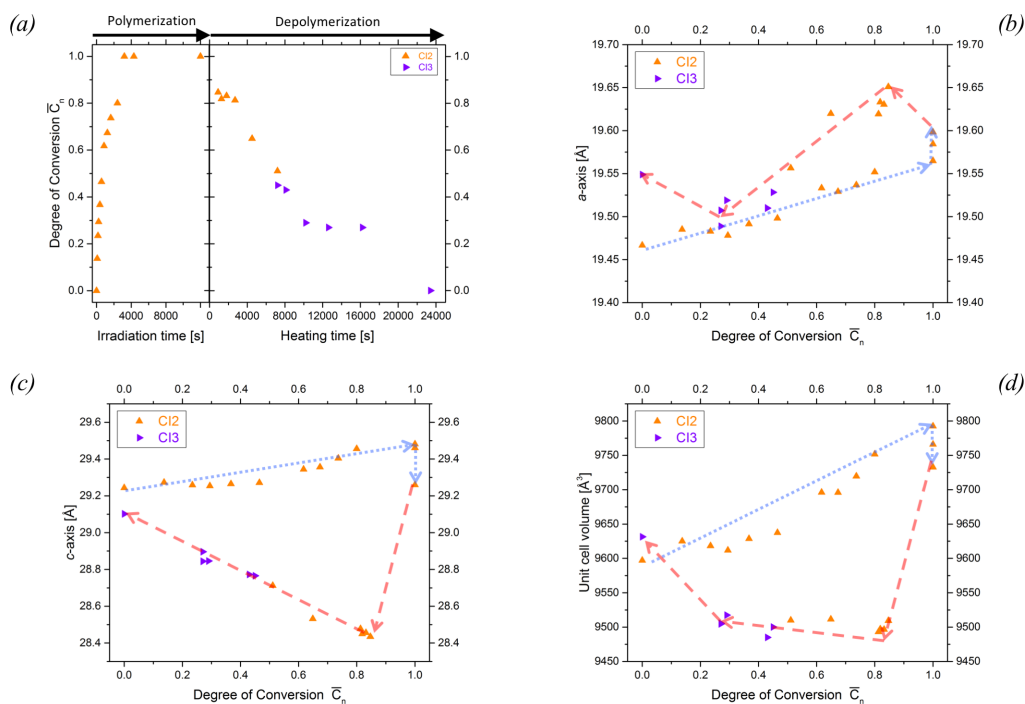


Figure 5.2: (a) Irradiation-time dependent conversion from monomer to polymer and heating-time dependent conversion from polymer to monomer obtained from room temperature X-ray experiments. Changes in the (b) a -axis, (c) c -axis and (d) unit cell volume upon polymerization and depolymerization propagation at room temperature. The arrows in (b), (c) and (d) are guides for the eyes, dotted arrows represent polymerization and dashed arrows represent depolymerization. Figure modified with permission from Hofer *et al.* (2018).

5.1.2 Thermal depolymerization

Crystal structure refinements concerning depolymerization turned out to be more challenging and resulted in less complete models. This is reflected in higher R -values: $R1 = 0.959 / 0.123 / 0.114$ (min / max / mean) and $wR2 = 0.337 / 0.423 / 0.380$. An accurate determination of \bar{C}_n from the crystal $CS2$ during depolymerization could not be accomplished. Using multiple ADP models to narrow down \bar{C}_n , as described in *Section 4.3.2*, revealed in some cases differences in \bar{C}_n by more than 60 percentage points for the same data set. An explanation for this strong inconsistency could not be

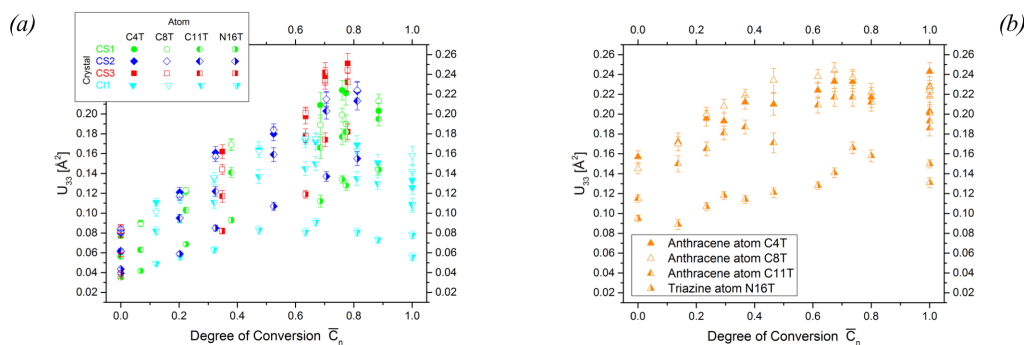


Figure 5.3: Change of the U_{33} parameter of some selected atoms in the template's anthracene and triazine moieties during polymerization at (a) 100 K and (b) room temperature. Symbol color and shape refer to the data set, the symbol interior to an atom. Atom $C4T$ (anthracene moiety, filled symbol) represents the largest, $N16T$ (triazine moiety, right-half filled symbol) the smallest and $C8T$ and $C11T$ (both in the anthracene moiety, open and left-half filled symbols, respectively) represent a typical change during polymerization. Reproduced with permission from Hofer *et al.* (2018).

found. The results are therefore considered as unreliable and not reported for that particular data set. In addition, very weak residual electron densities were observed. They resemble the shape of a monomer molecule slightly shifted along the c -axis up to about 1.3 \AA with respect to M_T , *Figure 5.6*. This residual electron density disappears during the first steps of depolymerization. The shape makes it implausible, that the residual electron density belongs to the polymer as the typical kink in the anthracene dimer is not observed. Inserting and refining an additional molecule at this position failed, probably because the corresponding molecule is strongly disordered and has a low concentration.

The following results about depolymerization are exclusively based on the room temperature experiments with *CI2* and *CI3*, where no difficulties as reported above were encountered. No additional residual densities similar to those observed in the synchrotron measurements were found. However, it cannot be excluded that corresponding residuals were eliminated when applying the *Squeeze* algorithm to the 2cpy molecules, due to the close proximity of potential residuals to the 2cpy. Another possibility is that they are blurred by additional thermal vibrations and therefore not visible. *Figure 5.2a* shows

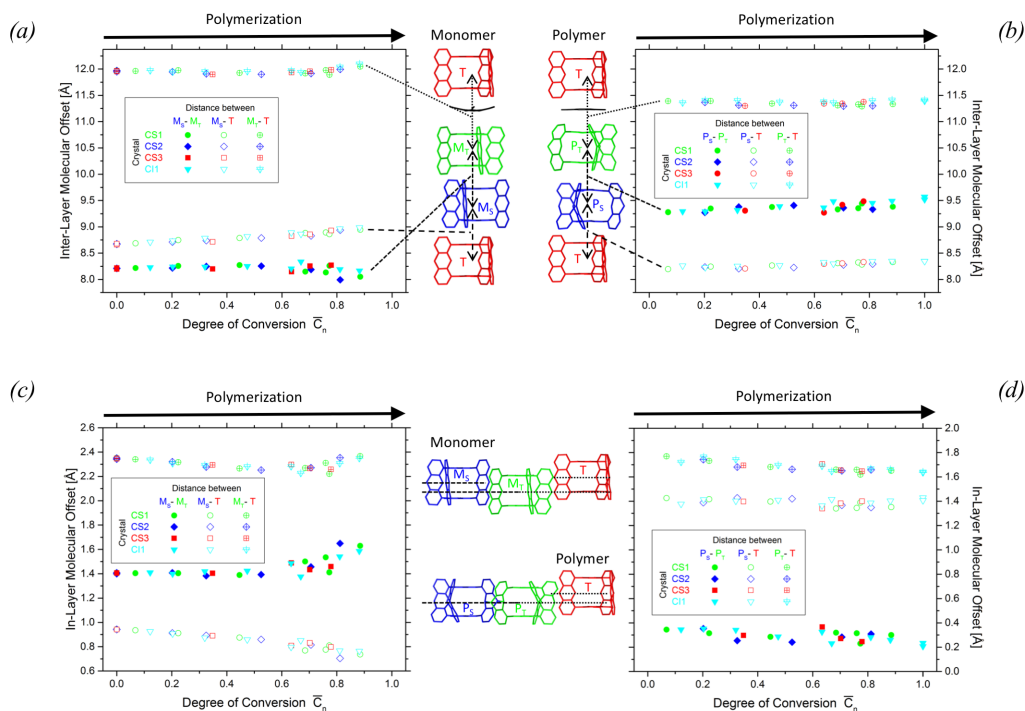


Figure 5.4: Change of the inter-molecular center-to-center distances between molecules along the columns with increasing conversion in (a) the monomer and (b) polymer portion at 100 K. Change of the inter-molecular center-to-center distances with increasing conversion within a layer in (c) the monomer and (d) polymer portion at 100 K. Note that color codes in the plots refer to the data set and not to the molecules. Modified with permission from Hofer *et al.* (2018).

the heating-time dependent conversion from polymer to monomer, which proceeds much faster than found by Kory *et al.* (2014b). While the *a*-axis shows an initial increase and subsequent decrease, *Figure 5.2b*, the *c*-axis initially shows a substantial decrease followed by a steady increase, *Figure 5.2c*. The final ADPs are smaller compared to the late phases of polymerization, but they never recover the values of the fresh crystal, *Figure 5.3*. The inter-molecular distances between P_T and the template in the column mimic the behavior of the *c*-axis: after a significant distance shortening by about 1 Å, they move continuously further apart from each other and reach approximately their original offsets, *Figure 5.5a,b*. Also apparent by the overall unit cell volume is that polymerization and depolymerization do not form a closed

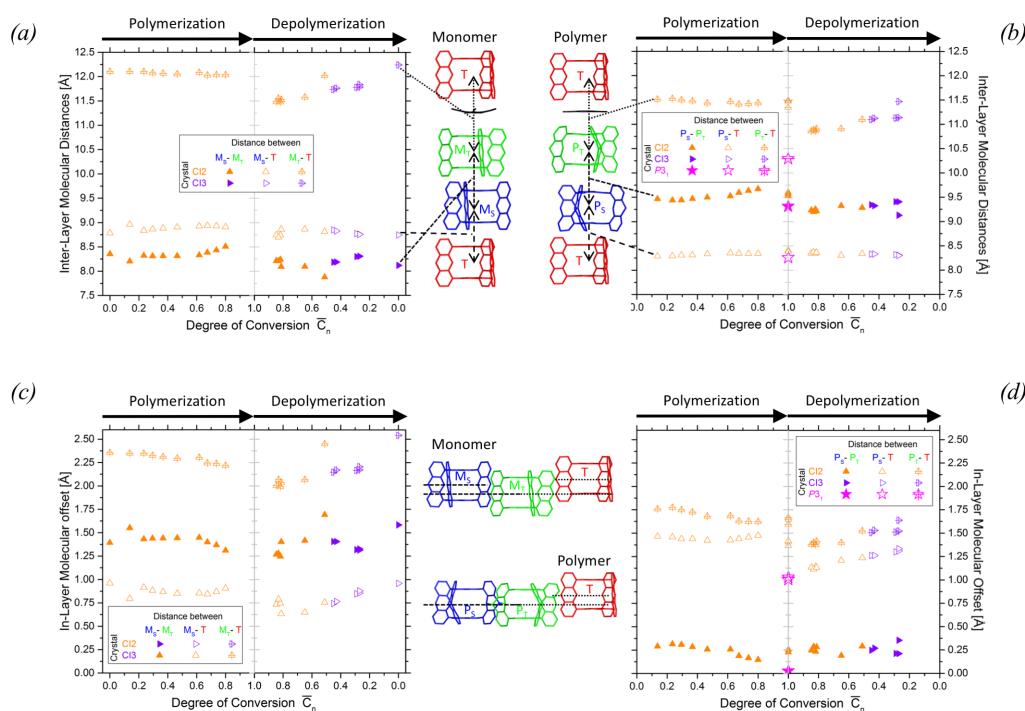


Figure 5.5: Change of the inter-molecular center-to-center distances with conversion between molecules along the columns in (a) the monomer and (b) polymer portion at room temperature. Change of the inter-molecular center-to-center distances with conversion within a layer in (c) the monomer and (d) polymer portion at room temperature. The values for the $P3_1$ structure are taken from Kory *et al.* (2014b). Modified with permission from Hofer *et al.* (2018).

loop, *Figure 5.2d*. When comparing the monitored parameters when switching from polymerization to depolymerization, the overall spread of the data points is larger during depolymerization.

5.1.3 Solvent molecules

Three different orientations of the upright 2cpy could be identified, *Figure 5.7a*, two of which were already reported by Kory *et al.* (2014b). They can be easily distinguished by the angle between the c -axis and the 2cpy's pendant cyano group. Remarkable is the short interatomic distance of 0.91 Å between the terminal nitrogen atoms of a certain sandwich-like and an up-

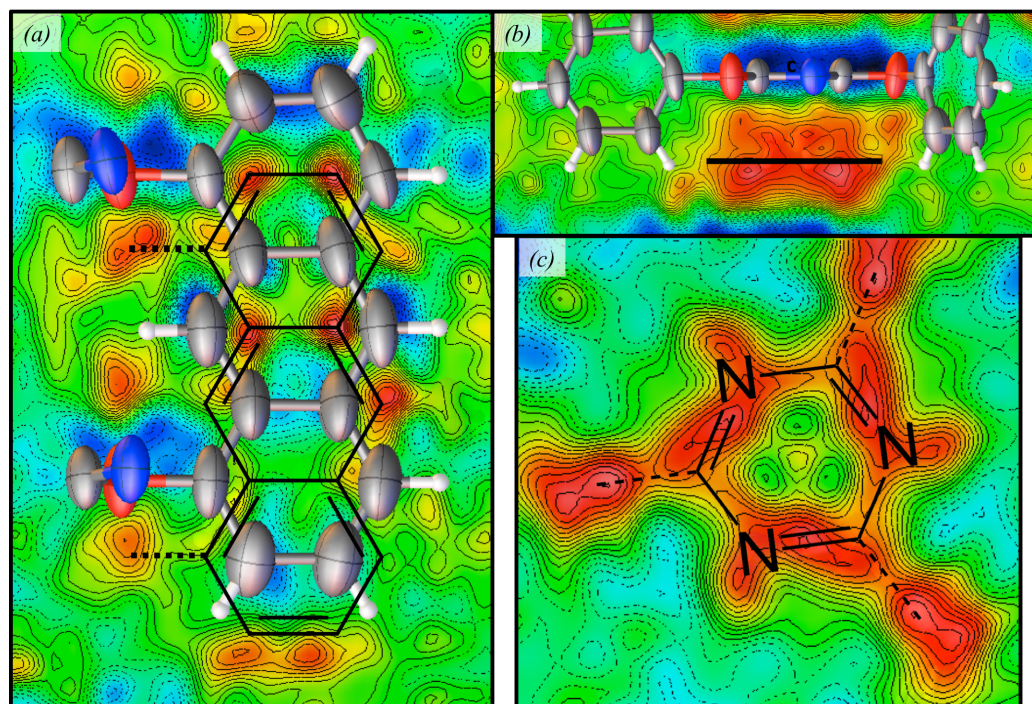


Figure 5.6: Residual electron density contour maps ranging from $+0.8 [e\text{\AA}^{-3}]$ (solid red lines) to $-0.6 [e\text{\AA}^{-3}]$ (dashed blue lines) at three different locations around M_T during the first step of depolymerization. (a) Residual electron density map centered on the anthracene blade, the maxima form the shape of an additional anthracene blade (black overlay) that is shifted against M_T (ORTEP plot) and P_T (not shown because most parts of it are outside of the drawing plane) along the c -axis. (b) Residual electron density map taken from a greater depth than (a) to highlight the distance offset of the triazine core. The black line marks the location of the electron density map shown in (c). (c) Residual electron density map focused above the triazine core. The maxima form the distinctive shape of the triazine core (black overlay). Note that negative electron densities appear at the exact location of the modeled monomer, showing that the monomer's modeled site occupation is overestimated. Reproduced with permission from Hofer *et al.* (2018).

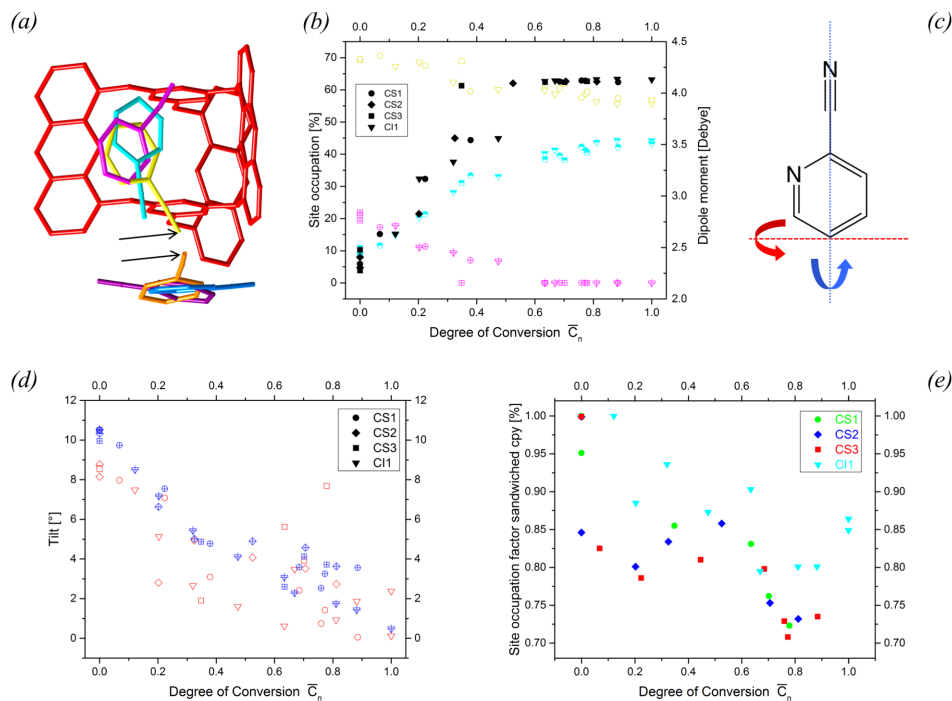


Figure 5.7: (a) Distribution of the disordered 2cpy molecules around the template. Note that the 2cpy orientations pointed out by arrows can not be present at the same time due to too short N - N distances. The sandwiched 2cyps below the template are symmetry-related via a threefold rotation axis. (b) Change in site occupation factors (left y-axis) of the upright 2cyps (half cyan symbols refer to the downward, open yellow symbols to the downward-right and crossed magenta symbols to the upward-right positions shown in (a)) and the calculated change of the dipole moment (right y-axis, solid black symbols). For comparison, a single water molecule has an electric dipole moment of 1.85 D (Clough *et al.*, 1973). (c) The 2cpy's short (dashed) and long (dotted) axis along which the molecular tilt is described. (d) Change of the 2cpy's tilt during polymerization for the short (open red symbols) and long (crossed blue symbols) axis. (e) Decreasing site occupation factors of the sandwiched 2cyps as a function of \bar{C}_n . Modified with permission from Hofer *et al.* (2018).

right 2cpy, highlighted in the *Figure 5.7a*. That particular distance is much shorter than any intra-molecular N - N distance, with the shortest being 1.10 Å (Haynes, 2014), which means that these two orientations cannot be present together. During polymerization, they reorient themselves, with one orientation even completely disappearing, *Figure 5.7b*. The polar nature of the crystal's space group and of the 2cpy give the crystal structure an overall electric dipole moment that changes upon polymerization because of the solvent's reorientation. *Figure 5.7b* (filled black symbols) depicts calculated values of that dipole moment and its changes during polymerization.

Upon polymerization, the initially tilted sandwiched 2cyps, *Figure 5.7c*, change to an almost parallel arrangement with respect to the *ab*-plane, *Figure 5.7d*. Furthermore, they get partially dislocated and once the crystals are fully polymerized, about one quarter of them have left their original site and could not be localized anymore, *Figure 5.7e*.

5.1.4 Reproducibility and systematic errors

The spread in the obtained structure parameter values and inconsistencies between repeated experiments are significantly larger than expected from statistical uncertainties. In particular, there is a striking discrepancy between the irradiation-time dependent evolution of \bar{C}_n in the in-house and the synchrotron measurements, which may be explained by the fact that the measurements were done with crystals from two different batches. Subtle environmental changes during synthesis and crystallization may have had an impact on the crystal quality and thus on the reactivity. Also, radiation damage from the intense synchrotron beam as well as variations in the environmental conditions during polymerization – the fridges for hosting the reactor at the synchrotron facility and in-house were not the same – may influence the reactivity and therefore the rate of conversion. Differing crystal volumes are not expected to play a major role because of the tail-end irradiation technique, which was selected to ensure homogeneous polymerization independent from the crystal volume (Enkelmann *et al.*, 1993). However, such an influence on the results obtained cannot be completely ruled out.

Inconsistencies in other structure parameter values within and among the various data sets may be explained by systematic errors stemming from the choices during data reduction and structure refinement strategies as discussed

above. The presence of split reflections certainly has an impact on the accurate determination of lattice constants. Furthermore, the observed strong numerical correlations between SOFs, ADPs, as well as overlapping electron densities of monomer and polymer portions could be resolved only partly. Despite these problems, consistent trends in the evolution of structure parameters could be identified. The comparison of repeated experiments helped to estimate the robustness of the results.

5.2 Real crystal structure

5.2.1 Features in reciprocal space

The observed diffuse scattering features are quite diverse and summarized in the following paragraph and shown in *Figure 5.8*. During the entire polymerization the diffuse scattering intensities increase with increasing \bar{C}_n . *Figure 5.8a,b* show the overall intensity increase of irregularly shaped diffuse scattering in the $hk0.2$ and $0kl$ sections. Thermal diffuse-scattering (TDS)-like maxima appear regardless of whether that position should be systematically extinct and vary in their intensity. *Figure 5.8c,d* show the intensifying and the appearance of additional TDS-like diffuse scattering maxima in the $hk1.8$ and $hk3.2$ sections. *Figure 5.8e,f* showcase both, the broadening and intensifying of different broader and irregular shaped diffuse scattering and the increase of the TDS-like diffuse scattering in the $hk5.6$ and $hk10.2$ sections. Finally, *Figure 5.8g,h* show the appearance of incomplete hexagons of diffuse scattering with vertices on integer h and k positions. At a \bar{C}_n of 0.44, *Figure 5.9* shows the occurrence of reflection splitting in the tangential direction.

5.2.2 *Yell* refinement results

The final R -values⁹ for the refinements with *Yell* of the monomer, 0.22 and 0.44 structures are 0.1294, 0.1397 and 0.1443 respectively. *Figure 5.10a* shows the best results for a single section in reciprocal space together with

$${}^9R_w = \left\{ \frac{\sum [w(F_o^2 - F_c^2)^2]}{\sum [w(F_o^2)^2]} \right\}^{\frac{1}{2}}$$

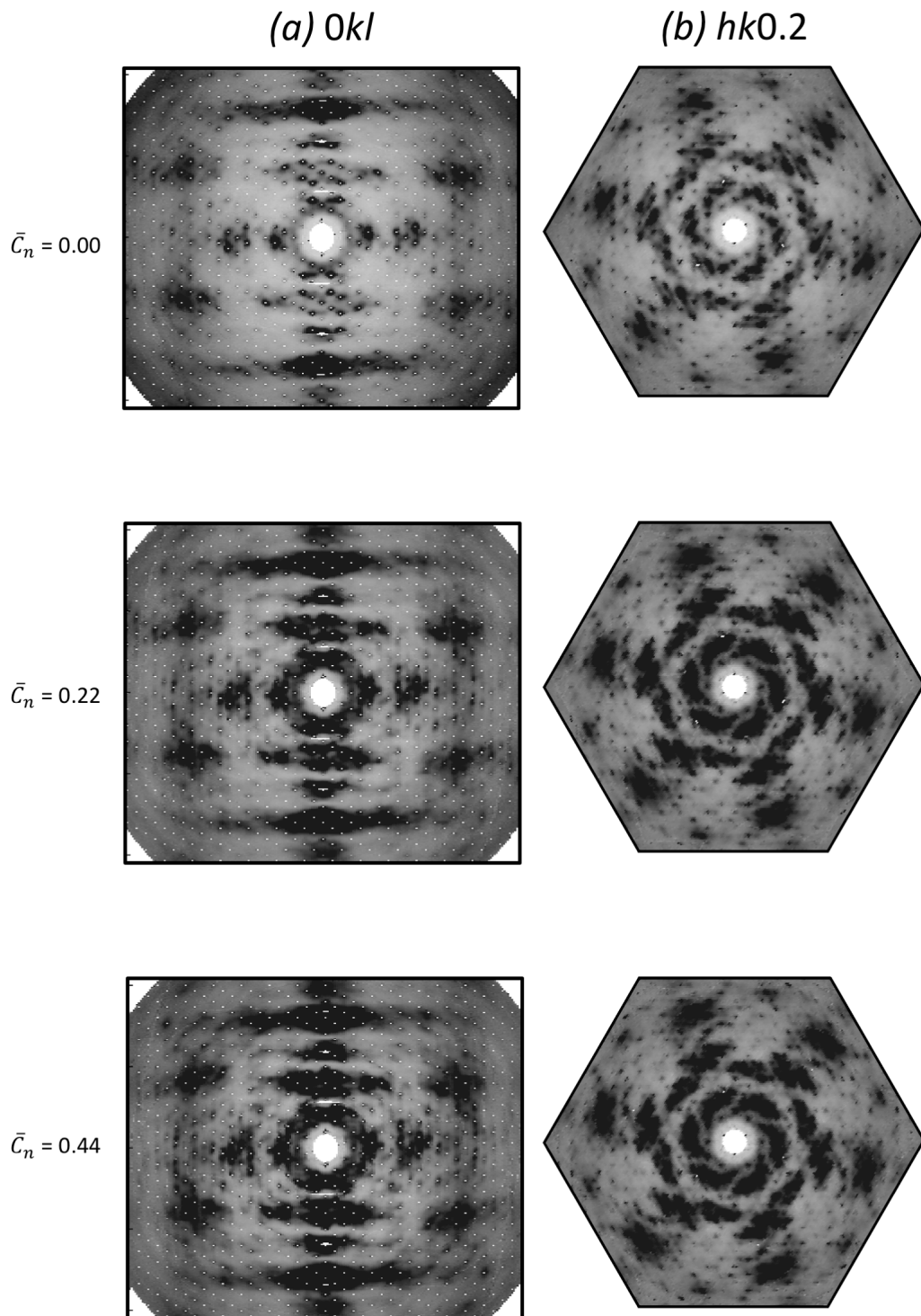


Figure 5.8: (Continued on next page)

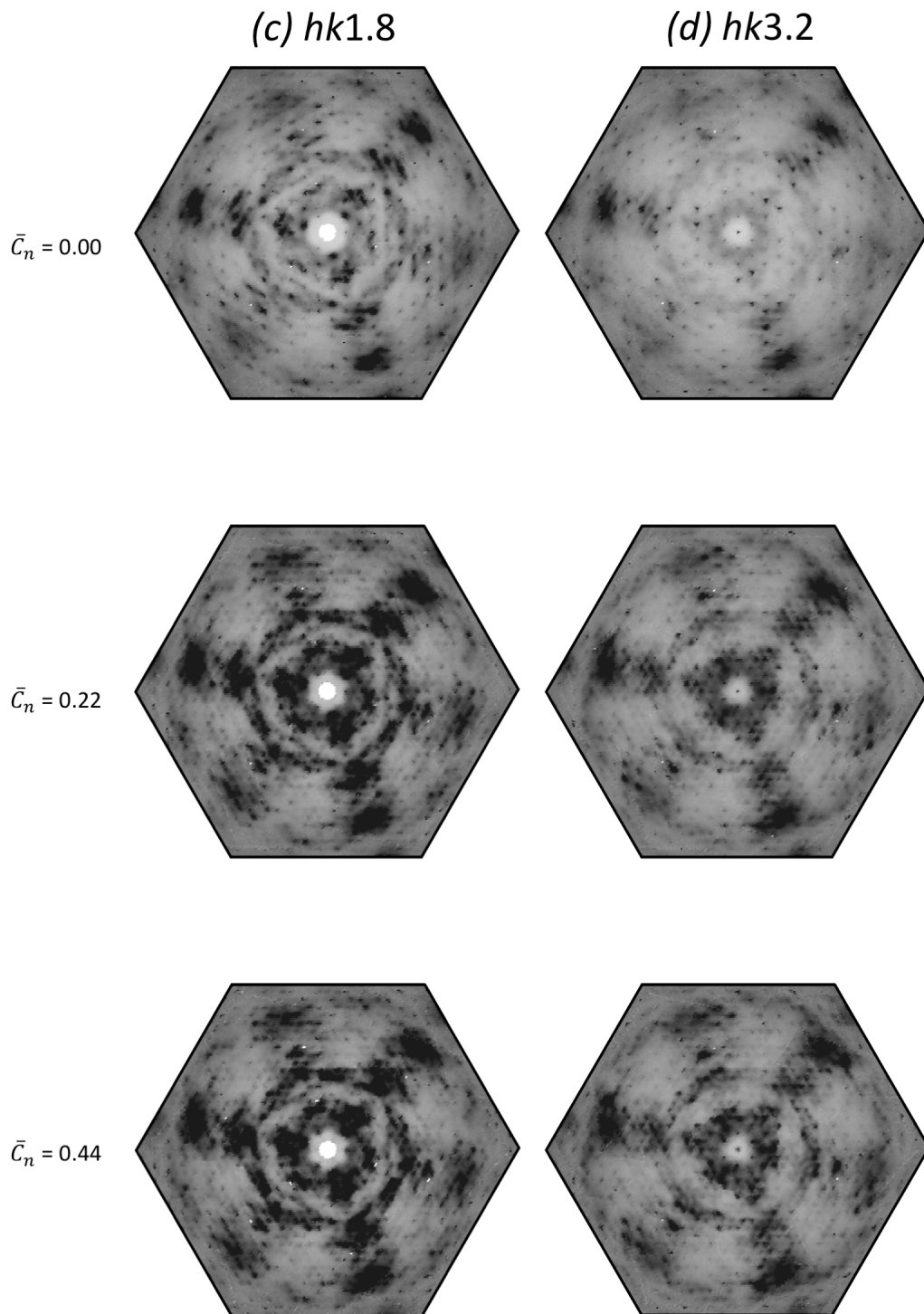


Figure 5.8: (Continued on next page)

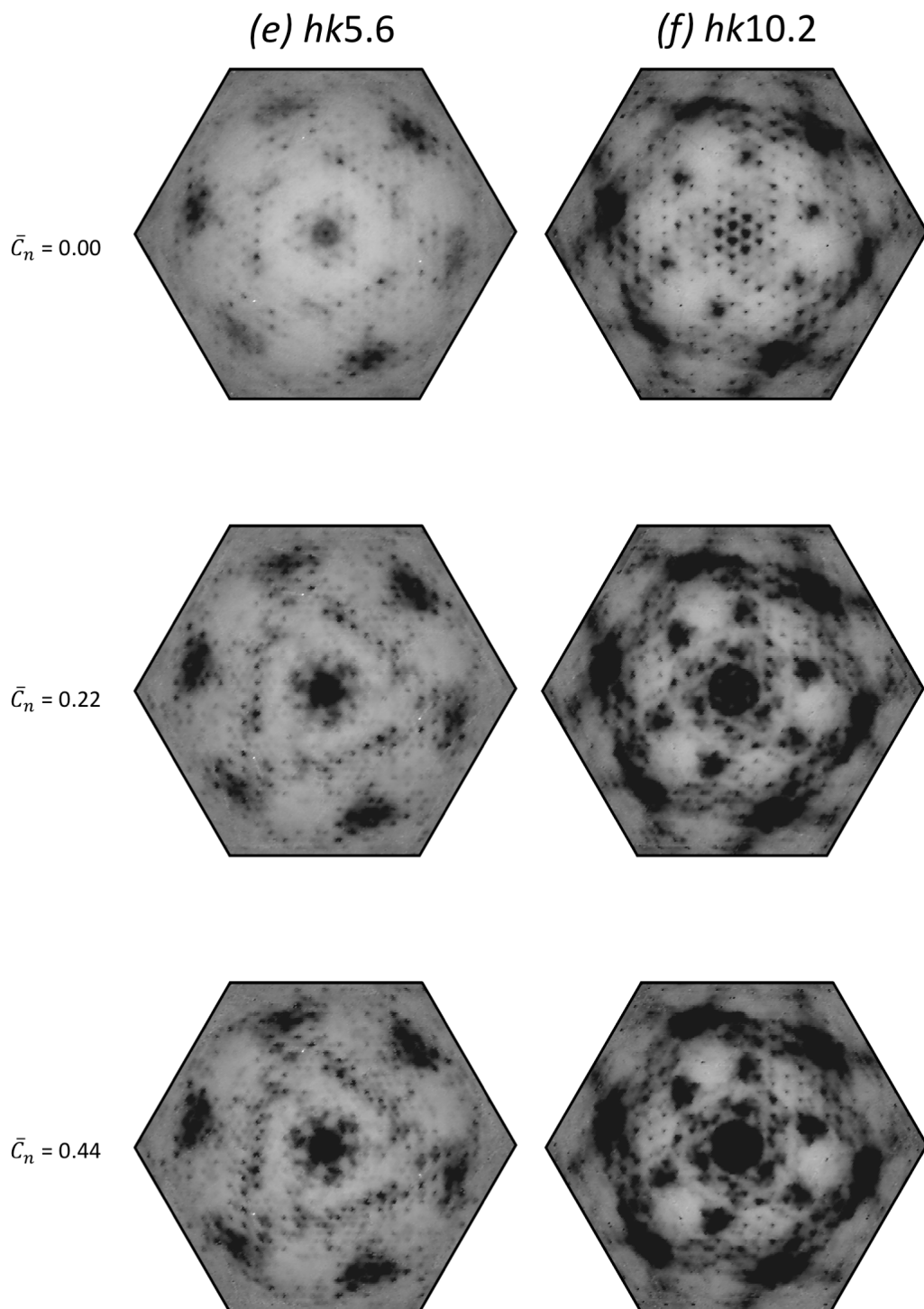


Figure 5.8: (Continued on next page)

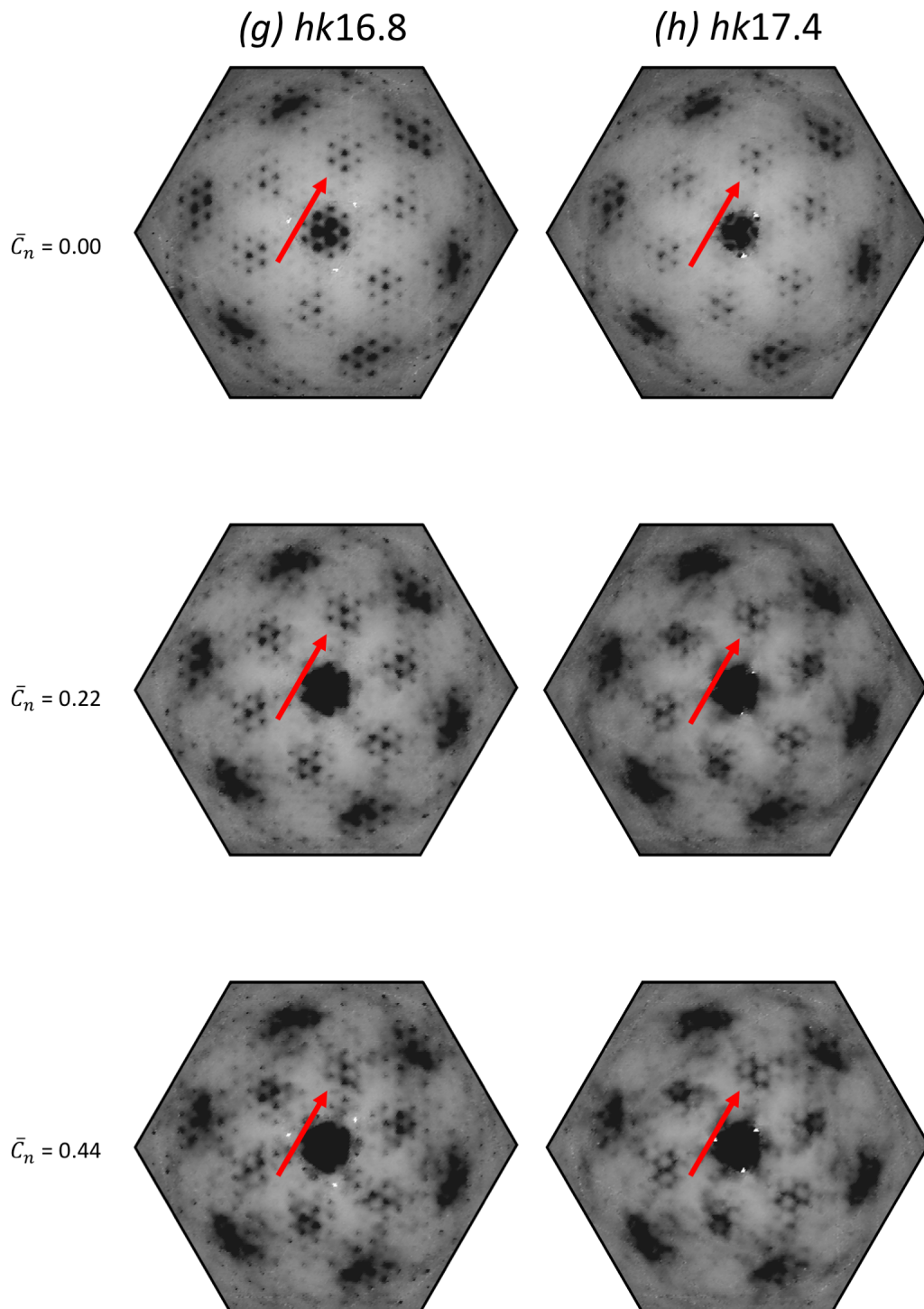


Figure 5.8: (Continued on next page)

Figure 5.8 (Previous pages): Selection of symmetry-averaged reciprocal space reconstructions of the observed diffuse scattering showing the wide range of diffuse scattering features. Broad, white areas are regions not covered by the detector. The presented sections show the development of the diffuse scattering during polymerization in the (a) $0kl$ section, (b) $hk0.2$, (c) $hk1.8$ section, (d) $hk3.2$ section, (e) $hk5.6$ section, (f) $hk10.2$ section, (g) $hk16.8$ section and (h) $hk17.4$ section. The white dot-pattern in (a) are removed pixels which contained Bragg scattering. The arrows in (g) and (h) mark the appearance of fine diffuse scattering features connecting integer h and k positions. Images have the same intensity scale.

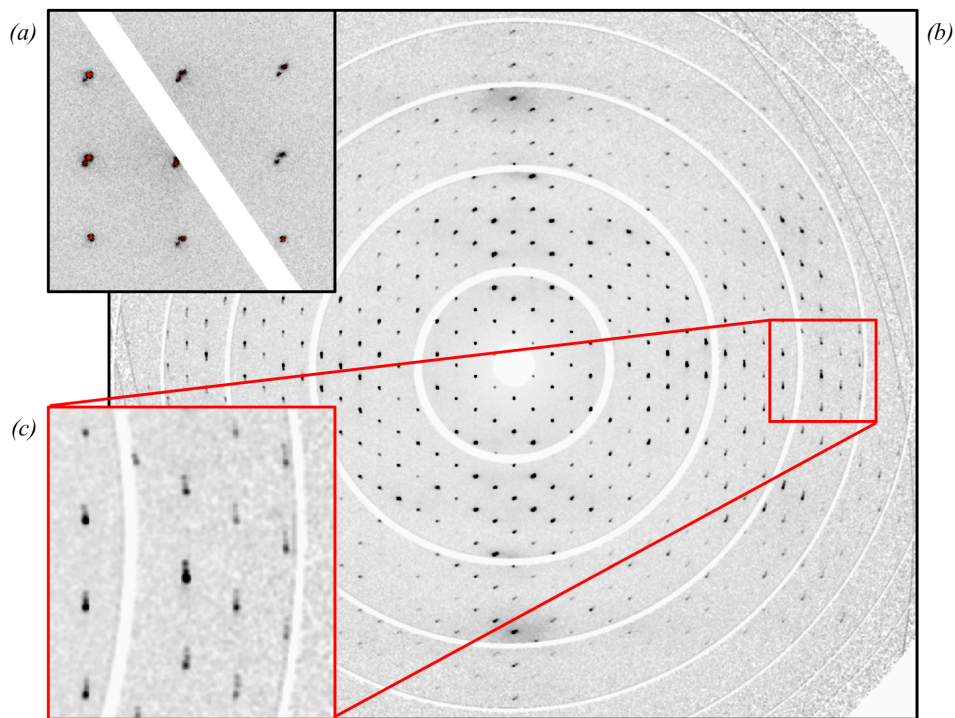


Figure 5.9: Observed reflection splitting at a \bar{C}_n of 0.44 as seen in (a) raw frames, (b) a reciprocal-space reconstruction of $0kl$ layer. (c) shows a magnification of the highlighted area in (b). White spaces represent areas that were not covered by the detector. Images have the same intensity scale.

the model of diffuse scattering and its difference at all investigated conversion ratios. *Figure 5.10b,c* show typical results of the experimental diffuse scattering and *Figure 5.10d* shows the worst result for an individual sections. Note that most of weak features in the models are sharper than in the experimental patterns, which is especially noticeable in *Figure 5.10d*, making the model data appear to be more dotted. The most likely cause is a small overestimation of several refined disorder parameters or insufficient removal of the tail-ends of Bragg reflections.

Standard uncertainties provided by *Yell* were usually in the fourth or fifth significant position. Changes in the *R*-value reported by *Yell* usually only become apparent when the numbers in the second or third significant position vary. In addition, the conversion ratio is derived from the average structure, which, as explained in *Section 4.3.2*, is already subject to a variation of single-digit percentage points, showing that uncertainties are strongly dominated by systematic errors.

In PDF space, density features are diverse, but well reproduced by the models. *Figure 5.11a* shows what is considered the best individual section in PDF space. *Figure 5.11b,c* show examples of the *uv*0.37 and *uv*0.42 section and are of typical model quality compared to the obtained data. *Figure 5.11d* shows the apparently worst fit of an individual section in the model. This is also the only section with strong systematic residual PDF densities, which are highlighted in *Figure 5.12*. These PDF densities are close to the center and present in all degrees of conversions investigated. They correspond to the intra- and interatomic distances within or between the anthracene blades, but could not be further refined due to the molecular scattering model. There is an apparent decrease in PDF densities with increasing conversion ratio because the features become wider and thereby seem to weaken the densities locally. However, the integral PDF densities increase with conversion ratio.

The contributions of the displacive and substitutional disorder could be well separated, both in reciprocal and in PDF space. An example is shown in *Figure 5.13* for a conversion ratio of 0.44. in reciprocal space, *Figure 5.13a*, the experimental data shows a ring-like structure close to the center which is present in the modeled substitutional disorder but not in the modeled displacive disorder. *Figure 5.13b* highlights an example in PDF space where a

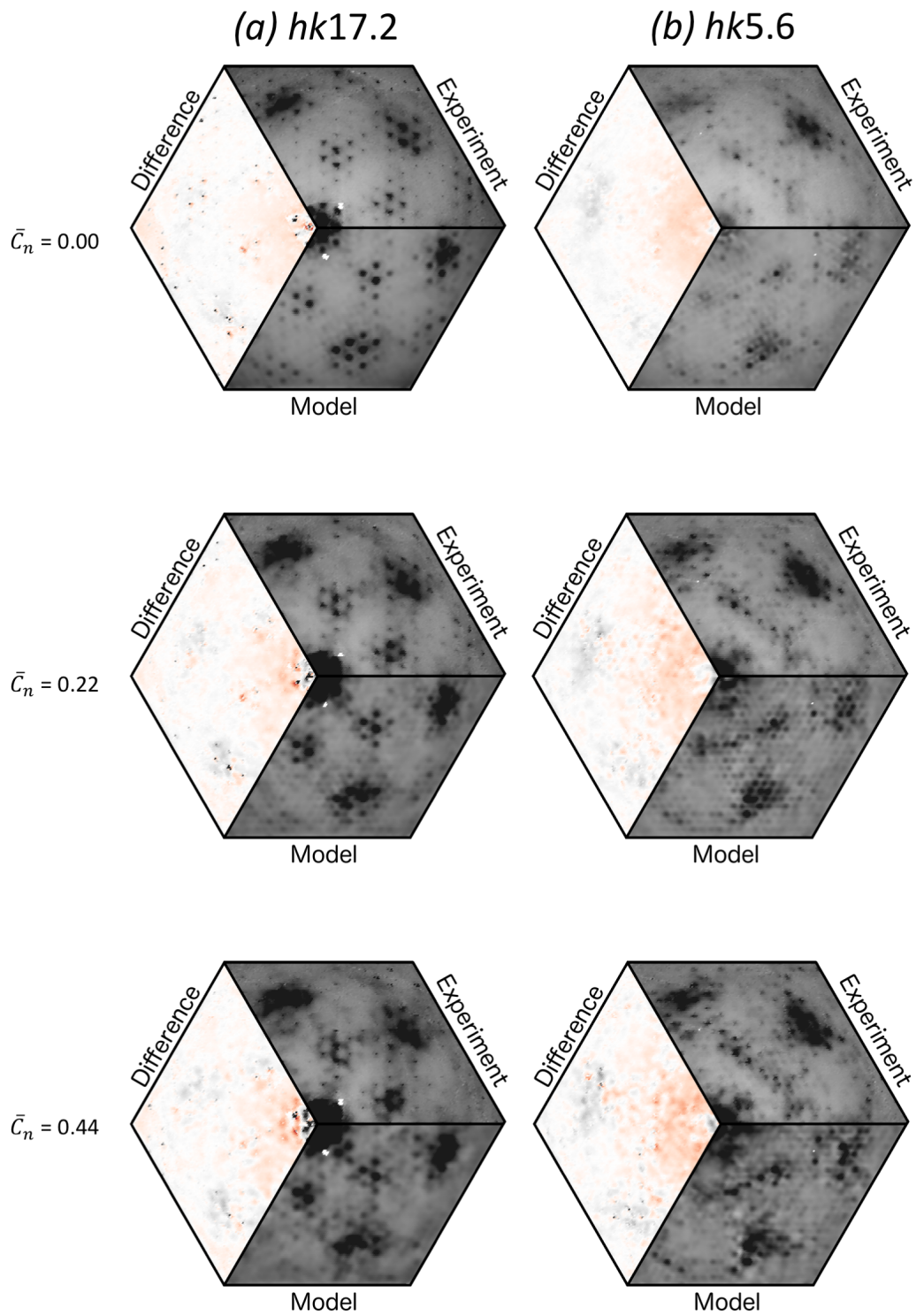


Figure 5.10: (continued on next page)

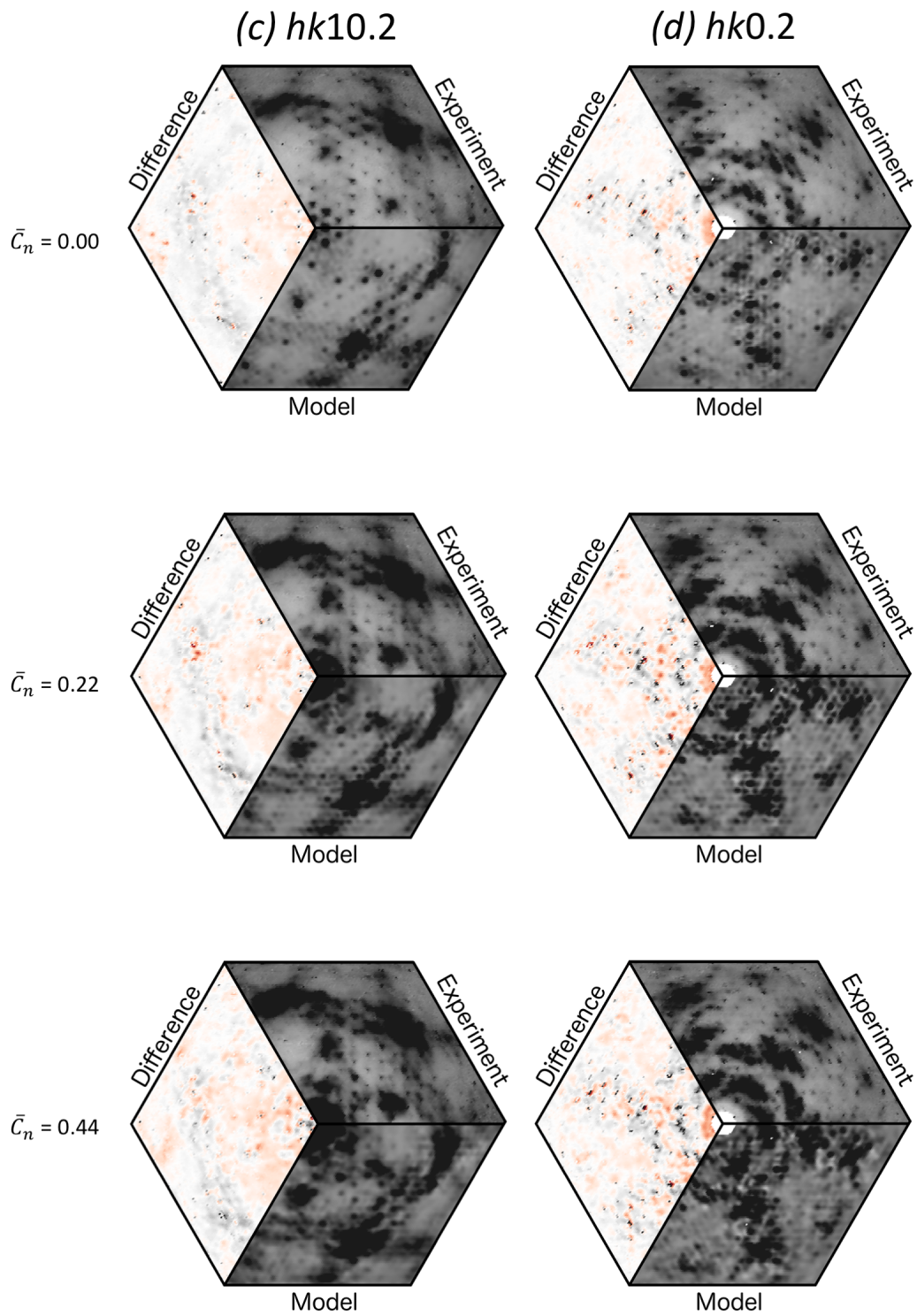


Figure 5.10: (continued on next page)

Figure 5.10 (Previous pages): Selected comparisons of the experimental and modeled diffuse scattering for all investigated degrees of conversion. (a) shows the best fit of an individual section. (b) and (c) show different regions in reciprocal space and are considered of typical quality. (d) shows the worst fit of an individual section.

cluster of negative and positive densities in the experimental data are modeled by a cluster of negative densities from the substitutional disorder overlapping a cluster of positive densities from the displacive disorder.

5.2.3 Displacive disorder

Displacive disorder is modeled as covariances and is transformed to correlations as

$$cor_{ij}^{AB} = \frac{U_{ij}^{AB}}{\sqrt{U_{ii}^A U_{jj}^B}} \quad (5.1)$$

with cor_{ij}^{AB} being elements in the correlation matrix describing the interactions between the moieties A and B . Correlations can assume values in the range from -1 to $+1$, where $cor_{ij}^{AB} = 0$ indicates the absence of a concerted displacement while positive and negative correlations indicate in-phase and anti-phase displacements, respectively. An example for a positively correlated displacement would be a joint translation of two objects. Generally speaking, the covariance between two moieties is used to identify strong diffuse scattering features because covariances are dependent on the displacement's amplitude. However, once sites with significant covariances were found, their development throughout polymerization is best followed via correlations because correlations are normalized with respect to the moiety's average displacements.

The diffuse scattering caused by displacive disorder is the most prominent and dominant feature throughout all polymerization steps. This is evident by the fact that the majority of features in reciprocal space are already present in the monomer structure, as seen in *Figure 5.8*. Understanding this kind of

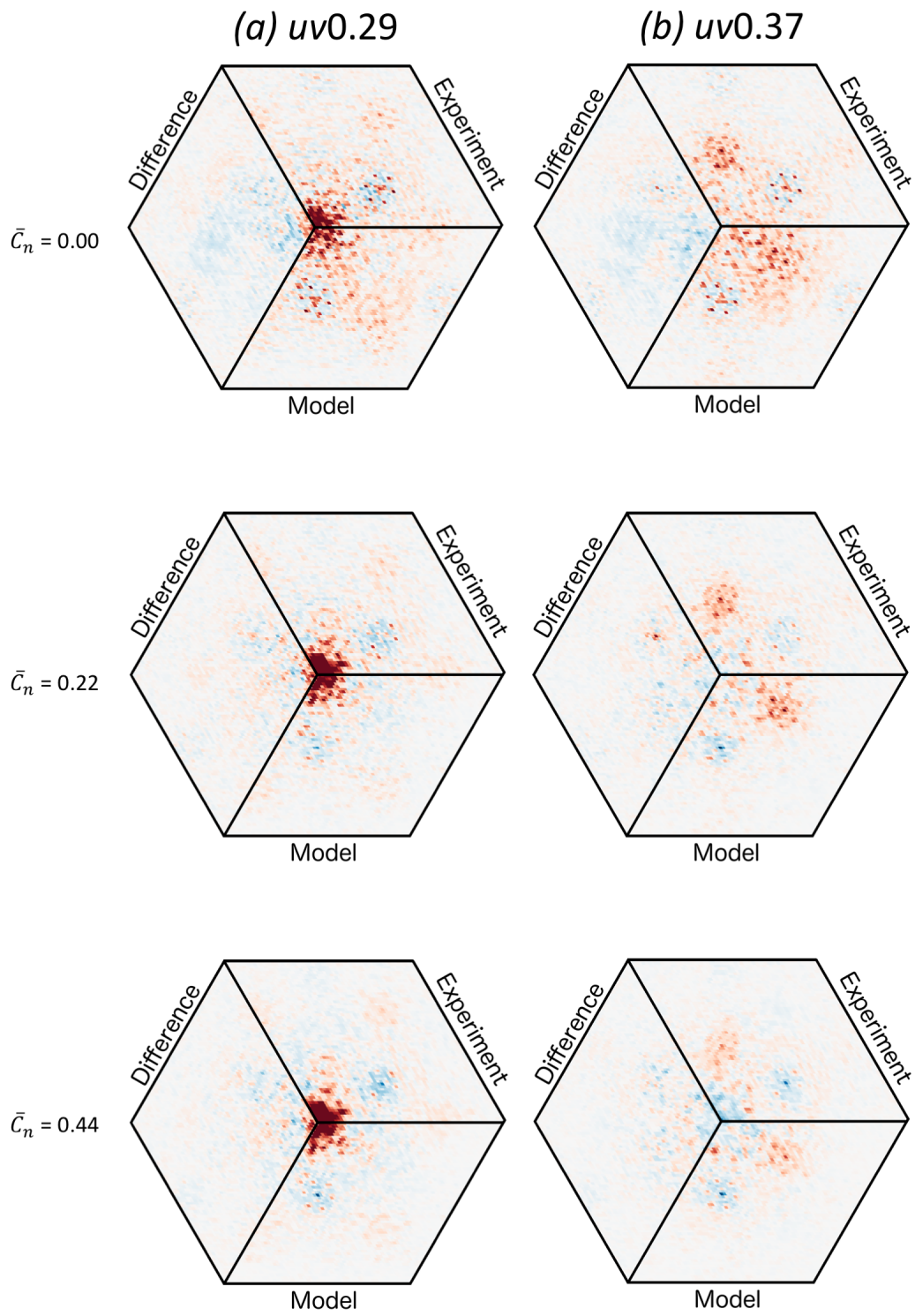


Figure 5.11: (continued on next page)

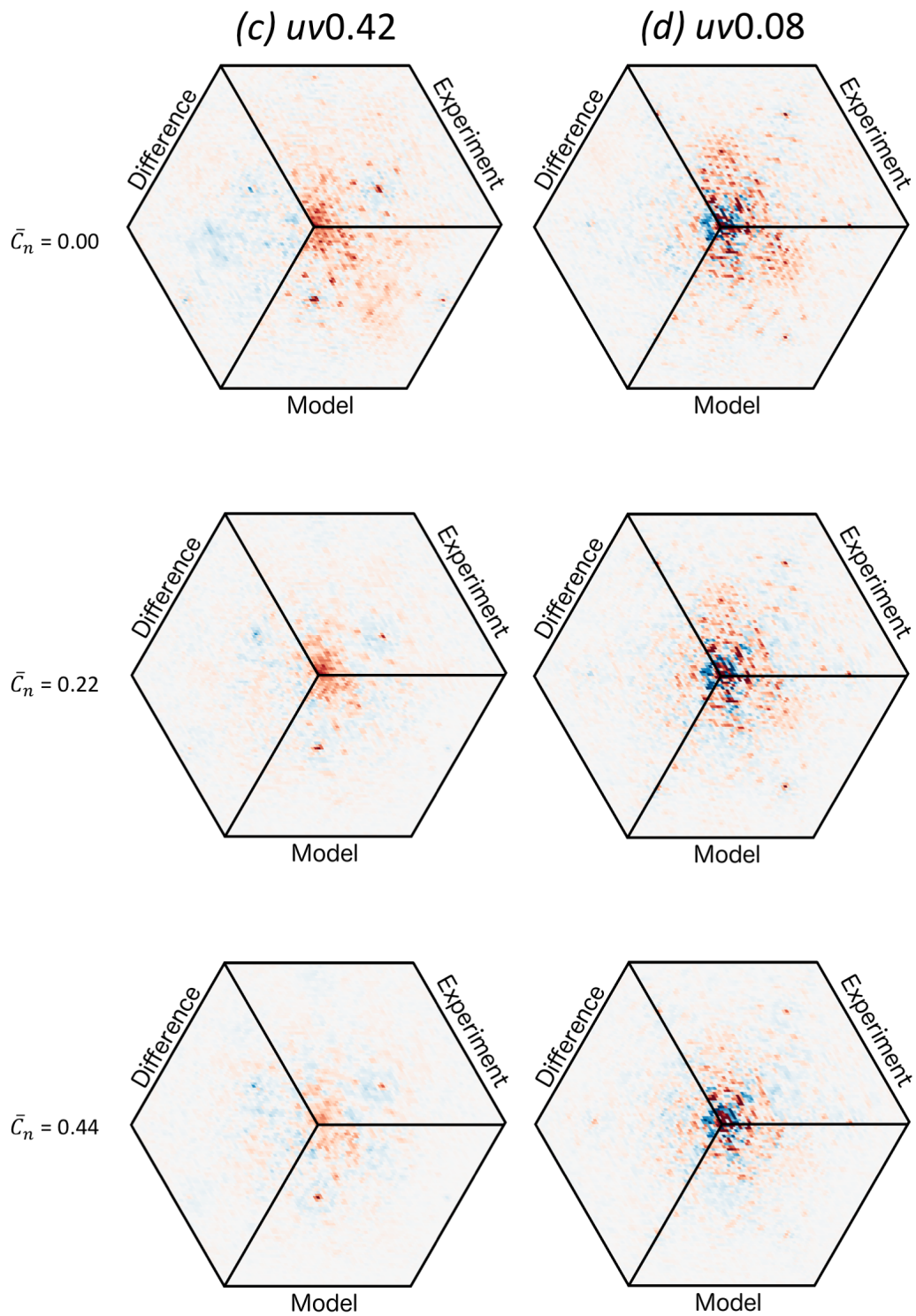


Figure 5.11: (continued on next page)

Figure 5.11 (Previous pages): Selected comparisons of the experimental, modeled, and their difference 3D- Δ PDF maps for all investigated conversion ratios. (a) shows the best fit of individual section. (b) and (c) show different regions in PDF-space which are considered of typical quality. (d) shows the worst fit of individual section.

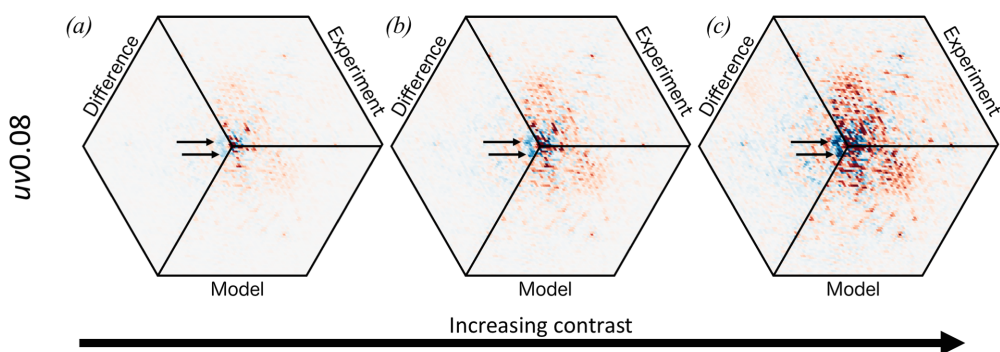


Figure 5.12: 3D- Δ PDF maps of the $uv0.08$ -layer, comparing the experimental data with the model data at increasing contrast settings. The blue triangles close to the origin and highlighted by arrows are unassigned densities and the only residuals resulting from model simplifications for all evaluated data-sets.

disorder was therefore essential. U^{AB} matrices for any given translation, libration or stretching mode can be calculated, which would yield a fingerprint for each mode. In practice, such calculations were of limited use, because libration and stretching modes strongly depend on their relative rotation or stretching axis in relation to the molecular moieties. Furthermore, the incomplete understanding of the off-diagonal U^{AB} elements, as discussed in *Section 4.4.5*, might lead to over- or wrong interpretations. However, as detailed later in this chapter, the most significant U^{AB} matrices have negligible off-diagonal values, typically by a factor ten or more smaller than the diagonal elements. Small off-diagonal values could mean two things, either that they are actually small or that the matrix itself becomes skew-symmetric. In the first case, displacements would be most likely simple translations, because all considered librations and stretching modes have either significant contributions from the off-diagonal elements or negative main-diagonal values. In the second case, the off-diagonal contributions from the U^{AB} matrix would

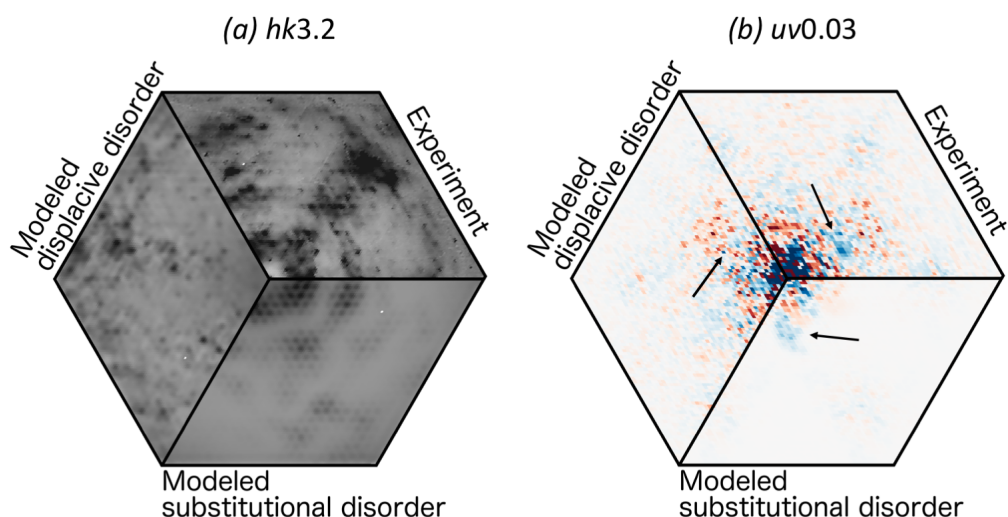


Figure 5.13: (a) reciprocal space reconstruction of the $hk3.2$ section together with modeled substitutional disorder and displacive disorder showing their differing occurrences in reciprocal space. (b) $uv0.03$ section in $3D-\Delta PDF$ space together with modeled substitutional disorder and displacive disorder. Arrows highlight areas where modeled densities of displacive and substitutional disorder contribute at different locations to the overall densities.

have canceled each other out according to *Equation 4.4*. In the absence of further evidence, the former was assumed.

Given the number of parameters obtained for the displacive disorder, about 2 000 for the monomer and about 4 000 for each partially polymerized structure, and the limited knowledge about the U^{AB} matrix, overall trends were sought and investigated. The first and most striking trend is that the vast majority of displacements are positively correlated. Also, correlations decrease with increasing distance, as expected. Furthermore, covariances, but not necessarily correlations, increase with an increasing \bar{C}_n , meaning that displacement amplitudes increase without an increase of a coordinated displacement. The strongest covariances are found in the first neighborhood around each molecule. In the second neighborhood, the covariances are al-

ready about two to five times weaker. The weakening of the covariances is more pronounced within the layer than in the column.

Table 5.3 summarizes all displacive correlations along the major axes within the individual molecules, their polymerized counterparts and the two directly face-to-face stacked blades. Note that they are all positive throughout polymerization, with the exception of one correlation which is of insignificant negative magnitude. The largest covariance and strongest correlation between two blades during conversion are the intramolecular correlations within M_S and M_T in the monomer substructure. The strongest correlations between two half-dimers are found between the two face-to-face stacked half-dimers from P_S and P_T as well as within P_S and P_T themselves. Together, they represent both, the strongest covariances and correlations in the polymer substructure and the strongest correlations throughout the whole polymerization. The displacive correlations within the partially polymerized molecules, in *Table 5.3* denoted as MP_S and MP_T , also become quite strong over the course of polymerization.

There are also surprisingly large covariances and correlations developing between blades and half-dimers within the columns upon polymerization. Their correlations are depicted in *Table 5.4* with the U_{33}^{AB} component as the most significant one. The values given refer to blades and half-dimers directly above and below each other and are representative of the interactions of the entire monomer molecules and their polymerized counterparts. Of remarkable interest is the occurrence of negative correlations in three cases. First, the correlations between the blades from M_S and M_T of the second neighborhood turn from positive to negative upon conversion to 0.44. Second, the initially negative correlations between half-dimers in the first and second neighborhood become positive at an increasing conversion. Finally, the correlations between P_T and the template change from negative to weakly positive upon polymerization. The strongest correlations, positive and negative, are found between two half-dimers, although at different conversions. Within the columns, certain trends of correlated displacements parallel to the ab plane were found. The correlations between the blades belonging to M_T/P_T and the template separated by the solvent are weaker than between the blades in direct contact with each other. This trend is observed throughout the polymerization process. All first-neighbor correlations are given in the appendix in *Tables 10.1, 10.2*.

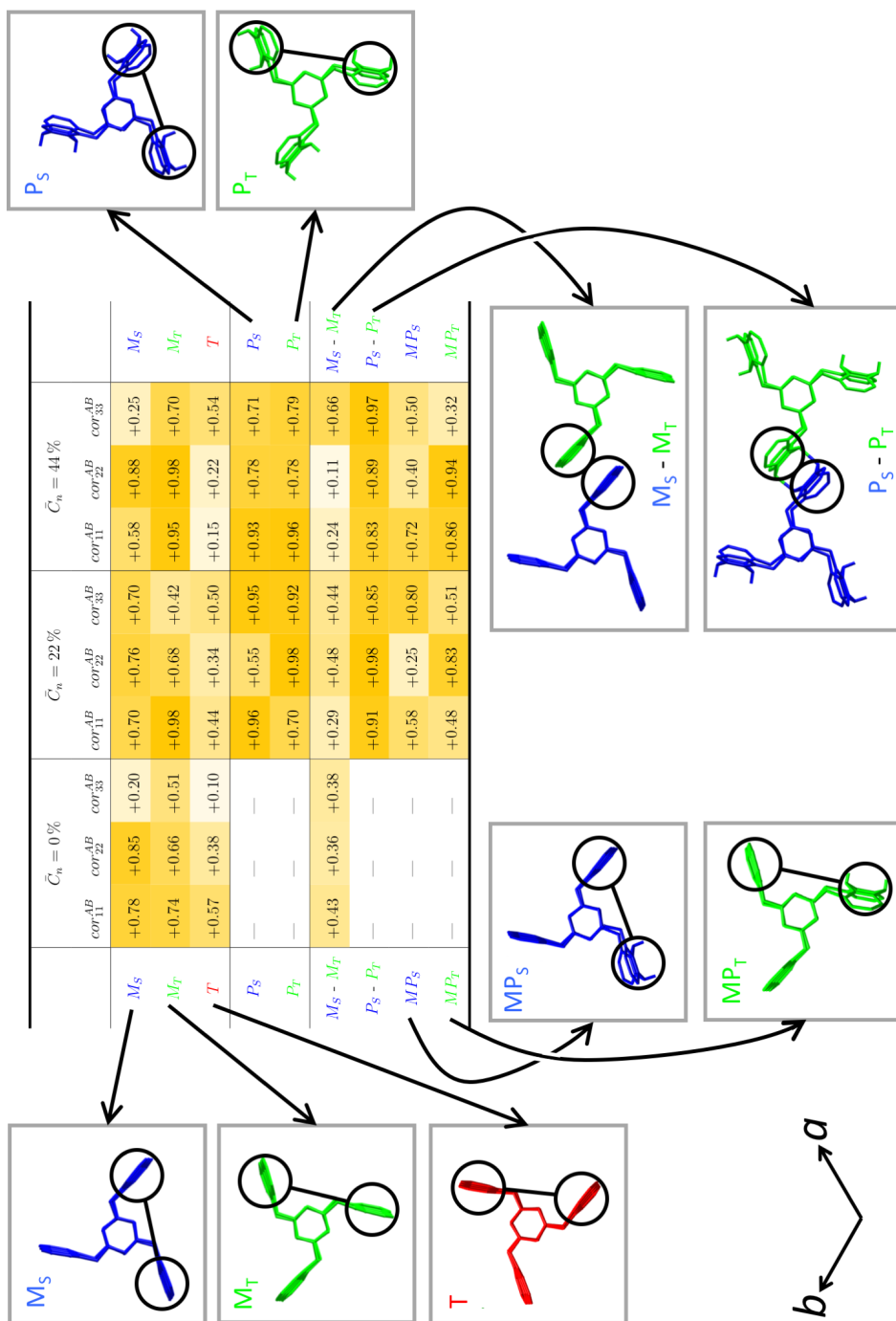


Table 5.3: Intra- and selected intermolecular correlations between blades and half-dimers. cor_{11}^{AB} , cor_{22}^{AB} and cor_{33}^{AB} denote the correlated movement between two moieties along the major axes. Note that all of them are positive with the color shading indicating the strength. The magnitudes of all cor_{ij}^{AB} components are all significantly smaller than 0.05, 0.18 and 0.14 for all three investigated conversions and are therefore negligible. Statistical errors are in the fourth significant digit and not shown.

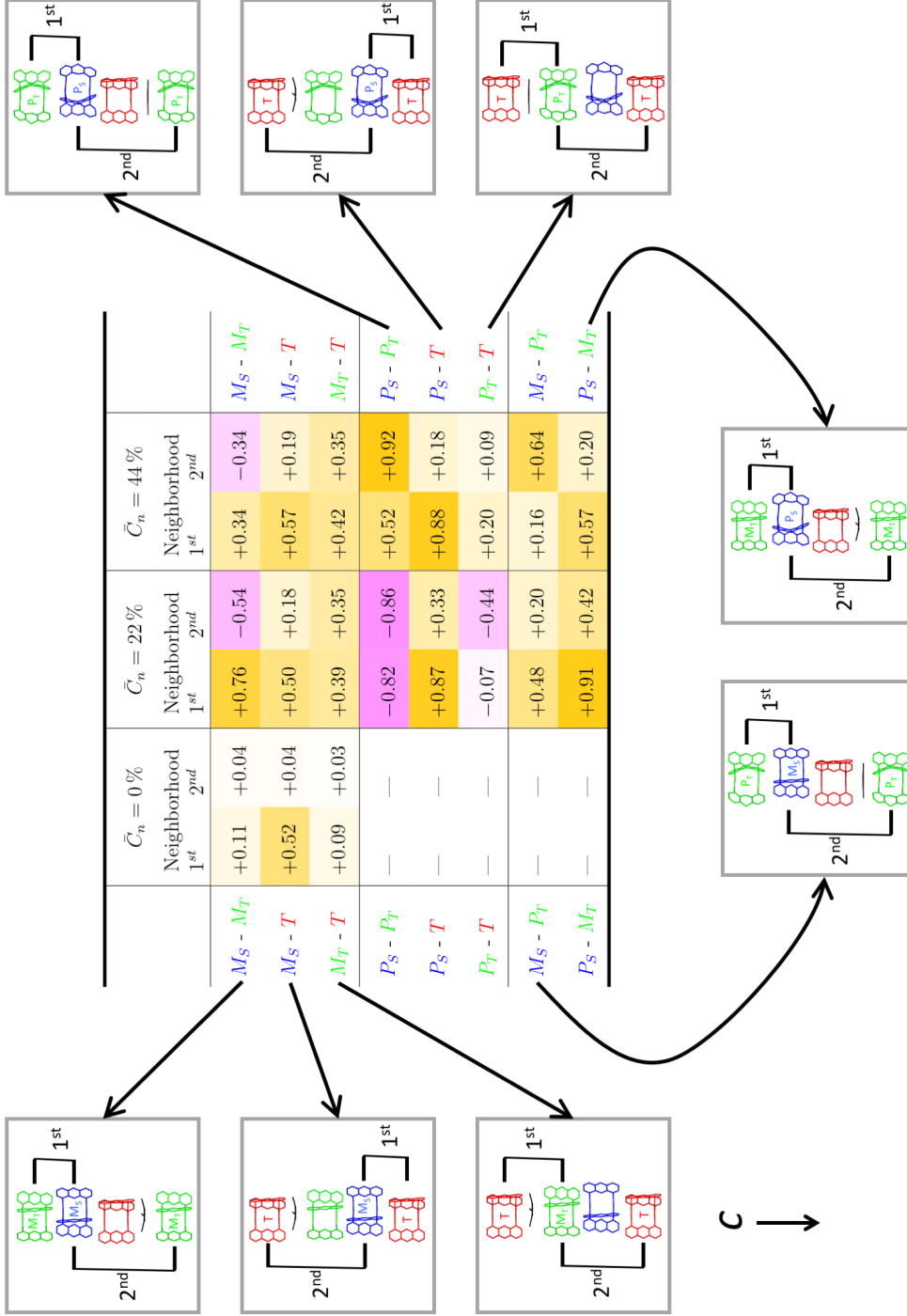


Table 5.4: cor_{33}^{AB} of blades and half-dimers stacked in the column. Negative correlations are highlighted in purple and positive correlations in yellow, while shading indicates magnitude. Statistical errors are in the fourth significant digit and not shown. Further details are given in the text.

Covariances and correlations comparable to the ones shown in *Table 5.4* are also found between the template and the moieties surrounding it, *Table 5.5*. In the monomer substructure, the strongest covariances and correlations are found between the edge-to-face stacked template and M_S . Additionally, covariance and correlations between the polymer and the template increase. The cor_{11}^{AB} component between M_T and the template, which is along the face-to-face contact between the individual blades, is dominant throughout polymerization.

Between previously not discussed pairs, certain trends of displacements between molecules and moieties are observed. Predominantly, positive correlations along the main axes with a magnitude smaller than 0.30 are found although negative correlations and correlations with an cor_{12}^{AB} , cor_{13}^{AB} and cor_{23}^{AB} component of similar magnitudes are also encountered. These displacements are consistent throughout polymerization, *i.e.* no major qualitative changes of the correlations were observed.

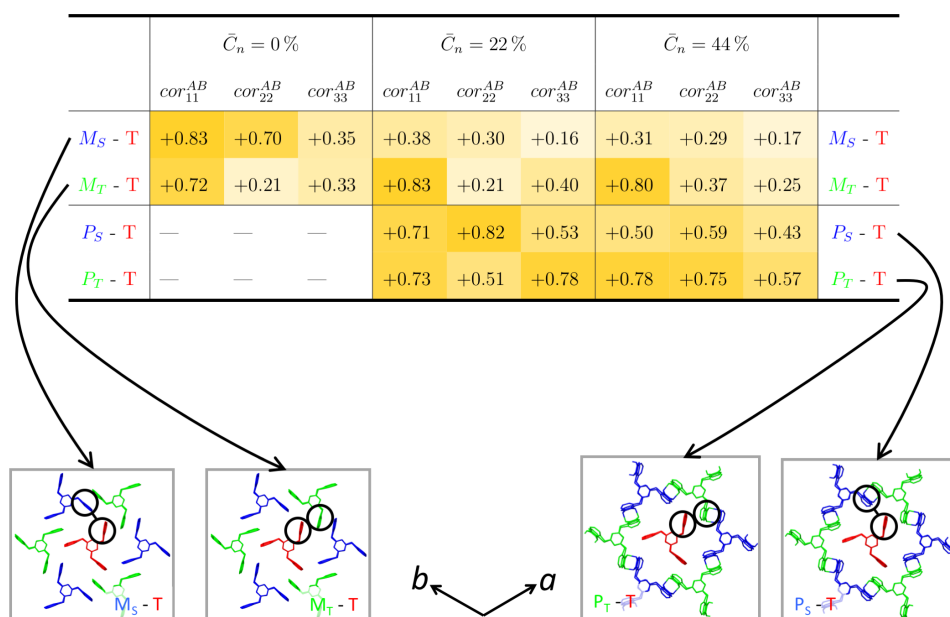


Table 5.5: Correlations between the template and its neighboring in-layer blades and half-dimers. Shading indicates magnitude. Statistical errors are in the fourth significant digit and not shown.

All correlations of the first neighborhood, which are the strongest observed correlations after the intra-molecular correlations, are tabulated in *Section 10*.

5.2.4 Substitutional disorder

Substitutional disorder occurs only between blades and dimers and are therefore only present in the partially polymerized structures. The joint probabilities modeled and refined by *Yell*, as discussed in *Section 4.4.6*, are transformed into correlations by the formula

$$C_{DD} = \frac{p_{DD} - \bar{C}_n^2}{\bar{C}_n - \bar{C}_n^2} \quad (5.2)$$

where C_{DD} is the the change in correlation between two dimers with respect to a random distribution, analogous to the work on substitutional disorder by Welberry (1985). C_{DD} can vary between -1 and $+1$. If C_{DD} is larger than zero, then it is more likely than random chance to find an anthracene dimer at a given location. If C_{DD} is smaller than zero then it is less likely to find an anthracene dimer at a given location with respect to a random distribution. For the previously established basic reactivity models, *Section 2.3.2*, these correlations are shown in *Figure 5.14*.

At a conversion of 0.22, *Figure 5.15a* shows that all in-layer correlations to the central dimer are weakly negative, with the strongest correlations of -0.10 in the first neighborhood and part of the third neighborhood. Notably, neighbors with the same topological but different geometrical distance have different correlations. While in the second neighborhood, that difference is rather small with 3 percentage points, the difference between the geometrically closest third neighbor and the remaining third neighbors is with 10 percentage points more substantial. *Figure 5.15b* shows the out-of-layer correlations. The first neighbors are slightly negative. The second neighborhood is divided by geometric distances, where the closest neighbors are uncorrelated, and distant ones are positively correlated. The overall appearance of correlations is of dimers isolating themselves, where the in-layer isolation reaches over longer geometric distances than out-of-layer.

Upon polymerizing to a \bar{C}_n of 0.44, these correlations change. Within the layer, *Figure 5.15c* shows that the first neighbors and closest second neighbors

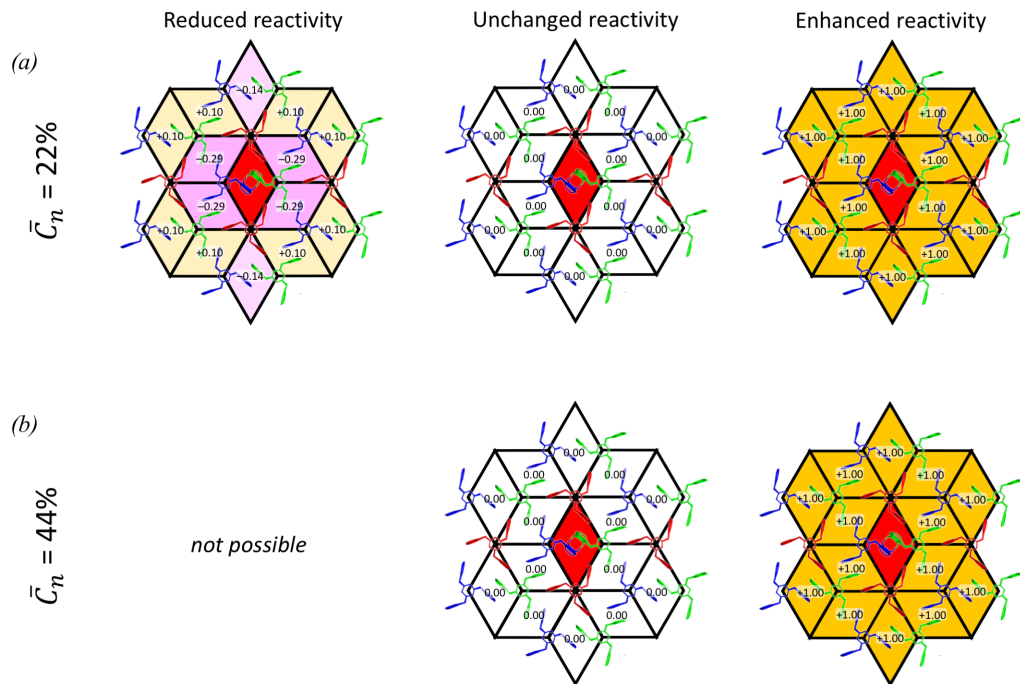


Figure 5.14: Expected patterns for substitutional correlations obtained from MC simulations for the three basic reactivity models defined in *Section 2.3.2* at a \bar{C}_n of (a) 0.22 and (b) 0.44. All models show the probability to find two dimers (the first being the central red rhomb) separated by a given distance from each other within the structure. Note that the definition of the basic reactivity models do not allow the reduced reactivity model to grow beyond a \bar{C}_n of 0.33. Yellow rhombs refer to positive correlations and violet rhombs to negative correlations, while shading indicates the strength of the correlation.

are still negatively correlated, though shifted closer to randomness. The more distant second neighbors and closest third neighbors have become positively correlated. *Figure 5.15d* shows that out-of-layer, the first neighbors and the second neighbors of intermediate geometric distance have not changed significantly. However, the correlations with the geometric nearest second neighbors and closest third neighbor have decreased, the former becoming negatively correlated and the latter almost uncorrelated.

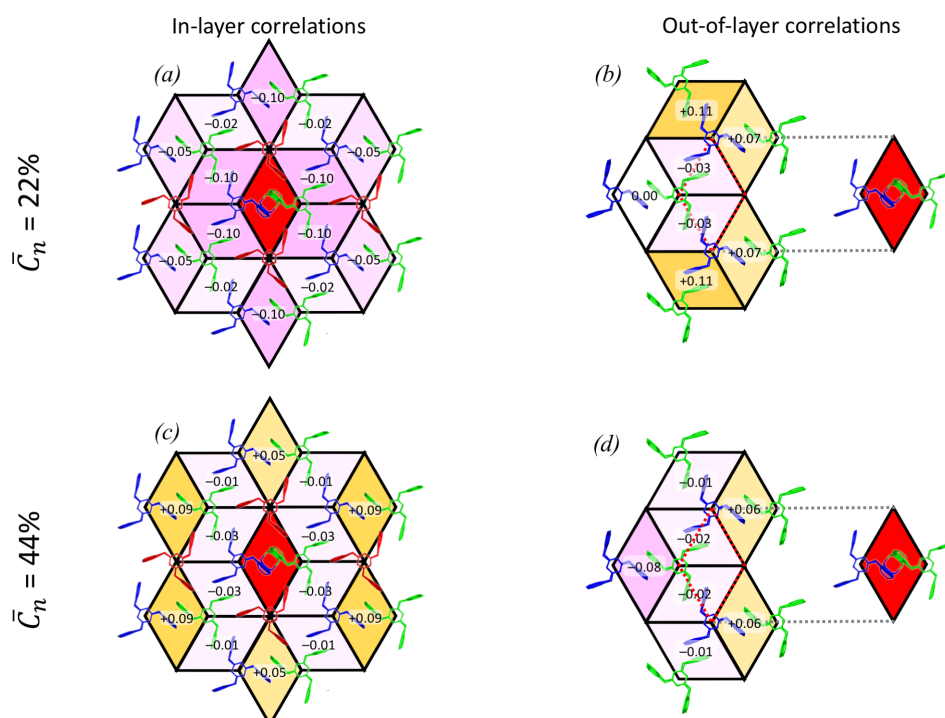


Figure 5.15: Substitutional correlations as refined by Yell for (a) in-layer and (b) out-of-layer at a \bar{C}_n of 0.22 and for (c) in-layer and (d) out-of-layer at a \bar{C}_n of 0.44. In (b) and (d), the isolated rhomb indicates that dimerization occurred in the layer below and dotted lines show the structural relation of that dimer with respect to the layer. See *Figure 4.5b, d* for additional information on the structural layout. The color code is similar to *Figure 5.14*.

6 2D polymerization and depolymerization

6.1 Insights from Bragg scattering

6.1.1 Structure transformation mechanics

The following chapter provides a detailed analysis of how the average structure reacts to the formation and breaking of anthracene - anthracene bonds during polymerization and depolymerization. The data primarily refer to the low temperature synchrotron data when discussing polymerization and to the room temperature in-house data when regarding depolymerization. Information about the 2cpys is exclusively taken from the low temperature measurements, because these molecules could not be sufficiently localized at room temperature. As far as comparable, low and room temperature results are consistent with each other.

The key for understanding the structural transformation from the monomer to the polymer is the observation that neighboring P_S and P_T *reduce* their in-layer offset along c by about 1 Å relative to their monomer counterparts when they are forming covalent bonds (cf. filled symbols in *Figure 5.4c* and *Figure 5.4d*). However, within a column, the same motion *separates* the corresponding molecules by about the same amount (*Figure 5.4a, b*, filled symbols) with the consequence of a gap opening between P_S and P_T as illustrated in *Figure 6.1a, b*. The shifts are locally buffered within a column by the next neighboring template/sandwiched 2cpy pair: the average in-column distances between the template and its neighboring polymer moieties P_S and P_T are reduced by about 0.5 Å compared to the template – monomer distances (cf. open and crossed symbols in *Figure 5.4a, Figure 5.4b*).

As long as the degree of conversion is low, at most one of the monomers is expected to have formed a bond above or below a particular template/2cpy pair. Affected templates are therefore pushed from one side only instead of two. With increasing degree of conversion it becomes more likely that a template/2cpy pair feels the pressure from upper *and* lower polymers, *Figure 6.1b*. This effect is visible in the evolution of the template's ADPs, *Figure 5.3*. Initially, the atomic U_{33} increase, because the templates compensate the push from one side by moving upwards or downwards. After having reached a degree of conversion of about 0.70, the atomic U_{33} decrease again

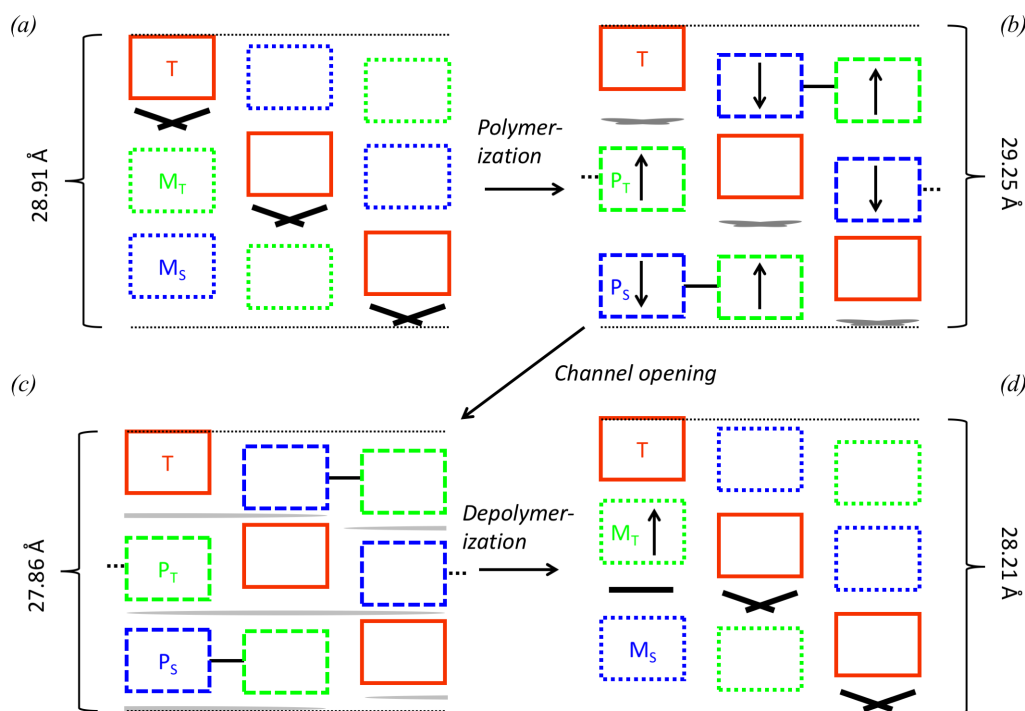


Figure 6.1: Sketches of (110) planes at different polymerization and equilibration states. The c -axis is vertical pointing downwards. Dimensions are not to scale. Monomer molecules are represented by dotted rectangles, their polymerized counterparts by dashed rectangles and the template by solid rectangles. Distances indicated by brackets refer to the unit cell height. (a) The fresh monomer structure. The crossed black lines indicate the orientationally disordered sandwiched solvent. (b) The non-equilibrated polymer structure. The bonds between P_S and P_T are shown by the connecting black bars. The arrows indicate the molecular shifts relative to the monomer due to polymerization. The solvents are slightly delocalized and their tilt relative to ab -plane has decreased. (c) Channel opening at high degrees of polymerization as described in the text. The solvent is strongly delocalized and the unit cell is smaller compared to the non-equilibrated polymer. (d) Explanation for the residual electron densities in the monomer substructure occurring at early stages of depolymerization (see *Figure 5.6*). If a solvent is locally trapped between M_S and M_T (horizontal black line) and the space between M_T and the template within the same column is not filled by a solvent, then M_T may shift closer to the neighboring template as indicated by the arrow. Modified with permission from Hofer *et al.* (2018).

since the pressure from both sides starts stabilizing the template's position. Note that the trend changes when, on average, two out of three anthracene blades per molecule have reacted, *i.e.* after the 2D network formation may have started. With increasing pressure from above and below the sandwiched 2cpys take up a flatter orientation (*Figure 5.7*, *Figure 6.1b* gray lines) and get physically squeezed away from their original sites, probably towards heavily delocalized positions that cannot be spotted in the average structure (*Figure 5.7e*). The high mobility of the 2cpys is also seen in the room temperature data where their blurred electron densities are visible in the difference Fourier maps, but the positions are too delocalized to allow a refinement.

Similar arguments as for the evolution of the pressure on the template/2cpys hold for the development of the gap opening. It is unlikely that in the early stages of polymerization two monomers neighbored along the c -axis would have reacted at the same time and therefore initial gaps open only by about 0.5 Å. With progressing polymerization gap opening continues and finally all of them reach their full size of 1 Å.

The almost perfect local compensation of the strong molecular shifts along the c -direction allows relatively small changes in the c -axis length. However, in the final step of polymerization, and, much more pronounced, after the first step of depolymerization this is no longer true. As long as a major fraction of the sandwiched 2cpys are still at their original positions, they act as spacers between the polymer layers and keep them apart. Given the flatness of the completely polymerized layers and the fully developed gaps between the polymer layers, it is assumed that pathways open at the interface between the layers. They would allow a higher lateral mobility of the 2cpys away from their original, energetically unfavorable position between the template and P_T towards sites providing more space in the polymerized state. As a consequence, the large distance between the template and P_T as well as the gap between P_S and P_T can be reduced (see *Figure 5.5a, b*, crossed and filled symbols close to the fully polymerized state) and therefore the length of the c -axis shrinks. The explanation why this effect is much more pronounced after the first step of depolymerization may be found in the fact that the higher temperature during depolymerization provides the activation energy for shifting the 2cyp molecules. The 2cpys must be highly disordered, because no significant traces of the formerly sandwiched 2cpys in the difference Fourier maps were found. Since about 60% of the 2cpys

reappear during depolymerization, it can be excluded that the 2cpy molecules have left the crystal completely.

It was described by Kory *et al.* (2014b) that temperature equilibration of the polymer has a significant impact on its structure. Annealing at 60 °C was reported to introduce a phase transition accompanied by a symmetry reduction from $R3$ to $P3_1$. In the annealed structure, *Figure 6.1c*, they were not able to identify any of the sandwiched 2cpy molecules but after depolymerization, the 2cpys take up their original position. The site occupation factor of the 2cpys in the depolymerized structure was not refined by Kory *et al.* (2014b), but constraint to full occupation. Although no dedicated annealing experiments were performed in this, traces of the $P3_1$ structure were observed in the diffraction patterns. A close inspection of highly overexposed synchrotron data shows the presence of weak, but pretty narrow diffuse maxima at positions indicating local violation of the R -centering, *i.e.* locally the $P3_1$ structure seems to be also present in all crystals, *Figure 6.2*. Such maxima become only visible after depolymerization has started and disappear after the first steps of this process. It is not completely clear why the long-range ordered $P3_1$ structure was not observed, but the most likely reason is that the stability temperature of the $P3_1$ structure was overshoot when reaching the depolymerization temperature. The most striking observation when comparing the in-column distances of the $P3_1$ structure with the results found in this study (*Figure 5.5b*, magenta stars) is that the distance between P_T and the template (crossed symbols) is much smaller in the $P3_1$ structure. This is a strong indication that a major fraction of the 2cpys have left their original sites and occupy unknown, but obviously highly disordered, positions. The distance reduction is not a simple temperature effect because the $P3_1$ structure was measured at 100 K while the data considered here were collected at room temperature: compared to distance along c of P_T and the template, the distances P_S - template and P_S - P_T are much more similar (full and open symbols).

When depolymerization is continued, the crystal volume and the c -axis increase – as it is expected when covalent bonds break. After complete depolymerization, about 60 % of the sandwiched 2cpys return to their original position. No traces of the remaining 40 % 2cpys were found and it remains uncertain whether they remain at highly disordered positions or if they have left the crystal. The return of the 2cpy during depolymerization is also seen

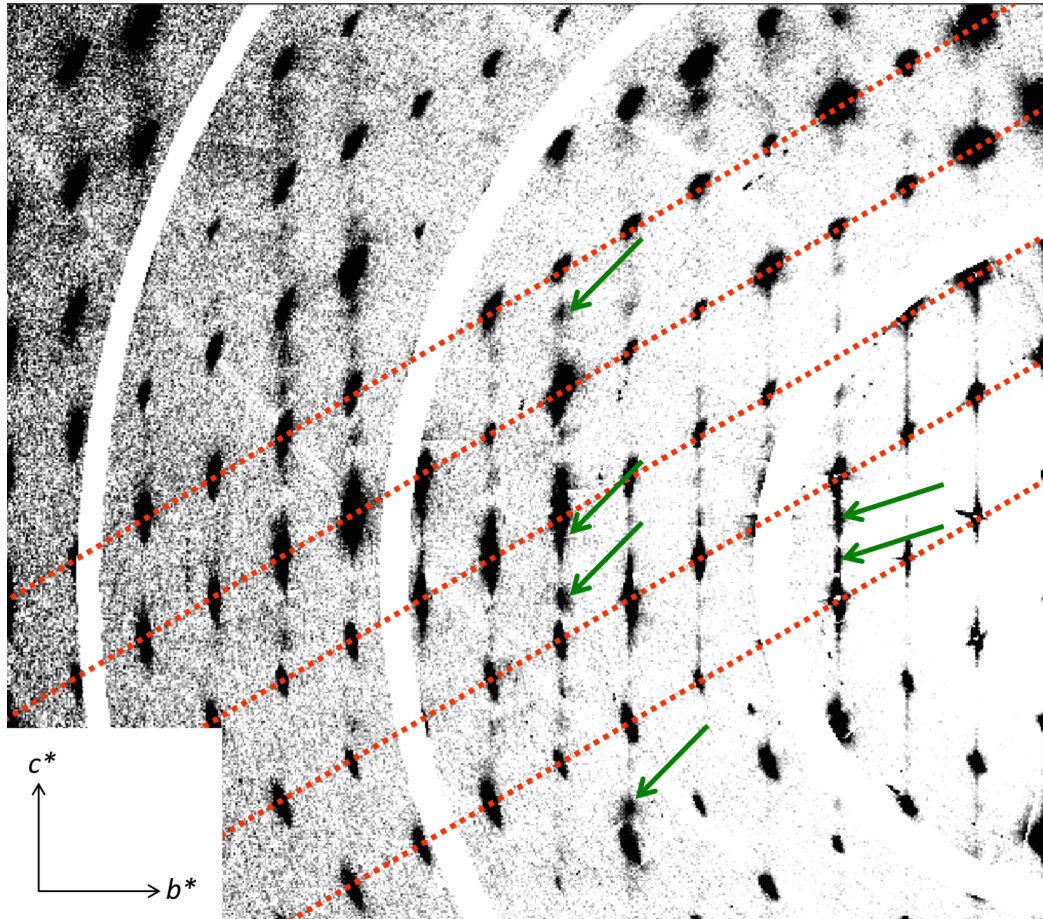


Figure 6.2: Overexposed reciprocal space reconstruction of the $0kl$ layer after the first step of depolymerization. Bragg reflections on the dotted lines highlight reflections that satisfy the cell's R -centering reflection condition. Arrows highlight examples of diffuse scattering maxima at systematic extinct lattice positions and indicate short-range ordered domains of the $P3_1$ structure. In this representation, the Bragg reflections are heavily saturated and appear to be broader than in reality because of their diffuse halo.

in the increase of the template — P_T and template — M_T distances (*Figure 5.5a, b*, crossed symbols).

The a -axis slightly reduces in size, because the monomers move back to out-of-layer positions and allow a lateral shrinkage, *i.e.* in contrast to the c -axis the depolymerization behaviour of a -axis is inverse to its development during polymerization. The observation that the a -axis increases again after the last depolymerization step is not understood so far.

The delocalization of the 2cpys close to the fully polymerized state also allows to explain the residual electron densities observed during depolymerization as shown in *Figure 5.6*. It is assumed that initially not all of the delocalized 2cpys find their way back to their positions between the template and M_T , (*Figure 6.1d*), because open pathways get blocked during depolymerization. Such stranded molecules may get trapped in remaining open gaps between P_S and P_T , which therefore cannot be closed by the later formed monomers. If, at the same time, a sandwiched 2cpy is missing at the other side of M_T , then it may shift towards the template, leading to residual electron density patterns at the in *Figure 5.6* observed position. Since the residuals cannot be fitted in the least-squares refinement, it is very likely that this scenario happens rarely and that the affected M_T molecules are heavily disordered. These residuals appear as soon as depolymerization starts and disappear in the mid-stages of our depolymerization experiments, *i.e.* such effects heal during depolymerization.

6.1.2 Propagation from reaction kinetics

For investigating the propagation mechanism from the average structure alone, polymerization kinetics were analyzed by employing the *Avrami model*. For that purpose, *Equation 2.1* is put into context for two-dimensional polymerization as

$$\bar{C}_n(t) = 1 - e^{-\omega t^n} \quad (6.1)$$

where the transformation propagation Y during two-dimensional polymerization is expressed by \bar{C}_n . The Avrami exponent n is expected to be $n = 1$ for random growth, *i.e.* if the formation of a local bond has no impact on

the reaction probability of the surrounding anthracene pairs (unchanged reactivity model, *Figure 2.2a*), it is supposed to be $n = 2$ if the polymerization starts at one seed from which a disc-like two-dimensional polymer would develop, because anthracene - anthracene bonds could only be established in the direct environment of an already existing bond (enhanced reactivity model, *Figure 2.2c*). A combined model in which additional nuclei would be formed during a disc-like growth would lead to an Avrami exponent of $n = 3$. Finally, a combined model that also stimulates three-dimensional growth would lead to $n = 4$. The Avrami exponent can be derived from the exposure time evolution of \bar{C}_n as the slope of a double logarithmic plot of $\ln t$ versus $\ln(\ln(1 - \bar{C}_n)^{-1})$ as described by Pethrick (2007). An example of such a plot of the data is depicted in *Figure 6.3a*. The Avrami exponent averaged over all polymerization kinetics data is 0.69(4) with no obvious differences between in-house, synchrotron, low or room temperature measurements and therefore very well reproducible. This is a surprising result since the original Avrami model only covers exponents $n \geq 1$ (Hay, 1971; Gedde, 1995), but examples with $n < 1$ are known (Lotz and Kovacs, 1969).

MC simulations were employed to better understand the results of the *Avrami* model. They were based on the assumption that light intensity and transparency of the crystal do not change with increasing polymerization time and that local anthracene - anthracene bond formation only influences the bond formation probability of the next lateral neighbors. The model was strictly two-dimensional, *i.e.* a single sheet and not a stack of sheets was modeled, template and 2cpys were ignored and formed bonds were assumed to be stable. The reactivity modifier r_1 was introduced to model the propagation mechanism with $0 \leq r_1 \leq 1$. The reaction probability of a blade pair having at least one dimer in the direct neighborhood is given by r_1 . Similarly, the reaction probability of a blade pair without any formed dimers in the direct neighborhood is given by $1 - r_1$. Different models were tested by varying r_1 . Enhanced reactivity models (*Figure 2.2b*) are represented by $r_1 > 0.5$, $r_1 = 0.5$ is the unchanged reactivity model (*Figure 2.2a*), and $r_1 < 0.5$ are reduced reactivity models (*Figure 2.2c*). Please note that in the case of $r_1 = 1$, an initial seed is required for starting polymerization. *Figure 6.3b* depicts the kinetic fingerprints of the simulated models as expected for $r_1 = 0, 0.5, 1$. Note that $r_1 = 0$ does not allow formation of a fully polymerized structure, but saturates at $\bar{C}_n \approx 0.3$, since any molecule can at most form one bond

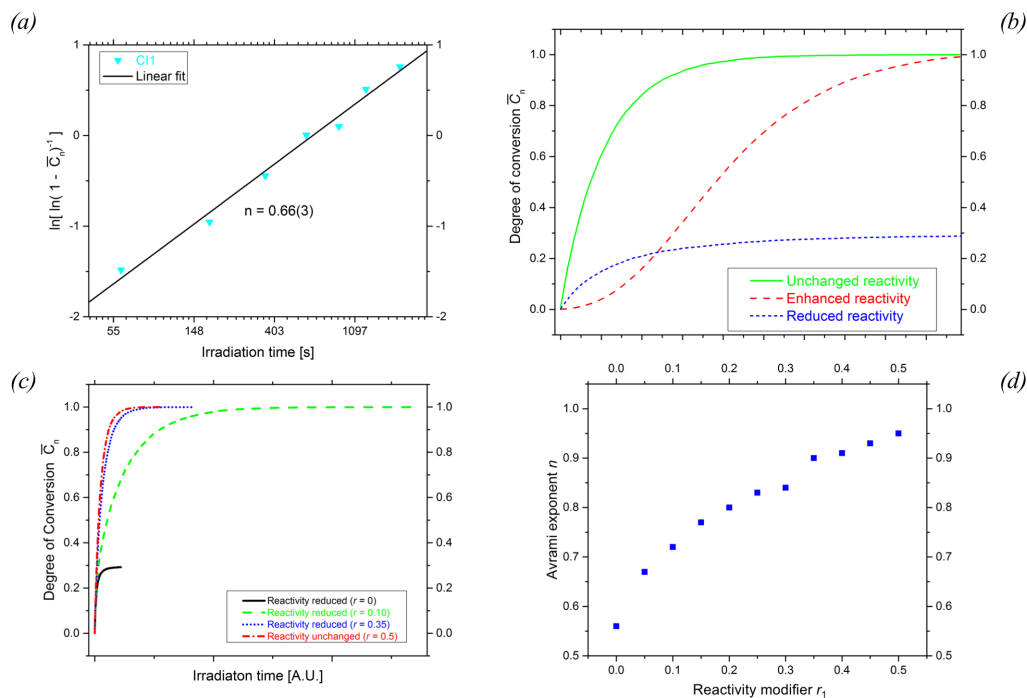


Figure 6.3: (a) Exemplary calculation of the Avrami exponent for *CI1* yields 0.66(3). The Avrami exponent averaged over all five crystals used for polymerization is 0.69(4). (b) Simulated reaction kinetics based on the models from *Figure 2.2*, assuming extreme values for the enhanced and reduced reactivity models. (c) Simulated reaction kinetics for different reduced models using different magnitudes to reduce the reactivity. (d) Avrami exponents for reduced models of different magnitudes.

to other molecules. In theory, the maximum value of \bar{C}_n would be $\frac{1}{3}$, but in practice it is slightly smaller because of frustration effects. The Avrami exponents of the three different basic models were calculated and yielded the expected Avrami exponents of 1 and 2 for the unchanged and enhanced reactivity models, while the reduced reactivity model with $r_1 = 0$ yielded an Avrami exponent of 0.55, *i.e.* smaller than 1 and therefore qualitatively similar to the experimental results. The reduced reactivity model was investigated further by modifying r_1 within the limits $0 \leq r_1 < 0.5$ which allows to form continuous mixtures between the reduced and random reactivity model. *Figure 6.3c* shows examples of the irradiation-time dependent evolution of such models with different values for r_1 and *Figure 6.3d* the Avrami exponents

for the whole range of tested models. All of them yield Avrami exponents smaller than 1, indicating that anthracene dimerization of the 2DP presented here restricts its direct neighbors in their reactivity and the corresponding r_1 factor is in the range of 0.05 to 0.15 to obtain $n \approx 0.69$.

Local impediment of bond formation may be explained by the local strain induced through the formation of a bond and the associated changes in distance between anthracene pairs, *Figure 6.4a*, which is a crucial factor for the reactivity (Schmidt, 1971). Indeed, as shown in *Figure 6.4b* the anthracene - anthracene distance of unbonded pairs tend to increase during polymerization. This nicely explains the self-impeding of the polymerization propagation as observed in the Avrami model analysis. While this explanation seems very likely, the Avrami formalism does not allow to distinguish reactivity changes along lateral and vertical directions. That leaves a small uncertainty about the propagation mechanism obtained from the *Avrami* model. Such detailed local structure investigations go beyond what can be learned from the average structure alone and will be further addressed when discussing substitutional disorder in *Section 6.2.2*.

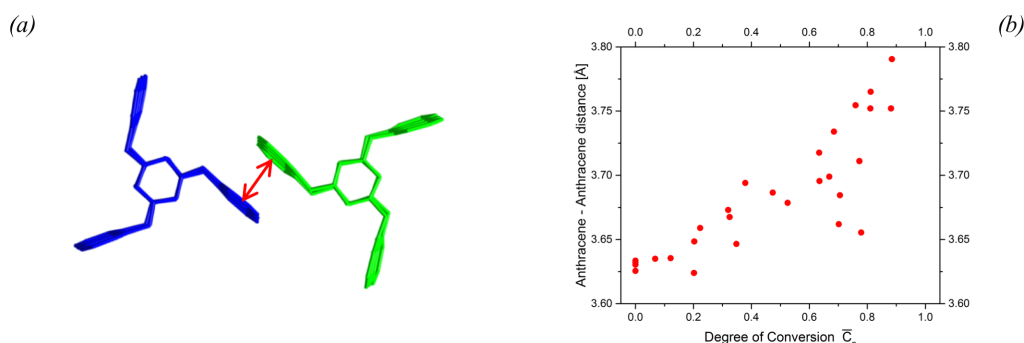


Figure 6.4: (a) Graphical representation of the average anthracene-anthracene distance between M_S and M_T . (b) Change of the average anthracene-anthracene distance between M_S and M_T upon polymerization.

The case for depolymerization propagation is less clear, because of fewer available data points and the lack of reference studies on anthracene cycloreversion. Depolymerization can be described with the same formalism and models as polymerization. However, instead of monitoring the impact of formed bonds on the formation of new bonds, we now monitor how a broken bond would enhance or reduce the rate of depolymerization in the next neigh-

borhood. The Avrami exponent extracted from the results of the depolymerization experiments is 0.84(7), indicating a self-impeding propagation model also in the case of depolymerization. This behavior can be explained if one assumes that a polymer layer is more stressed than a monomer layer, because of the deformations introduced during polymerization and, because the higher rigidity of the polymer layers does not allow a flexible adaptation to changes in its environment. Breaking of bonds would therefore reduce local stress in the polymer layers and reinforce the anthracene-anthracene bonds in the remaining polymer fragments. As a consequence, the probability that a given anthracene - anthracene bond gets broken within a certain time becomes smaller with progressing depolymerization.

6.2 Insights from diffuse scattering

6.2.1 Displacive disorder

As shown in *Table 5.3*, all U^{AB} matrices referring to intramolecular displacements show strong positive correlations for the main-diagonal entries and negligible correlations for the off-diagonal entries. These correlations show that M_S , M_T , P_S , P_T , P_T and the template behave like rigid bodies in a first approximation and that the intramolecular displacive disorder is dominated by translations rather than librations. The internal rigidity of molecules and moieties is maintained throughout polymerization. Correlations between opposite blades from M_S and M_T decline weakly upon polymerization. The most likely reason for this decrease is that dimers belonging to the same molecular part as the unbound blade reduce the mobility of the entire moiety and thus the interaction possibilities of the unbound blade.

The strong correlations between the edge-to-face stacked blades of M_S and the template, *Table 5.5*, are surprising given that they appear rather far apart in the structure drawings in this work. However, hydrogen atoms are not plotted in the majority of structure drawings. When considering the distances between the outermost hydrogen atoms of M_S and the template, they vary from 2.8 Å to 3.0 Å, which is actually the shortest inter-molecular distance within a layer. Upon polymerization, correlations between the template and polymer substructure are larger than those between the template and the monomer substructure, making the template stronger integrated

into the polymer substructure. This strong integration was demonstrated by Beyer *et al.* (2017). The surfaces of some 2DP crystals and partially exfoliated sheets were extensively studied using atomic force microscopy. It was expected to find depressions in the surfaces which should have formed if the template vacated the pores, leaving behind the hexagonal arrangement of the polymer. When the surface topography revealed no pores and a trigonal arrangement of elevations they concluded that the template must remain within the pores because the trigonal arrangement with the given spacing is only possible if the pores are filled by the template.

Intra-columnar displacements along the c -axis were expected to be equally directed, *i.e.* all positively correlated like dominoes pushing each other over, given the relatively high rigidity of blades and half-dimers. However, this was not the case, *cf.* all negative correlations highlighted in *Table 5.4* in purple, *i.e.* between P_S and P_T at a conversion ratio of 0.22. Additional simplified structure simulations were employed to study the appearance of negative correlations within the columns further. These simulations calculate all permutations of monomer molecules, polymer moieties and their displacements within a column of 200 molecules while assuming periodic boundary conditions. The displacive disorder was modeled only on a qualitative basis and is expressed as whether a molecule is displaced in the positive or negative direction within the column. About 20% of all permutations show a behaviour that is qualitatively and quantitatively similar to the values found in *Table 5.4*, *i.e.* negative correlations in the second neighborhood between M_S and M_T and negative correlations in the first and second neighborhood only at a \bar{C}_n of 0.22 between P_S and P_T .

The mechanism from the simulation results is interpreted in a simplified way as follows. In order to dimerize, M_S and M_T have to move along the c -axis in opposite directions, indicated in *Figure 6.5a* by arrows *outside* of the rectangular representations for the monomers. In the monomer crystals, M_S and M_T are intrinsically disordered along the c -axis, indicated in *Figure 6.5b* by arrows *inside* of the rectangular representations for the monomers. Individual monomer pairs could be either displaced in the same direction (positive correlation) or in different directions (negative correlations). In the example depicted in *Figure 6.5b*, the average correlation of all molecule pairs equals to zero. The intrinsic displacements of M_S and M_T along c make those molecules that are displaced in the same direction as the motion required for dimer-

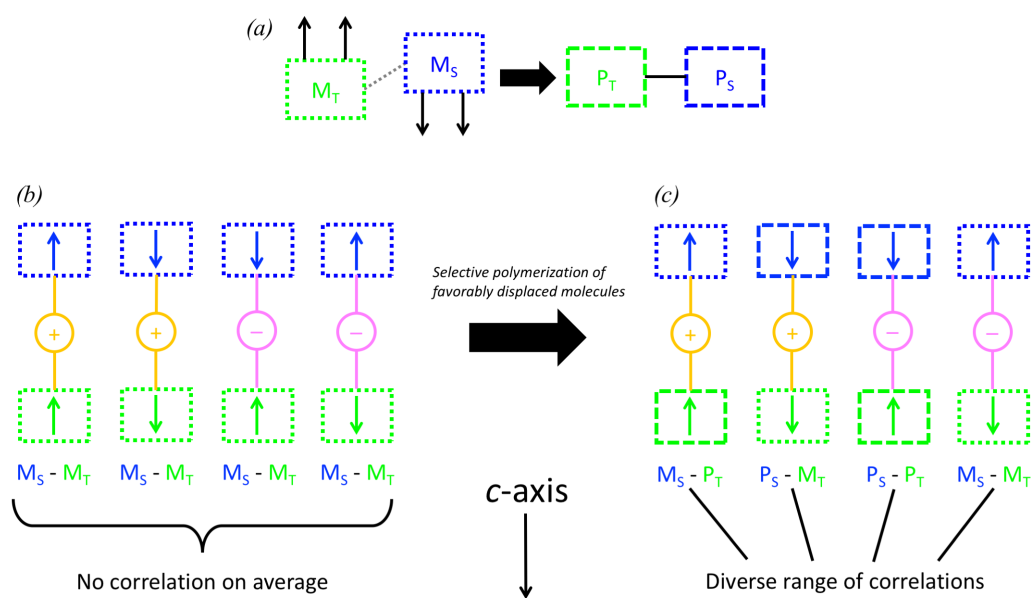


Figure 6.5: Schematic representation of how selective polymerization can change correlations. (a) Polymerization requires that monomers within a layer move along the columns in different directions in order to polymerize. (b) Schematic drawing of multiple columns containing the second neighbors M_S and M_T , separated by a template (not drawn for clarity), where each molecule is displaced along the column, as indicated by arrows, and are overall not correlated. (c) Same stacks as in (b) though monomers that were displaced in the same direction as the motion required for dimerization (M_S down, M_T up) were polymerized. This selective polymerization changed the correlations between moieties. Notable, the previous uncorrelated monomers M_S and M_T became negatively correlated. Dotted boxes refer to monomer molecules, dashed boxes to their polymerized counterparts.

ization more likely to dimerize because they are closer to their dimerization partner¹⁰. When dimerizing only those molecules that favor dimerization due to their internal displacements, and then consider their correlations, the previously uncorrelated molecules M_S and M_T became in the given example negatively correlated, *Figure 6.5c*.

The displacive disorder in the partially polymerized structures is most likely of static origin, which was already indicated by the average structure. This is evident when comparing the ADPs from measurements made at different temperatures, *Figure 5.3*. In the monomer state, the ADPs decrease when the temperature is reduced, as is expected for thermal movements. As soon as polymerization begins, however, the ADPs from low and room temperature measurements become more similar, indicating increasing contributions from static displacements.

6.2.2 Substitutional disorder

The results of the substitutional disorder from the diffuse scattering experiments differ in the second and third topological neighborhood from the results of the Avrami model (*Figure 5.14*) which is based on the Bragg data, *Figure 6.6*. According to the MC simulation, the first neighbors are stronger correlated throughout the polymerization than in the actual experiments. Similarly, the second neighborhood never has negative correlations in the MC simulation, and the third neighborhood is more strongly correlated than expected. A particular striking feature is also the lack of change from negative to positive correlations in parts of the second and third neighborhood.

The previously used MC simulation was extended by additional modifiers that influence further topological neighborhoods. For that purpose, the same design principle as for the first neighborhood (see *Section 6.1.2*) were used. Four r -modifiers were used as parameters, one for the first, two for the second and one for parts the third topological neighborhood, called r_1 , r_2 , r_3 and r_4 . Two parameters for the second neighborhood made it possible to group the second topological neighbors according to their different geometric distances. The r -modifiers were subjected to differential evolution (DE) minimization

¹⁰The concept of reaction probabilities changing with distance between reactive moieties is explored in depth in *Sections 2.3.4* and *6.1.2*.

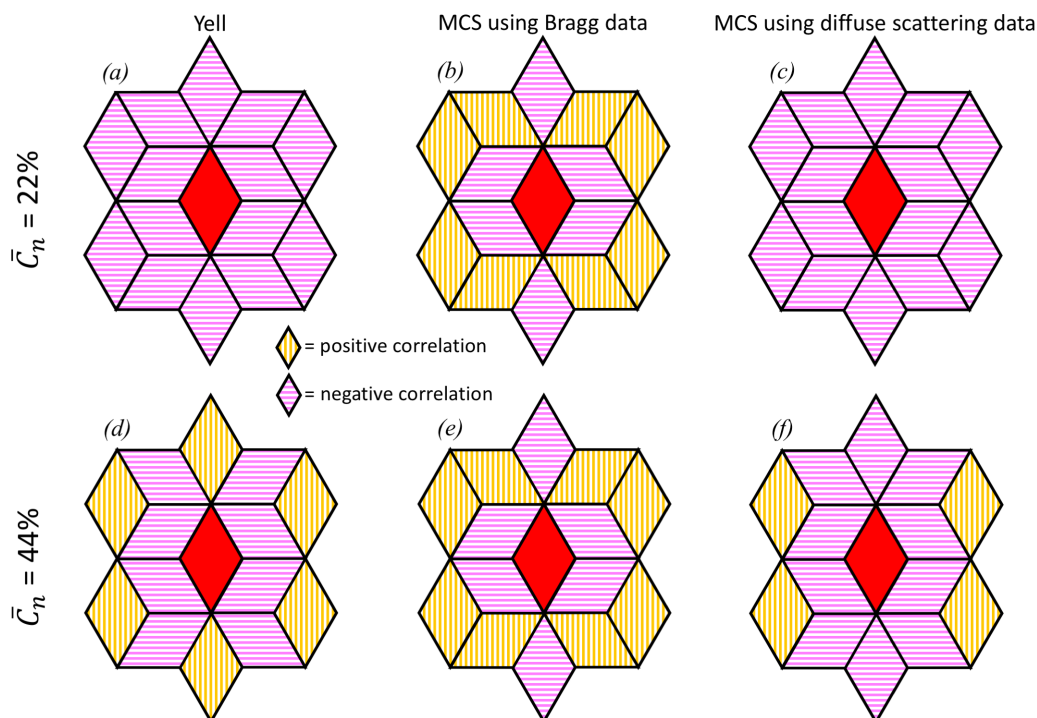


Figure 6.6: Qualitative distribution of positive and negative correlations (a) as refined by *Yell*, (b) for the MC simulation considering decreased reactivity ($r_1 = 0.15$) in first topological neighborhood and (c) for the MC simulation considering decreased reactivity up to the third topological neighborhood at a \bar{C}_n of 0.22. Correlations (d) as reported by *Yell*, (e) MC simulation for the first topological and (f) additional topological neighborhoods at a \bar{C}_n of 0.44.

(Storn and Price, 1997) to find the best set of r -modifiers to explain the observed substitutional correlations. The objective function to be minimized was the square sum of the differences between correlations obtained from *Yell* and the MC simulation. Python's implementation of the DE algorithm was used with ten individuals per parameter and was executed in parallel mode on EULER. Again, parallel computing was an essential component because each of the forty individuals per generation could be calculated on a separate computing core, therefore drastically reducing the wall-clock time of the minimization. *Figure 6.6* shows the improvement when involving the second and third neighbors by comparing the distribution of positive and negative correlations at different conversion ratios.

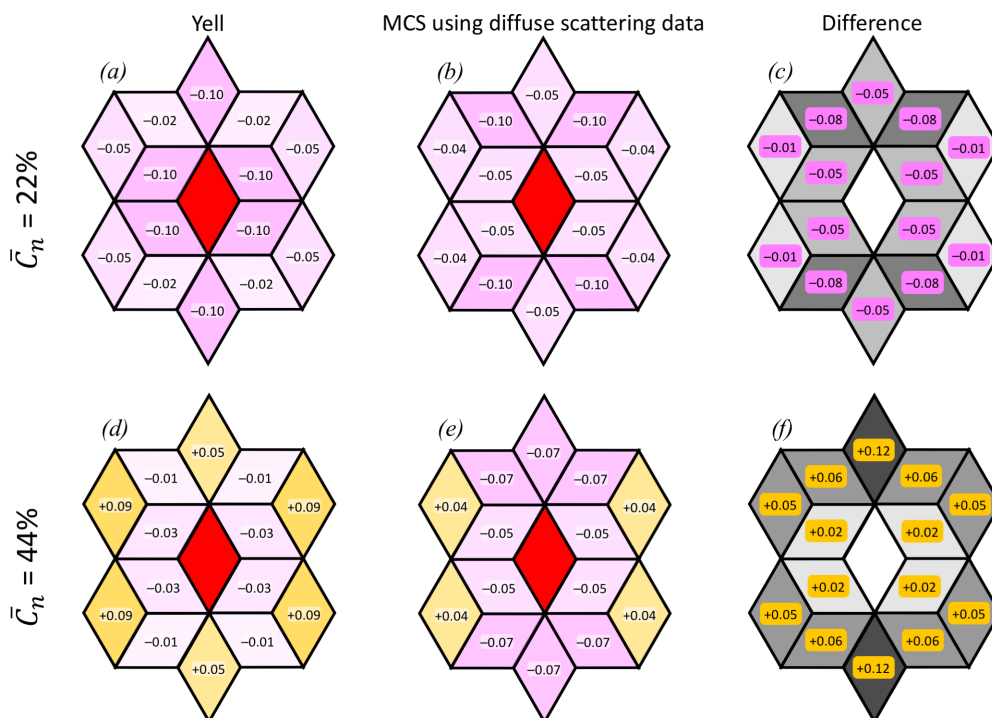


Figure 6.7: (a) the *Yell* model compared to (b) the MC simulation and (c) their difference at a \bar{C}_n of 0.22 as well as (d) the *Yell* model compared to (e) the MC simulation and (f) their difference at a \bar{C}_n of 0.44.

Three important observations and conclusions could be gathered by comparing the *Yell* models with the two MCs simulations and by extending the change in reactivity to moieties further away. First, the change from negative to positive correlations as seen in *Figure 6.6a,d*, can be achieved in any topological neighborhood larger than one, even when a reduced reactivity is assumed for all neighborhoods. At a low \bar{C}_n , dimers have enough space to avoid each other relatively well, but at higher \bar{C}_n the need to form new dimers creates specific spots which are more accommodating for dimerization. Second, the MC simulations are surprisingly sensitive to the input parameters. Changes of or below 1 percentage point in an r -modifier result in significant changes in the correlation development during polymerization. For example, such minor changes influence if and at which \bar{C}_n a change in correlation parity occurs. Finally, no single set of r -modifiers was found by the refinement to explain the *Yell* models satisfactorily because at least one correlation value obtained from the MC simulation will not correspond to a correlation value

from the *Yell* model. The best obtained set of r -modifiers for both investigated intermediate states is 0.31(7), 0.17(5), 0.28(8) and 0.55(10) for the first, second, and the two differentiated third neighbors, respectively. The errors represent the spread in the population after convergence of DE minimization. This set of parameters agrees reasonably well with the qualitative (*Figure 6.6*) and quantitative (*Figure 6.7*) *Yell* model at a \bar{C}_n of 0.22. However, at a \bar{C}_n of 0.44 a qualitative mismatch appears. While the first and second neighborhood are well reproduced, the third neighborhood has the wrong parity as seen in *Figure 6.6f*. Apart from this outlier, the quantitative match is acceptable, *Figure 6.7f*.

There are two possible explanations why the DE was not able to provide a perfectly fitting model. First, the symmetry introduced into the model (*cf. Figure 4.5*) might be too restrictive. Second, the model could be too simplistic¹¹. Furthermore, when looking at the difference between the results obtained from *Yell* and the refined MC simulation, *Figure 6.7c,f*, all differences at a \bar{C}_n of 0.22 are negative and all differences at a \bar{C}_n are positive, indicating a systematic error.

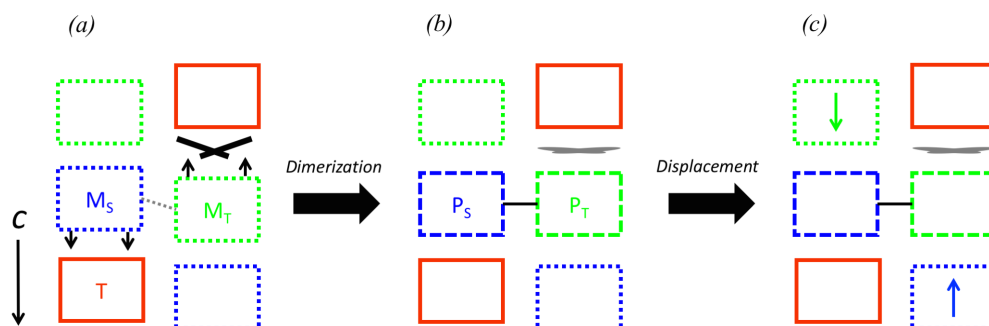


Figure 6.8: A possible explanation for the negative substitutional correlations above and below dimers. (a) In the monomer structure, M_S and M_T (blue and green dotted boxes) have to move along c in opposite directions to dimerize, thereby exerting pressure on the template and solvent (red full box and crossed black lines), see also *Figure 6.1a,b*. (c) The channel opening caused by dimerization enables the monomer molecules above and below to move into that space.

¹¹The model simplifications are given in *Section 6.1.2*.

When considering the substitutional disorder across the layers, *Figure 5.15b,d*, it is less likely that dimers form above or below existing dimers. One possible explanation for this behavior is the channel opening (*cf. Figure 6.1*) that occurs during polymerization. During dimerization, *Figure 6.8a,b* the monomers must move along c into the layer. The corresponding channel opening allows monomers in adjacent layers to move a little into the opening gap, *Figure 6.8c*. This small displacement increases the distance of the monomers to their dimerization partners, which reduces the reaction probability according to Schmidt's rule (Schmidt, 1971). Note that these small displacements could also be caused by lateral movements.

7 Conclusion

7.1 Overview

For the system studied here, approximately one million carbon-carbon bonds per μm^2 are formed to obtain a single, well-ordered macromolecule. In addition, this chemical transformation converts independent monomer molecules into stacks of 2DP sheets that ideally span throughout the entire crystal. In view of this complexity, it is important to understand why polymerization nevertheless takes place, and which mechanisms support it. Given the crystallinity of 2DPs, total X-ray scattering techniques have proven to be an excellent tool for investigating this single-crystal-to-single-crystal transformation with atomic resolution. For the first time, the polymerization and depolymerization propagation of a two-dimensional polymer was investigated in detail. It was found that polymerization is predominantly random, with aspects of a repulsive growth mechanism within and surprisingly across the layers. Depolymerization proceeds in a similarly random fashion with a tendency to evenly distribute bond-breaking events throughout the layer. Such processes have unprecedented complexity as far as the number of bond formation and bond breaking events per unit area are concerned.

7.2 Propagation mechanisms

Unraveling two-dimensional polymerization using total X-ray scattering requires two steps, understanding the average and the real crystal structure. First, all relevant structural parameters from the average structure were determined as a function of reaction conversion. This provided insights into several of the structural changes that occurred during the transformation from monomer to polymer and back. Results obtained from such complex solid-state-reactions experiments may be very sensitive to small variations in sample preparation, experimental setup, and data analysis. Therefore, repeating the experiments with several crystals under different experimental conditions and testing various data evaluation approaches turned out to be essential for estimating the reproducibility and the reliability of the results. Second, the changes in the crystal's 3D- Δ PDF were studied to gather information about the real structure. Not only did this verify and further

support the propagation mechanism as extracted from the average structure, it also showed that the growing 2DP-layers in the crystal influence each other, making two-dimensional polymerization a three-dimensional process.

In general, the conversion ratio and the propagation mechanisms of polymerization and depolymerization have an impact on the topology, homogeneity, and size of exfoliated sheets. Detection and design of exploitable properties in partially polymerized structures could be of even higher interest than the fully polymerized end-product itself. Although Bragg scattering-based information alone does not deliver a complete model, it was shown that the *Avrami* formalism is a promising and easy-to-use tool for an initial characterization of the polymerization propagation mechanism, *Section 6.1.2*. By including results obtained from diffuse scattering, it was clearly shown that two-dimensional polymerization propagation is a much more multifaceted mechanism than Bragg scattering alone would suggest. The magnitude in reduction of the reactivity in the *Avrami* model from the average structure is overestimated when compared to the results from the diffuse scattering. Deriving the propagation mechanism from the *Avrami* model is a good qualitative indicator, but insufficient to describe the propagation mechanism as a whole. For example, the *Avrami* model suggests that the first topological neighborhood is primarily affected by a single dimerization event. However, the results from the diffuse scattering clearly show that this is not the case. Furthermore, the data obtained from the real structure show that a single dimer influences the reactivity of the second topological neighbors and some of the topological third neighbors within the layer as well as several additional geometric neighbors from adjacent layers.

The polymerization - depolymerization cycle is an asymmetric process, *Figure 5.2*. As seen from the rapid drop of the crystal volume after heat treatment, the crystal structure is out of thermodynamic equilibrium during polymerization. This is considered fortunate, since the metastable state allows polymerization while keeping the monomers close enough together to achieve full conversion. As a consequence, the number of microscopic or macroscopic cracks stays small enough to essentially preserve the single-crystalline state. In the course of heat-induced depolymerization, the crystal is closer to structural equilibrium. Depolymerization is a partially self-inhibiting process, in which heat treatment reduces local strain and keeps the polymer moieties close together, stabilizing the remaining bonds. Polymerization and de-

polymerization especially, which both require significant structural changes, leave the crystals intact. This remarkable finding is of particular importance regarding the obtainable single-layers from a crystal. The observation that a polymerization - depolymerization cycle does completely recover the monomer but not exactly its initial crystal structure suggests that polymerization cycling might be a suitable way for realizing structures that cannot be directly accessed from the fresh monomer.

7.3 Structural features promoting 2D polymerization

In order to make two-dimensional polymerization happen, two conditions must be met. First, anthracenes must have the right geometric relation to one another. Second, the surroundings of the reaction centers must be flexible enough to respond in a non-destructive way to the connectivity changes during polymerization. For the here-presented 2DP, the second aspect is fulfilled in particular by translocations of solvents and templates, *i.e.* the passive molecules. Regarding the solvent molecules, it is interesting to note that they act as a mechanical buffer and “lubricant“ between sheets during polymerization. The buffering-effect is also observed when considering the displacive disorder. The interactions along the *c*-axis between monomer/polymer and the template separated by the solvent are initially smaller than the interactions between monomer/polymer/template in direct contact, see *Table 5.4*. That difference becomes smaller with increasing conversion, indicating that the solvent has absorbed stress and has a decreased capacity to dissipate additional stress. The decreased capacity is also indicated by the solvent molecule itself, as it becomes more parallel with the *ab*-plane, see *Figure 5.7c,d*. The importance of the solvent for a complete characterization of the compound is further illustrated by its impact on the crystal’s physical properties: the upright solvent molecules introduce a significant electric dipole moment. Although the solvent molecule is partially disordered, the resulting calculated dipole moment at any conversion ratio is larger than that of water (Clough *et al.*, 1973), which can even be fine-tuned through the conversion ratio.

Given the currently available tools and knowledge, it is difficult, if not impossible, to tailor structural, chemical, or physical properties of two-dimensional polymers from scratch. A thorough crystallographic analysis of the intermediate and final products of a given compound, as carried out in this study,

provides further insights for crystal engineering in 2DPs. Several such studies could eventually provide guidelines for the future development of 2DPs and explain why a final product may or may not achieve its desired properties. This study provides three important insights from diffuse scattering, which have also enabled a better understanding of the polymerization mechanism. First, all molecular deformations and movements must be analyzed and understood in relation to the conversion ratio. Ideally, the monomer molecules would perfectly compensate for the deformation caused by dimerization. However, the results clearly show that the molecules are limited in that capacity, and that the solvent molecules sandwiched between monomer and polymer molecules play a key role in compensating for stress caused by deformation and displacement, *Section 5.2.3* and *Section 6.1.1*. Second, the diffuse scattering resulting from the displacive disorder provides a better understanding of the distribution of blades and dimers than the average structure alone would suggest, *Figure 6.6*. The diffuse scattering revealed that polymerization propagation is a primarily random process, although dimers prefer to avoid each other. This leads to a more even distribution of dimers during polymerization, which further reduces the local stress. Finally, the polymerization propagation also affects reactive centers belonging to another layer. Fortunately, this influence does not interfere in any way with the polymerization in the case presented here. It is conceivable, however, that although the molecules are perfectly arranged in the starting monomer, dimerization could take place in such a way that complete polymerization of adjacent layers is prevented. Real structure analysis would provide the experimental framework to identify and investigate these cases. Such insights are of critical importance for future monomer design, because it is not enough to just consider internal molecular deformations during, dimerization but also how the layers above and below are affected.

7.4 On exfoliation and single sheets

The results from the average structure analysis expose interesting findings related to liquid exfoliation. Within the columns, the molecules move further apart until they reach full polymerization, *Figures 5.4, 5.5*, which makes it easier for exfoliation agents to penetrate the structure and to push the sheets apart. Unfortunately, no real crystal structure analysis is available for the

fully polymerized state, and therefore no comments can be made on interactions between moieties within the column. Furthermore, when attempting liquid exfoliation, annealing is not recommended because it would cause a phase transformation, from space group $R3$ to $P3_1$, in which the molecules are much closer together within the columns, making it much harder for exfoliation agents to penetrate the structure.

Regarding the templates, it is noteworthy that at the beginning of polymerization they can easily dissipate any stress exerted on them by dimerization by moving along the c -axis. Towards the end of the polymerization, their degrees of translational freedom are reduced by the emerging polymer, *Figure 6.1*. Further information on the template's interactions are important regarding future applications, like molecular sieving, which would require the template to vacate the pore. Given the strong interactions between the template and the neighboring moieties within the layer found during this study, it seems unlikely that the templates vacate a sheet's pores spontaneously. This was confirmed in a study by Beyer *et al.* (2017). Note that bending motions of an individual sheet in solution would probably provide an adequate mechanism to remove the templates from the pores.

7.5 Modeling disorder via the 3D- Δ PDF method

An important additional aspect of this project was to thoroughly test the implementation of the 3D- Δ PDF method in the *Yell* program and to prove its capabilities. It was shown that it is possible to model and refine the disorder of large molecules and to investigate the change in disorder during a sophisticated phase transformation. It could be also shown that disorder can be modeled comparatively easily compared to Monte Carlo simulations while, requiring less computational power. Furthermore, modeling and expressing disorder via pair correlations and viewing the results in 3D- Δ PDF space, allows a semi-quantitative estimate of the parameters defining the disorder by eye with surprising accuracy within a comparatively short time. This is currently not possible with Monte Carlo simulations.

The work on data from the diffuse scattering was a challenging task. Since the diffuse scattering showed broad, three-dimensional features and was centered on Bragg reflections, the separation of these two was difficult. However,

improved computing power and software made it possible to experiment with different approaches to find the best separation method. Modeling the disorder was time consuming, labor-intensive and error-prone due to the low crystal symmetry, and the relatively large number of atoms in the asymmetric unit, but straightforward. The resulting 3D- Δ PDF maps could not be interpreted intuitively, unlike other examples (Sangiorgio *et al.*, 2018). However, the patterns of density distributions for displacive and substitutional disorder were very characteristic and effectively counteracted the error-prone modeling.

7.6 Final remarks

In summary, this work provides the first thorough investigation of the polymerization mechanism in a crystalline 2DP. It was shown that by using standard X-ray diffraction techniques and the 3D- Δ PDF method, two-dimensional polymerization propagation can be described in terms of crystalline disorder. This approach revealed, among many other interesting features, that the polymerization mechanism is best described as random with aspects of repulsive growth, and that stress compensation via different mechanisms is important to facilitate polymerization propagation. This project has been an enriching experience for myself, and it is my sincere hope that the results of this work will be a reference point for future research on 2DPs, phase transitions and disorder in crystals.

8 Outlook

8.1 Monomer and polymer

Many research opportunities remain for the monomer and polymer investigated in this study. Since the monomer and polymer structure are isotypic, it would be interesting to see if the monomer structure can be forced to undergo a phase transition to the $P3_1$ structure known from annealing, which has smaller cell parameters, through means of high pressure. The reduced symmetry might result in a different propagation mechanism.

The master project by Gabriele Pagani showed that light with a wavelength of 250 nm triggers cyclo-reversion of the anthracene dimers although it takes at least 24 h to achieve a small percentage of depolymerization. His findings show that the structural changes of thermal- and photodepolymerization are different. For example, the reduction of the c -axis observed during thermal depolymerization does not occur. However, more research is necessary to gain more detailed insights.

Several side effects of polymerization are also of interest. So far, the changes in the dipole moment were only calculated and independent measurements are necessary to determine the real strength. Also, after a polymerization and depolymerization cycle, the fully depolymerized structure is almost, but not quite, similar as the pristine monomer structure. It would be interesting to understand whether or not these deviations accumulate during multiple polymerization and depolymerization cycles and if this recycling gives access to exploitable intermediate states which cannot be obtained from the pristine monomer crystal.

The particular crystal morphology and the orientation of the crystallographic axes in relation to the morphology play an important role for future applications of 2DPs obtained from the single-crystal approach, as they restrict the maximum achievable sheet size and as they result in an intrinsic sheet-size distribution. Understanding the relation between the crystal lattice and the crystal morphology reveals further properties. The 2DP presented here is obtained from crystals with rhombohedral morphology, with the trigonal symmetry-axis being normal to the polymer layer. Therefore the intrinsic polydispersity of the sheet size is extremely broad. In theory, no two sheets

have the same size, *Figure 4.1c*. To obtain a large amount of a monodisperse fraction of a desired sheet size, several crystals must be exfoliated and the obtained sheets must be further processed to obtain the desired fraction.

8.2 Revisiting concepts and definitions

Definitions for polymers were written with linear polymers in mind, therefore some of them require an extension to account for the increased degrees of freedom in 2DPs. For example, oligomers require an additional identifier to distinguish different topologies comprised from the same number of monomer molecules, *Figure 8.1*. Similarly, the net topology opens up additional possibilities for tacticity, a subject that was briefly touched upon by Lange *et al.* (2017)

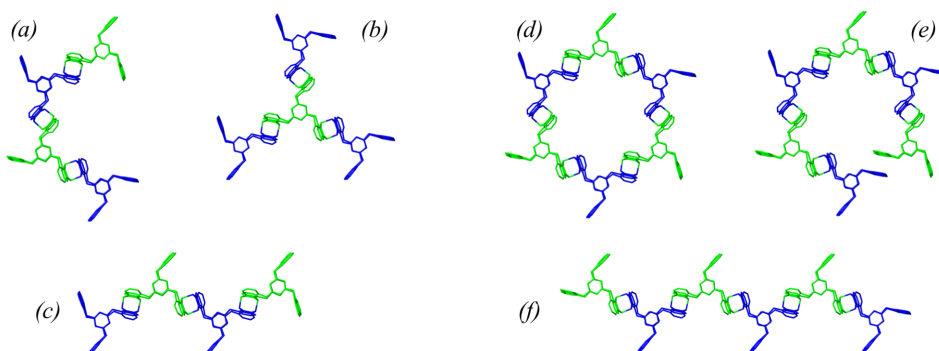


Figure 8.1: Several examples of oligomers that could occur in the studied 2DP. The term *n-mers*, *e.g.* tetramer (a to c) or hexamer (e to f), is ambiguous for oligomers that are capable of two-dimensional polymerization.

8.3 Monomer design, arrangement, and polymerization

The inspiration for the development of a monomer suitable for two-dimensional polymerization can come from any book or website dealing with tilings. For example, a pentafunctional monomer could be utilized in at least three different reactive arrangements to obtain a 2DP, *Figure 8.2*. An intrinsic advantage of using a non-regular tessellation is that an additional parameter can be exploited for pore size design. Additionally, the pores are intrinsically decorated with functional groups which could be used for post-polymerization

modification, similar to edge functionalization (Zhao *et al.*, 2016). A variety of different intermediate states and propagation mechanisms are expected from such novel arrangements. Some intermediate states of specific growth mechanisms might also be exploited for their properties. For example, *Figure 8.3a* shows how a specific growth mechanism would yield individual chains. Furthermore, irregular *Figure 8.3b* or regular *Figure 8.3c* net structures could be obtained from intermediated states. Diffuse scattering techniques could become an invaluable tool for identifying these. In my personal opinion, there are considerable synergies that can be exploited through the joint development of 2DPs and diffuse scattering techniques such as the 3D- Δ PDF method.

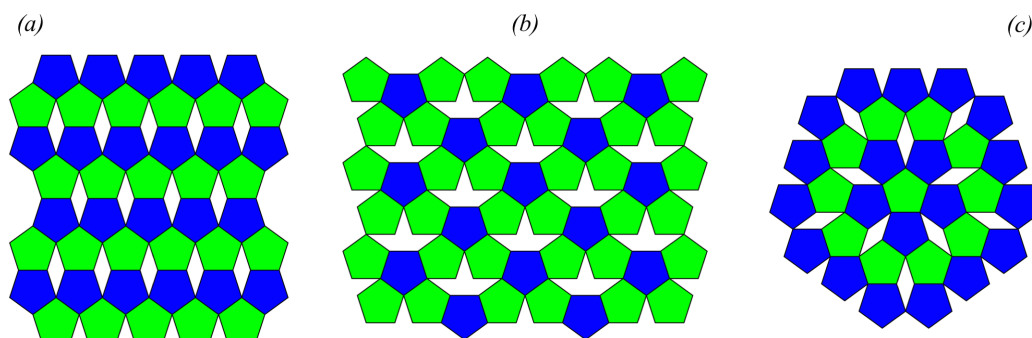


Figure 8.2: Three examples of 2DPs that could be obtained from a penta-functional monomer that have an intrinsic porosity. Note that (a) and (b) are periodic while (c) is aperiodic.

It is conceivable that stress and strain develop differently depending on the growth mechanism. When considering the previously introduced reactivity models, *Figure 2.2*, the unchanged and reduced reactivity model distribute stress throughout the crystal while the enhanced reactivity model creates a reaction front at which stress would be localized. Depending on the magnitude of the stress, such a reaction front can produce grain boundaries in the single crystal that prevent continuous growth and thus drastically reduce the achievable sheet sizes.

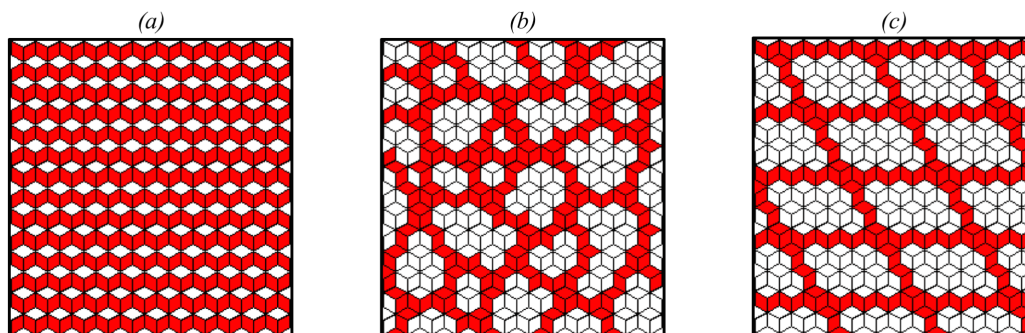


Figure 8.3: Concept drawings of hypothetical intermediate states of an unspecified growth mechanism during polymerization from which (a) linear polymers, (b) irregular nets or (c) regular nets could be obtained. A white rhomb represents a reactive center ready to dimerize while a red rhomb represents an already dimerized site.

8.4 3D- Δ PDF modeling

An important aspect to advance real crystal structure analysis using the 3D- Δ PDF method is to streamline the work flow with diffuse scattering data. Yell has closed a big gap in the processing pipeline, by providing a general framework to model disorder, but self-made scripts are still required for transferring and analyzing data.

The results from this study and other works regarding displacive disorder (Bosak *et al.*, 2015) show that diffuse scattering is capable of probing the correlated dynamic or static displacements between two molecules. This information bears some similarities with spectroscopic methods such as infrared spectroscopy which probes internal vibration modes of a molecule. Although analyzing displacive disorder is not yet sufficiently developed in terms of practical application or precision with respect to spectroscopic methods, it could provide a valuable framework for future measurement techniques that complement spectroscopy.

9 References

- Agilent (2015). *CrysAlis PRO*. Agilent Technologies Ltd.
- Albouy, P.-A., Patillon, J.-N. and Pouget, J.-P. (1983). *Mol. Cryst. Liq. Cryst.* **93**(1), 239–246.
- Avrami, M. (1939). *J. Chem. Phys.* **7**(12), 1103–1112.
- Avrami, M. (1940). *J. Chem. Phys.* **8**(2), 212–224.
- Avrami, M. (1941). *J. Chem. Phys.* **9**(2), 177–184.
- Bae, S., Kim, S. J., Shin, D., Ahn, J.-H. and Hong, B. H. (2012). *Phys Scr.* **2012**(T146), 014024.
- Baughman, R. H. (1974). *Sci. B Polym. Phys.* **12**(8), 1511–1535.
- Baughman, R. H. and Chance, R. R. (1980). *J. Chem. Phys.* **73**(8), 4113–4125.
- Becker, H. D., Andersson, K. and Sandros, K. (1985). *J. Org. Chem.* **50**(20), 3913–3916.
- Beyer, H., Kory, M. J., Hofer, G., Stemmer, A. and Schlüter, A. D. (2017). *Nanoscale*, **3**, 20.
- Bhatia, R. (2007). *Positive definite matrices*. Princeton series in applied mathematics. Princeton, N.J: Princeton University Press.
- Bhola, R., Payamyar, P., Murray, D. J., Kumar, B., Teator, A. J., Schmidt, M. U., Hammer, S. M., Saha, A., Sakamoto, J., Schlüter, A. D. and King, B. T. (2013). *J. Am. Chem. Soc.* **135**(38), 14134–14141.
- Billinge, S. J. L. (2019). *Philos. Trans. Royal Soc. A*, **377**(2147), 20180413.
- Boldyreva, E. (1987a). *React. Solid.* **3**(3), 185–203.
- Boldyreva, E. (1987b). *React. Solid.* **3**(3), 205–225.
- Boldyreva, E. and Salikhov, K. (1985). *React. Solid.* **1**(1), 3–17.
- Bosak, A., Chernyshov, D., Wehinger, B., Winkler, B., Le Tacon, M. and Krisch, M. (2015). *J. Phys. D*, **48**(50), 504003.
- Bouas-Laurent, H., Castellán, A. and Desvergne, J.-P. (1980). *Pure Appl. Chem.* **52**(12).
- Bouas-Laurent, H., Castellán, A., Desvergne, J. P. and Lapouyade, R. (2000). *Chem. Soc. Rev.* **29**(1), 43–55.

- Bouas-Laurent, H., Desvergne, J.-P., Castellán, A. and Lapouyade, R. (2001). *Chem. Soc. Rev.* **30**(4), 248–263.
- Bragg, W. H. and Bragg, W. L. (1913). *Proc. Royal Soc. A*, **88**(605), 428–438.
- Charles, Z. B., Farber, M., Johnson, C. R. and Kennedy-Shaffer, L. (2013). *Linear Algebra and its Applications*, **438**(3), 1427–1445.
- Choi, W., Lahiri, I., Seelaboyina, R. and Kang, Y. S. (2010). *Cr. Rev. Sol. State*, **35**(1), 52–71.
- Chung, C., Kim, Y.-K., Shin, D., Ryoo, S.-R., Hong, B. H. and Min, D.-H. (2013). *Acc. Chem. Res.* **46**(10), 2211–2224.
- Clough, S. A., Beers, Y., Klein, G. P. and Rothman, L. S. (1973). *J. Chem. Phys.* **59**(5), 2254–2259.
- Coates, C., Gray, H., Bulled, J., Boström, H., Simonov, A. and Goodwin, A., (2018). Ferroic multipolar order and disorder in cyanoelpasolite molecular perovskites. https://chemrxiv.org/articles/Ferroic_Multipolar_Order_and_Disorder_in_Cyanoelpasolite_Molecular_Perovskites/7358363/1. Accessed: 2019-04-23.
- Colson, J. W. and Dichtel, W. R. (2013). *Nat. Chem.* **5**(6), 453.
- Cote, A. P., Benin, A. I., Ockwig, N. W., O’Keeffe, M., Matzger, A. J. and Yaghi, O. M. (2005). *Science*, **310**(5), 1166–1170.
- Cowley, J. M. (1950a). *Phys. Rev.* **77**(5), 669–675.
- Cowley, J. M. (1950b). *J. Appl. Phys.* **21**(1), 24–29.
- Cyvin, S. (1968). *Molecular Vibrations and Mean Square Amplitudes*. Universitetsforlaget, Oslo, and Elsevier, Amsterdam.
- Debye, P. (1913). *Ann. Phys. (Leipzig)*, **348**(1), 49–92.
- Dolomanov, O. V., Bourhis, L. J., Gildea, R. J., Howard, J. A. K. and Puschmann, H. (2009). *J. Appl. Crystallogr.* **42**(2), 339–341.
- Dong, R., Zhang, T. and Feng, X. (2018). *Chem. Rev.* **118**(13), 6189–6235.
- Dou, L., Wong, A. B., Yu, Y., Lai, M., Kornienko, N., Eaton, S. W., Fu, A., Bischak, C. G., Ma, J., Ding, T., Ginsberg, N. S., Wang, L. W., Alivisatos, A. P. and Yang, P. (2015). *Science*, **349**(6255), 1518–1521.
- Dou, L., Zheng, Y., Shen, X., Wu, G., Fields, K., Hsu, W. C., Zhou, H., Yang, Y. and Wudl, F. (2014). *Science*, **343**(6168), 272–277.
- Dyadkin, V. (2015). *Swiss-Norwegian Beamlines, European Synchrotron Radiation Facility, Grenoble, France*.

- Eddaoudi, M., Kim, J., Rosi, N., Vodak, D., Wachter, J., O’keeffe, M. and Yaghi, O. M. (2002). *Science*, **295**(5554), 469–472.
- Enkelmann, V., Wegner, G., Novak, K. and Wagener, K. B. (1993). *J. Am. Chem. Soc.* **115**(22), 10390–10391.
- Feng, X., Ding, X. and Jiang, D. (2012). *Chem. Soc. Rev.* **41**(18), 6010–6022.
- Feng, X. and Schlüter, D. (2018). *Angew. Chem. Int. Edit.* pp. 1–17.
- Flack, H. D. and Bernardinelli, G. (2008). *Chirality*, **20**(5), 681–690.
- Flory, P. J. (1953). *Principles of polymer chemistry*. Cornell University Press.
- Foundation, F. S., (2019). Gnu bash manual. <http://www.gnu.org/software/bash/manual/>.
- Friedrich, W., Knipping, P. and Laue, M. (1913). *Ann. Phys. (Leipzig)*, **346**(1), 971–988.
- Gedde, U. (1995). *Polymer physics. 1995*. Chapman & Hall: London.
- Greene, F. D., Misrock, S. L. and Wolfe, J. R. (1955). *J. Am. Chem. Soc.* **77**(14), 3852–3855.
- Grimm, H., Axe, J. D. and Kröhnke, C. (1982). *Phys. Rev. B*, **25**(3), 1709–1716.
- Hamilton, W. C. (1965). *Acta Cryst.* **18**(3), 502–510.
- Hasegawa, M. (1983). *Chem. Rev.* **83**(5), 507–518.
- Hay, J. N. (1971). *Brit. Polym. J.* **3**(2), 74–82.
- Haynes, W. M. (2014). *CRC Handbook of Chemistry and Physics, 95th Edition*. CRC Press.
- Henrich, B., Bergamaschi, A., Broennimann, C., Dinapoli, R., Eikenberry, E. F., Johnson, I., Kobas, M., Kraft, P., Mozzanica, A. and Schmitt, B. (2009). *Nucl. Instr. Meth. Phys. Res. A*, **607**(1), 247–249.
- Higham, N. J. (1990). In *Reliable numerical computation*, pp. 161–185. Oxford Univ. Press, New York.
- Hoang, T., Lauher, J. W. and Fowler, F. W. (2002). *J. Am. Chem. Soc.* **124**(36), 10656–10657.
- Hofer, G., Grieder, F., Kröger, M., Schlüter, D, A. and Weber, T. (2018). *J. Appl. Crystallogr.* **51**(2), 481–497.
- Huang, K. (1947). *Proc. Royal Soc. A*, **190**(1020), 102–117.

- Jenkins, A. D., Kratochvíl, P. and Stepto, R. (1996). *Pure Appl. Chem.* **68**(12).
- Johnson, W. A. and Mehl, R. F. (1939). *Trans. AIME*, **135**(8), 396–415.
- Johnston, P., Braybrook, C. and Saito, K. (2012). *Chem. Sci.* **3**(7), 2301–2306.
- Jones, R. G., Wilks, E. S., Metanomski, W. V., Kahovec, J., Hess, M., Stepto, R. and Kitayama, T. (2009). *Compendium of Polymer Terminology and Nomenclature*. IUPAC Recommendations 2008. Royal Society of Chemistry.
- Kabsch, W. (1988). *J. Appl. Crystallogr.* **21**(6), 916–924.
- Kabsch, W. (2010). *Acta Crystallogr. D*, **66**(2), 125–132.
- Keen, D. A. and Goodwin, A. L. (2015). *Nature*, **521**(7552), 303–309.
- Kissel, P., Erni, R., Schweizer, W. B., Rossell, M. D., King, B. T., Bauer, T., Götzinger, S., Schlüter, A. D. and Sakamoto, J. (2012). *Nat. Chem.* **4**(4), 287–291.
- Kissel, P., Murray, D. J., Wulftange, W. J., Catalano, V. J. and King, B. T. (2014). *Nat. Chem.* **6**(9), 774–778.
- de Klijn, T., Schreurs, A. M. M. and Kroon-Batenburg, L. M. J. (2019). *IUCrJ*, **6**(2), 277–289.
- Kluyver, T., Ragan-Kelley, B., Pérez, F., Granger, B. E., Bussonnier, M., Frederic, J., Kelley, K., Hamrick, J. B., Grout, J., Corlay, S. *et al.* (2016). In *ELPUB*, pp. 87–90.
- Knudsen, E. B., Sørensen, H. O., Wright, J. P., Goret, G. and Kieffer, J. (2013). *J. Appl. Crystallogr.* **46**(2), 537–539.
- Kolmogorov, A. N. (1937). *Bull. Acad. Sci. USSR, Math. Ser.*, **1**, 355–359.
- Kopský, V. and Litvin, D. (2010). *International Tables for Crystallography, Vol. E, Subperiodic Groups*. Wiley.
- Kory, M. J., Bergeler, M., Reiher, M. and Schlüter, A. D. (2014a). *Chem. Eur. J.* **20**(23), 6934–6938.
- Kory, M. J., Wörle, M., Weber, T., Payamyar, P., van de Poll, S. W., Dshemuchadse, J., Trapp, N. and Schlüter, A. D. (2014b). *Nat. Chem.* **6**(9), 779–784.
- Lange, R. Z., Hofer, G., Weber, T. and Schlüter, A. D. (2017). *J. Am. Chem. Soc.* **139**(5), 2053–2059.
- Laue, M. V. (1918). *Ann. Phys.* **361**(1), 497–506.

- Launois, P. and Moret, R. (2000). *J. Phys. IV*, **10**(P3), 193–204.
- Liu, W. and Loh, K. P. (2017). *Acc. Chem. Res.* **50**(3), 522–526.
- Liu, W., Luo, X., Bao, Y., Liu, Y. P., Ning, G.-H., Abdelwahab, I., Li, L., Nai, C. T., Hu, Z. G., Zhao, D., Liu, B., Quek, S. Y. and Loh, K. P. (2017). *Nat. Chem.* **9**(6), 563.
- Lotz, B. and Kovacs, A. (1969). *Poly. Chem.* **10**, 820.
- Medishetty, R., Park, I.-H., Lee, S. S. and Vittal, J. J. (2016). *Chem. Commun.* **52**(21), 3989–4001.
- Millman, K. J. and Aivazis, M. (2011). *Comput. Sci. Eng.* **13**(2), 9–12.
- Momma, K. and Izumi, F. (2011). *J. Appl. Crystallogr.* **44**(6), 1272–1276.
- Moret, R., Launois, P., Wågberg, T. and Sundqvist, B. (2000). *Eur. Phys. J. B*, **15**(2), 253–263.
- Moret, R., Launois, P., Wågberg, T., Sundqvist, B., Agafonov, V., Davydov, V. A. and Rakhmanina, A. V. (2004). *Eur. Phys. J. B*, **37**(1), 25–37.
- Müller, V., Hinaut, A., Moradi, M., Baljovic, M., Jung, T. A., Shahgaldian, P., Möhwald, H., Hofer, G., Kröger, M., King, B. T., Meyer, E., Glatzel, T. and Schlüter, A. D. (2018). *Angew. Chem.* **48**, 1030.
- Müller, V., Hungerland, T., Baljovic, M., Jung, T., Spencer, N. D., Eghlidi, H., Payamyar, P. and Schlüter, A. D. (2017). *Adv. Mater.* **29**(27), 1701220.
- Nassau, K. (1978). *Am. Mineral.* **63**(3-4), 219–229.
- Nassau, K. (1983). *The Physics and Chemistry of Color*. Wiley.
- Neff, V. D. (1978). *J. Electrochem. Soc.* **125**(6), 886–887.
- Novak, K., Enkelmann, V., Wegner, G. and Wagener, K. B. (1993). *Angew. Chem. Int. Ed.* **105**(11), 1678–1680.
- Novoselov, K., Mishchenko, A., Carvalho, A. and Neto, A. C. (2016). *Science*, **353**(6298), aac9439.
- Novoselov, K. S., Geim, A. K., Morozov, S. V., Jiang, D., Zhang, Y., Dubonos, S. V., Grigorieva, I. V. and Firsov, A. A. (2004). *Science*, **306**(5696), 666–669.
- Oliphant, T. E. (2006). *A guide to NumPy*, vol. 1. Trelgol Publishing USA.
- Oliphant, T. E. (2007). *Comput. Sci. Eng.* **9**(3), 10–20.
- OriginLab (2015). *Origin PRO*. OriginLab.

- Oszlányi, G. and Forro, L. (1995). *Solid State Commun.* **93**(4), 265–267.
- Oszlányi, G. and Sütő, A. (2004). *Acta Crystallogr. Sect. A*, **60**(Pt 2), 134–141.
- Oyedele, A. D., Yang, S., Liang, L., Puretzky, A. A., Wang, K., Zhang, J., Yu, P., Pudasaini, P. R., Ghosh, A. W., Liu, Z., Rouleau, C. M., Sumpster, B. G., Chisholm, M. F., Zhou, W., Rack, P. D., Geohegan, D. B. and Xiao, K. (2017). *J. Am. Chem. Soc.* p. jacs.7b04865.
- Palatinus, L. and Chapuis, G. (2007). *J. Appl. Crystallogr.* **40**(4), 786–790.
- Palmer, D. C. (2014). *CrystalMaker*. CrystalMaker Software Ltd.
- Paściak, M., Ondrejčovic, P., Kulda, J., Vaněk, P., Drahoš, J., Steciuk, G., Palatinus, L., Welberry, T. R., Fischer, H. E., Hlinka, J. and Buixaderas, E. (2019). *Phys. Rev. B*, **99**(10), 104102.
- Payamyar, P., Kaja, K., Ruiz Vargas, C., Stemmer, A., Murray, D. J., Johnson, C. J., King, B. T., Schiffmann, F., VandeVondele, J., Renn, A., Götzinger, S., Ceroni, P., Schütz, A., Lee, L. T., Zheng, Z., Sakamoto, J. and Schlüter, A. D. (2014). *Adv. Mater.* **26**(13), 2052–2058.
- Payamyar, P., King, B. T., Öttinger, H. C. and Schlüter, A. D. (2016). *Chem. Com.* **52**(1), 18–34.
- Peplow, M. (2016). *Nature*, **536**(7616), 266–268.
- Pérez, F. and Granger, B. E. (2007). *Comput. Sci. Eng.* **9**(3), 21–29.
- Perreault, F., de Faria, A. F. and Elimelech, M. (2015). *Chem. Soc. Rev.* **46**(39), 5861–5896.
- Pethrick, R. A. (2007). *Polymer Structure Characterization*. The Royal Society of Chemistry.
- Petříček, V., Dušek, M. and Palatinus, L. (2014). *Z. Kristallogr. Cryst. Mater.* **229**(5).
- PlasticsEurope, (2019). European plastics industry market data. <https://www.plasticseurope.org/en/resources/market-data>. Accessed: 2019-04-17.
- de Poel, W., Elemans, J. A., van Enckevort, W. J., Rowan, A. E. and Vlieg, E. (2019). *Chem.: Eur. J.* **25**(15), 3756–3760.
- Rao, A. M., Zhou, P., Wang, K. A., Hager, G. T., Holden, J. M., Wang, Y., Lee, W. T., Bi, X. X., Eklund, P. C., Cornett, D. S., Duncan, M. A. and Amster, I. J. (1993). *Science*, **259**(5097), 955–957.
- Ravy, S., Launois, P. and Moret, R. (1996). *Phys. Rev. B*, **53**(16), R10532–R10535.

- Rees, B., Jenner, L. and Yusupov, M. (2005). *Acta Crystallogr. D*, **61**(9), 1299–1301.
- van Rossum, G. (1995). *Python reference manual*. Tech. Rep. CS-R9526. Centrum voor Wiskunde en Informatica (CWI), Amsterdam.
- Sakamoto, J., van Heijst, J., Lukin, O. and Schlüter, A. D. (2009). *Angew. Chem. Int. Edit.* **48**(6), 1030–1069.
- Sangiorgio, B., Bozin, E. S., Malliakas, C. D., Fechner, M., Simonov, A., Kanatzidis, M. G., Billinge, S. J. L., Spaldin, N. A. and Weber, T. (2018). *Phys. Rev. Mater.* **2**(8), 085402.
- Sayre, D. (1951). *Acta Cryst.* **4**(4), 362–367.
- Schmidt, G. M. J. (1971). *Pure Appl. Chem.* **27**(4).
- Schomaker, V., Trueblood, K. N. and IUCr (1968). *Acta Crystallogr. B*, **24**(1), 63–76.
- Servalli, M., Öttinger, H. C. and Schlüter, A. D. (2018). *Phys. Today*, **71**(5), 40–47.
- Servalli, M. and Schlüter, A. D. (2017). *Annu. Rev. Mater. Res.* **47**(1), 361–389.
- Servalli, M., Trapp, N., Solar, M. and Schlüter, A. D. (2017). *Cryst. Growth. Des.* p. acs.cgd.7b00367.
- Sheldrick, G. M. (2015). *Acta Crystallogr. C*, **71**(1), 3–8.
- Simonov, A., (2016). Density Viewer. <https://github.com/aglie/DensityViewer>.
- Simonov, A., (2017). Meerkat. <https://github.com/aglie/meerkat>.
- Simonov, A., Weber, T. and Steurer, W. (2014a). *J. Appl. Crystallogr.* **47**(6), 2011–2018.
- Simonov, A., Weber, T. and Steurer, W. (2014b). *J. Appl. Crystallogr.* **47**(3), 1146–1152.
- Simonov, A., Weber, T. and Steurer, W., (2014c). Yell reference. <https://github.com/YellProgram/Yell>.
- Spek, A. L. (2003). *J. Appl. Crystallogr.* **36**(1), 7–13.
- Spek, A. L. (2009). *Acta Crystallogr. D*, **65**(2), 148–155.
- Staudinger, H. (1920). *Ber. Dtsch. Chem, Ges.* **53**(6), 1073–1085.
- Stepito, R. F. (2009). *Pure Appl. Chem.* **81**(2), 351–353.

- Storn, R. and Price, K. V. (1997). *J. Global Optimization*, **11**(4), 341–359.
- Sun, A. (2006). *Science*, **312**(5776), 1030–1034.
- Tanner, P., Maier, G. and Schlüter, A. D. (2018). *Helv. Chim. Acta*, **101**(10), e1800128.
- Ten Eyck, L. F. (1977). *Acta Crystallogr. A*, **33**(3), 486–492.
- Trueblood, K. N., Bürgi, H. B., Burzlaff, H., Dunitz, J. D., Gramaccioni, C. M., Schulz, H. H., Shmueli, U., Abrahams, S. C. and IUCr (1996). *Acta Crystallogr. A*, **52**(5), 770–781.
- Van Der Walt, S., Colbert, S. C. and Varoquaux, G. (2011). *Comput. Sci. Eng.* **13**(2), 22.
- Volker, P., (2015). Albula Viewer. <https://www.dectris.com/products/albula-software>.
- Waller, I. (1923). *Z. Phys. A - Hadron Nucl.* **17**(1), 398–408.
- Waller, P. J., Gándara, F. and Yaghi, O. M. (2015). *Acc. Chem. Res.* **48**(12), 3053–3063.
- Wang, L., Boutilier, M. S. H., Kidambi, P. R., Jang, D., Hadjiconstantinou, N. G. and Karnik, R. (2017). *Nat. Nanotech.* **12**(6), 509–522.
- Wang, W. and Schlüter, A. D. (2018). *Macromol. Rap. Commun.* **40**(1), 1800719–29.
- Warren, B. E., Averbach, B. L. and Roberts, B. W. (1951). *J. Appl. Phys.* **22**(12), 1493–1496.
- Weber, T. and Simonov, A. (2012). *Z. Krist.* **227**(5), 238–247.
- Wegner, G. (1971). *Macromol. Chem. Phys.* **145**(1), 85–94.
- Welberry, T. R. (1985). *Rep. Prog. Phys.* **48**(1), 1543–1594.
- Welberry, T. R. and Butler, B. D. (1994). *J. Appl. Crystallogr.* **27**(3), 205–231.
- Welberry, T. R. and Weber, T. (2015). *Crystallogr. Rev.* **22**(1), 2–78.
- Welberry, T. R. and Withers, R. L. (1991). *J. Appl. Crystallogr.* **24**(1), 18–29.
- Xiang, Z., Cao, D. and Dai, L. (2015). *Polym. Chem.* **6**(11), 1896–1911.
- Yang, F., Cheng, S., Zhang, X., Ren, X., Li, R., Dong, H. and Hu, W. (2017). *Adv. Mat.* **102**, 1702415.

- Young, C. A. and Goodwin, A. L. (2011). *J. Mater. Chem.* **21**(18), 6464–6476.
- Zhang, X.-L., Wang, L., Chen, L., Ma, X.-Y. and Xu, H.-X. (2018). *Chin. J. Polym. Sci.* **37**(2), 101–114.
- Zhao, Y., Bernitzky, R. H. M., Kory, M. J., Hofer, G., Hofkens, J. and Schlüter, A. D. (2016). *J. Am. Chem. Soc.* **138**(28), 8976–8981.
- Zheng, Z., Grönker, R. and Feng, X. (2016). *Adv. Mater.* **28**(31), 6529–6545.
- Zhu, J., Yang, C., Lu, C., Zhang, F., Yuan, Z. and Zhuang, X. (2018). *Acc. Chem. Res.* **51**(12), 3191–3202.
- Zhuang, X., Zhao, W., Zhang, F., Cao, Y., Liu, F., Bi, S. and Feng, X. (2016). *Polym. Chem.* **7**(25), 4176–4181.
- Zucker, U. H. and Schulz, H. (1982). *Acta Crystallogr. A*, **38**(3), 563–568.

10 Appendix

Attempts to recover the U^{AB} -matrix

This section provides additional context for *Section 4.4.5* and uses the same terminology and formula symbols. The failed attempts to recover the complete U^{AB} matrix are briefly summarized in the following paragraphs. Two additional tensors were introduced. The first is the tensor V

$$V = \begin{bmatrix} U^A & U^{AB} \\ U^{ABT} & U^B \end{bmatrix} \quad (10.1)$$

which describes the displacement between moiety A and B . The second tensor is the S tensor described by

$$S = \begin{bmatrix} U^A & S^{AB} \\ S^{ABT} & U^B \end{bmatrix} \quad (10.2)$$

with S^{AB} obtained from *Equation 4.4*. S and V are positive semi-definite and symmetric. Eigenvector and eigenvalue properties of S , V and U^{AB} were investigated and while no useful information for the problem at hand was gained it was observed that $U_{ij}^{AB} = U_{ji}^{AB}$ maximizes the smallest eigenvalue of U^{AB} . Properties of positive semi-definite matrices were investigated (Bhatia, 2007), with the Cholesky decomposition (Higham, 1990) being one of the most promising examples but yielded no further insights. Finally, the parity of the off-diagonal elements (Charles *et al.*, 2013) was investigated, but that approach was also unsuccessful.

Visualizations of different growth mechanisms

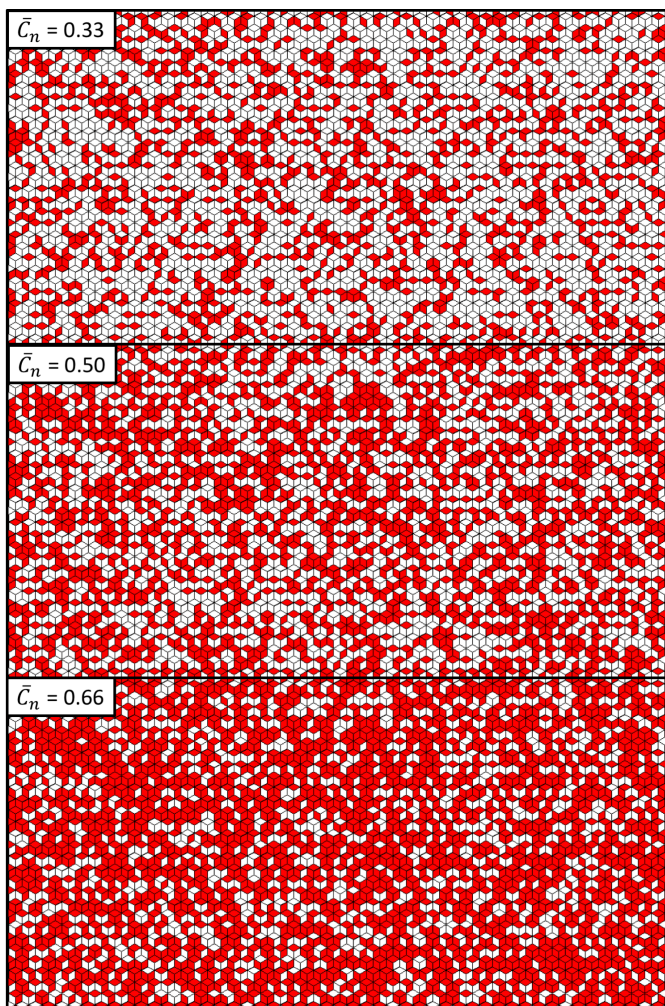


Figure 10.1: Selected intermediate states of the simulated unchanged reactivity model. The reactivity modifiers are $r_1 = 0.50$, $r_2 = 0.50$, $r_3 = 0.50$, and $r_4 = 0.50$. Details on the calculations are given in *Section 6.1.2* and *Section 6.2.2*.

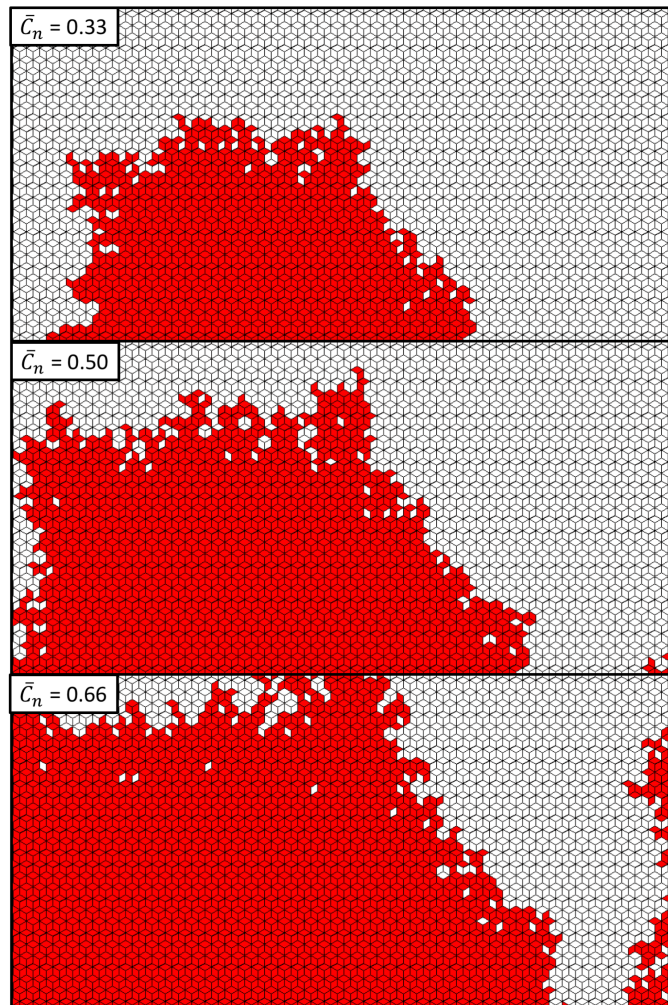


Figure 10.2: Selected intermediate states of the simulated enhanced reactivity model. The reactivity modifiers are $r_1 = 1.00$, $r_2 = 0.00$, $r_3 = 0.00$, and $r_4 = 0.00$. Details on the calculations are given in *Section 6.1.2* and *Section 6.2.2*.

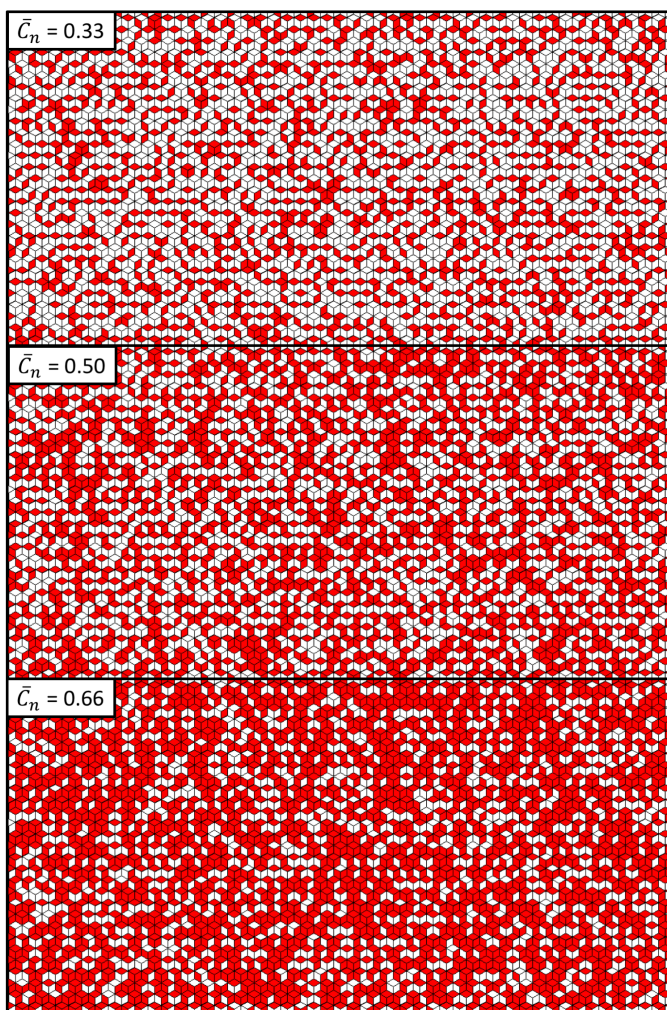


Figure 10.3: Selected intermediate states of the simulated partially reduced reactivity model. The reactivity modifiers are $r_1 = 0.15$, $r_2 = 0.50$, $r_3 = 0.50$, and $r_4 = 0.50$. Details on the calculations are given in *Section 6.1.2* and *Section 6.2.2*.

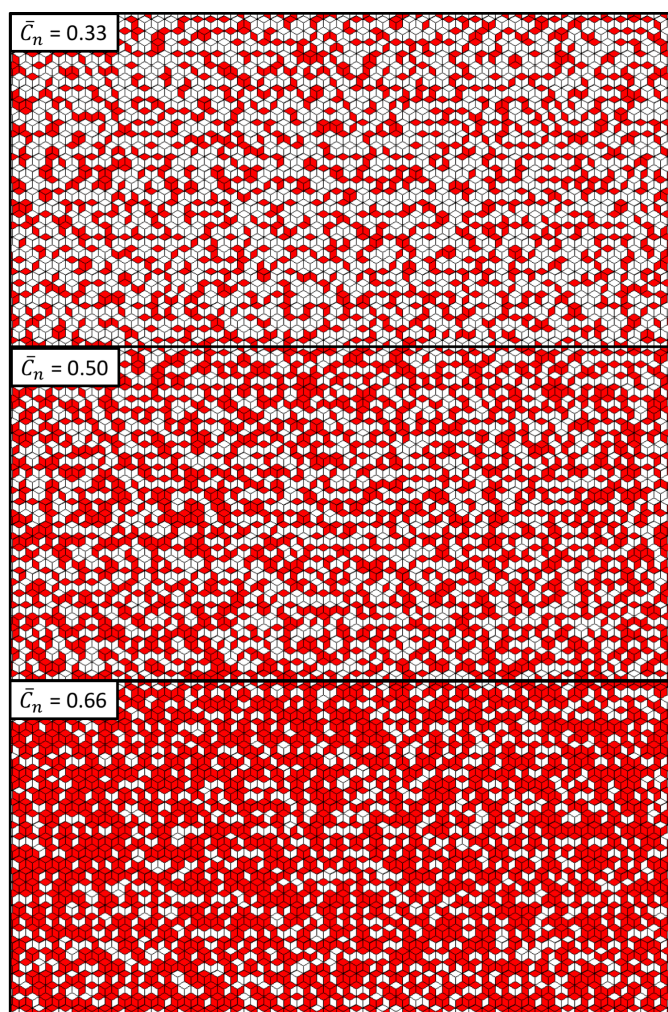


Figure 10.4: Selected intermediate states of the simulated repulsive growth mechanism as obtained from the diffuse scattering. The reactivity modifiers are $r_1 = 0.31$, $r_2 = 0.17$, $r_3 = 0.28$, and $r_4 = 0.55$. Details on the calculations are given in *Section 6.1.2* and *Section 6.2.2*.

Correlation tables

The following pages provide extensive tables about all first-neighbor displacive correlations. *Figure 10.5* explains the symbols used in these tables.

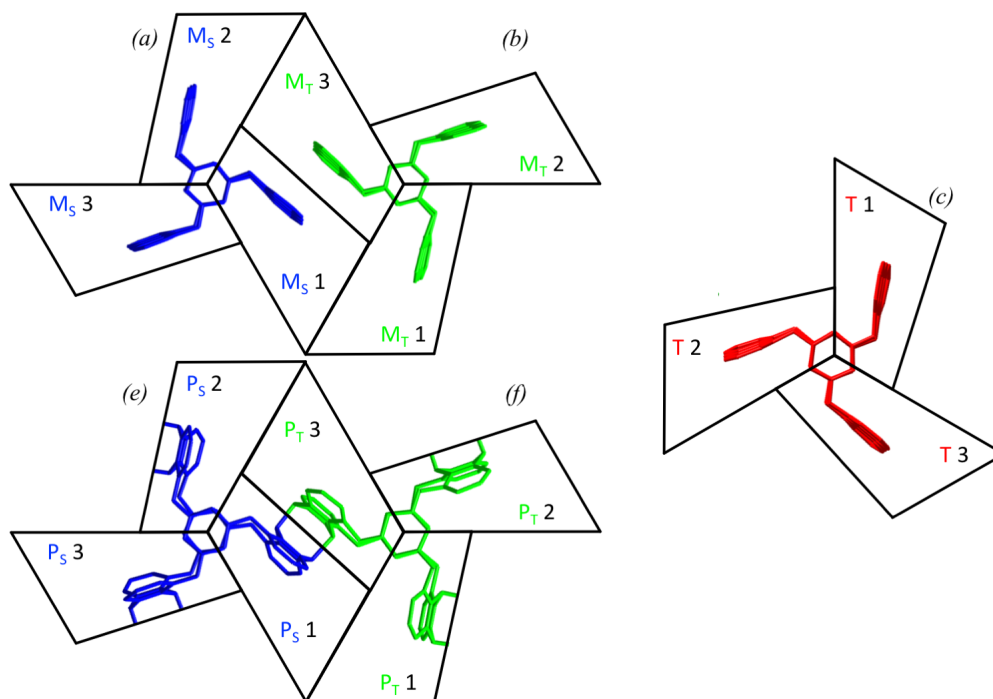


Figure 10.5: Fragments of (a,b) the monomer molecules, (c) the template and (e,f) polymerized molecules and their designations as used in *Table 10.1* to *Table 10.5*.

Fragments	cor_{11}^{AB}	cor_{22}^{AB}	cor_{33}^{AB}	cor_{12}^{AB}	cor_{23}^{AB}	cor_{31}^{AB}
M_S 1 - M_T 1	+ 0.18	+ 0.46	+ 0.32	-0.08	+ 0.02	-0.03
M_S 1 - M_T 2	+ 0.11	+ 0.53	+ 0.69	+ 0.25	0.00	-0.08
M_S 1 - M_T 3	+ 0.21	+ 0.39	+ 0.31	+ 0.20	-0.10	-0.08
M_S 1 - T 1	+ 0.08	+ 0.16	+ 0.31	+ 0.03	+ 0.01	+ 0.02
M_S 1 - T 2	-0.08	+ 0.27	+ 0.52	+ 0.02	-0.04	-0.04
M_S 1 - T 3	+ 0.44	+ 0.09	+ 0.26	+ 0.12	+ 0.01	+ 0.03
M_T 1 - T 1	+ 0.03	-0.15	+ 0.29	-0.01	-0.03	0.00
M_T 1 - T 2	+ 0.06	+ 0.09	+ 0.30	+ 0.04	+ 0.02	-0.06
M_T 1 - T 3	+ 0.02	+ 0.11	+ 0.17	+ 0.05	-0.06	+ 0.02

Table 10.1: Correlations between the first nearest neighbor molecules within the columns in the monomer crystal.

Fragments	cor_{11}^{AB}	cor_{22}^{AB}	cor_{33}^{AB}	cor_{12}^{AB}	cor_{23}^{AB}	cor_{31}^{AB}	Fragments	cor_{11}^{AB}	cor_{22}^{AB}	cor_{33}^{AB}	cor_{12}^{AB}	cor_{23}^{AB}	cor_{31}^{AB}
$M_S 1 - M_T 1$	-0.17	-0.03	+0.76	-0.38	+0.05	+0.11	$M_S 1 - M_T 1$	+0.20	+0.55	+0.34	-0.33	-0.04	+0.08
$M_S 1 - M_T 2$	-0.47	+0.71	+0.43	+0.02	+0.07	-0.05	$M_S 1 - M_T 2$	-0.64	+0.80	+0.91	+0.17	+0.13	+0.20
$M_S 1 - M_T 3$	+0.12	+0.40	+0.44	+0.20	-0.09	-0.10	$M_S 1 - M_T 3$	+0.23	+0.45	+0.34	+0.19	-0.08	-0.04
$P_S 1 - P_T 1$	-0.67	-0.65	-0.82	-0.03	+0.36	+0.26	$P_S 1 - P_T 1$	-0.29	-0.03	+0.52	-0.29	+0.30	+0.35
$P_S 1 - P_T 2$	-0.50	-0.65	-0.51	-0.02	-0.39	+0.15	$P_S 1 - P_T 2$	+0.20	+0.02	+0.48	+0.39	-0.23	+0.31
$P_S 1 - P_T 3$	-0.41	-0.49	-0.43	-0.34	+0.28	+0.37	$P_S 1 - P_T 3$	-0.32	-0.09	+0.20	-0.37	-0.03	+0.10
$M_S 1 - P_T 1$	-0.75	-0.05	+0.48	+0.27	-0.22	+0.17	$M_S 1 - P_T 1$	-0.10	+0.58	+0.16	+0.43	-0.42	+0.36
$M_S 1 - P_T 2$	+0.55	-0.16	+0.39	+0.39	-0.42	0.43	$M_S 1 - P_T 2$	+0.73	-0.57	-0.06	-0.03	-0.30	-0.17
$M_S 1 - P_T 3$	+0.55	-0.68	+0.52	-0.06	-0.05	-0.35	$M_S 1 - P_T 3$	+0.41	-0.28	-0.14	+0.12	-0.29	-0.39
$P_S 1 - M_T 1$	+0.13	+0.25	+0.95	-0.27	-0.05	-0.05	$P_S 1 - M_T 1$	+0.37	+0.35	+0.57	+0.32	-0.32	-0.36
$P_S 1 - M_T 2$	-0.79	+0.51	+0.34	-0.40	+0.43	+0.24	$P_S 1 - M_T 2$	-0.23	+0.77	+0.68	-0.21	+0.18	+0.31
$P_S 1 - M_T 3$	-0.65	+0.73	+0.85	-0.07	-0.05	+0.08	$P_S 1 - M_T 3$	-0.45	+0.18	+0.57	-0.09	-0.09	-0.06
$M_S 1 - T 1$	+0.10	+0.11	+0.50	+0.04	+0.03	-0.02	$M_S 1 - T 1$	+0.03	+0.13	+0.56	+0.07	+0.05	+0.01
$M_S 1 - T 2$	-0.45	+0.22	+0.65	-0.20	-0.05	-0.04	$M_S 1 - T 2$	-0.49	+0.07	+0.76	-0.30	-0.10	-0.13
$M_S 1 - T 3$	+0.39	+0.09	+0.42	+0.18	+0.07	+0.09	$M_S 1 - T 3$	+0.33	-0.08	+0.55	+0.16	+0.05	+0.09
$P_S 1 - T 1$	+0.33	-0.15	+0.86	+0.19	+0.16	-0.04	$P_S 1 - T 1$	-0.01	+0.11	+0.88	+0.22	+0.26	0.00
$P_S 1 - T 2$	+0.33	+0.37	+0.89	+0.38	-0.06	+0.02	$P_S 1 - T 2$	+0.06	+0.31	+0.93	+0.25	-0.15	-0.09
$P_S 1 - T 3$	+0.18	+0.44	+0.55	+0.04	+0.20	+0.02	$P_S 1 - T 3$	-0.01	+0.15	+0.65	-0.06	+0.18	+0.07
$M_T 1 - T 1$	-0.05	-0.28	+0.39	+0.06	+0.04	-0.05	$M_T 1 - T 1$	-0.23	-0.30	+0.42	+0.13	+0.06	-0.02
$M_T 1 - T 2$	+0.02	+0.06	+0.23	-0.02	+0.01	-0.10	$M_T 1 - T 2$	-0.11	+0.03	+0.43	-0.06	-0.01	-0.13
$M_T 1 - T 3$	+0.05	-0.01	+0.25	+0.03	-0.07	0.00	$M_T 1 - T 3$	+0.02	-0.15	+0.23	-0.07	-0.11	-0.01
$P_T 1 - T 1$	+0.21	+0.36	-0.07	+0.04	-0.06	-0.33	$P_T 1 - T 1$	-0.13	-0.00	+0.20	-0.36	-0.14	-0.43
$P_T 1 - T 2$	+0.23	+0.14	+0.22	+0.44	+0.04	0.00	$P_T 1 - T 2$	-0.03	+0.04	+0.39	+0.16	+0.07	-0.09
$P_T 1 - T 3$	-0.59	+0.30	+0.14	+0.40	-0.02	-0.44	$P_T 1 - T 3$	-0.27	-0.01	+0.35	+0.06	-0.07	-0.13

Table 10.2: Correlations between the first nearest neighbor molecules within the column in the partially polymerized structure. Left half of the table refers to a conversion ratio of 0.22 and the right half to a conversion ratio of 0.44.

Fragments	cor_{11}^{AB}	cor_{22}^{AB}	cor_{33}^{AB}	cor_{12}^{AB}	cor_{23}^{AB}	cor_{31}^{AB}
$M_S 1 - M_T 1$	+ 0.46	+ 0.69	+ 0.25	+ 0.28	-0.08	-0.16
$M_S 1 - M_T 2$	+ 0.09	+ 0.17	+ 0.08	-0.15	-0.04	-0.01
$M_S 1 - M_T 3$	+ 0.43	+ 0.36	+ 0.38	-0.11	-0.08	-0.04
$M_S 2 - M_T 1$	+ 0.16	+ 0.24	+ 0.08	+ 0.15	+ 0.03	+ 0.01
$M_S 2 - M_T 2$	+ 0.11	+ 0.07	+ 0.11	0.00	-0.05	-0.02
$M_S 2 - M_T 3$	0.00	-0.08	+ 0.25	-0.04	+ 0.12	+ 0.17
$M_S 3 - M_T 1$	+ 0.08	+ 0.24	+ 0.13	+ 0.05	+ 0.08	-0.00
$M_S 3 - M_T 2$	+ 0.11	+ 0.19	+ 0.05	+ 0.03	-0.01	-0.01
$M_S 3 - M_T 3$	+ 0.03	+ 0.51	+ 0.10	+ 0.15	-0.01	+ 0.04
$M_T 1 - T 1$	+ 0.73	+ 0.21	+ 0.33	+ 0.34	-0.02	+ 0.05
$M_T 1 - T 2$	+ 0.10	+ 0.17	+ 0.16	+ 0.09	-0.00	-0.01
$M_T 1 - T 3$	+ 0.34	+ 0.09	+ 0.05	+ 0.10	+ 0.04	+ 0.04
$M_T 2 - T 1$	+ 0.27	+ 0.17	+ 0.12	+ 0.17	0.00	+ 0.05
$M_T 2 - T 2$	+ 0.14	+ 0.11	+ 0.16	-0.02	-0.03	-0.03
$M_T 2 - T 3$	+ 0.13	+ 0.21	+ 0.10	+ 0.08	+ 0.03	+ 0.08
$M_T 3 - T 1$	+ 0.08	+ 0.19	+ 0.11	+ 0.07	+ 0.04	+ 0.05
$M_T 3 - T 2$	+ 0.07	+ 0.10	+ 0.07	+ 0.04	-0.02	-0.00
$M_T 3 - T 3$	+ 0.02	+ 0.19	+ 0.21	+ 0.06	-0.02	+ 0.01
$T 1 - M_S 1$	+ 0.83	+ 0.70	+ 0.35	+ 0.06	+ 0.02	+ 0.03
$T 1 - M_S 2$	+ 0.10	+ 0.23	+ 0.09	+ 0.05	-0.02	+ 0.04
$T 1 - M_S 3$	+ 0.20	+ 0.03	+ 0.16	-0.14	+ 0.15	+ 0.15
$T 2 - M_S 1$	+ 0.15	+ 0.33	+ 0.12	+ 0.18	-0.02	-0.02
$T 2 - M_S 2$	+ 0.43	+ 0.56	+ 0.11	+ 0.23	-0.06	+ 0.04
$T 2 - M_S 3$	-0.00	+ 0.34	+ 0.17	+ 0.12	0.00	+ 0.01
$T 3 - M_S 1$	+ 0.16	+ 0.20	0.00	+ 0.13	0.00	-0.01
$T 3 - M_S 2$	+ 0.14	+ 0.26	+ 0.15	+ 0.17	-0.01	+ 0.02
$T 3 - M_S 3$	+ 0.19	+ 0.25	+ 0.13	+ 0.07	0.00	-0.01

Table 10.3: Correlations between the first nearest neighbor molecules within the layer in the monomer crystal.

10. Appendix: Correlation tables

Fragments	cor_{11}^{AB}	cor_{22}^{AB}	cor_{33}^{AB}	cor_{12}^{AB}	cor_{23}^{AB}	cor_{31}^{AB}	Fragments	cor_{11}^{AB}	cor_{22}^{AB}	cor_{33}^{AB}	cor_{12}^{AB}	cor_{23}^{AB}	cor_{31}^{AB}
$M_S 1 - M_T 1$	+0.54	+0.92	+0.17	+0.40	+0.05	-0.12	$T 1 - M_S 1$	+0.38	+0.30	+0.16	+0.14	-0.05	+0.01
$M_S 1 - M_T 2$	+0.22	+0.04	-0.28	-0.13	-0.35	-0.13	$T 1 - M_S 2$	+0.29	+0.30	+0.02	+0.19	+0.04	+0.06
$M_S 1 - M_T 3$	+0.29	+0.48	+0.44	-0.19	-0.12	-0.06	$T 1 - M_S 3$	+0.44	+0.23	+0.13	+0.19	-0.04	+0.09
$M_S 2 - M_T 1$	+0.19	+0.26	+0.09	+0.16	+0.03	-0.03	$T 2 - M_S 1$	+0.02	+0.30	+0.05	+0.09	+0.02	-0.02
$M_S 2 - M_T 2$	-0.03	-0.17	+0.15	-0.27	-0.20	-0.07	$T 2 - M_S 2$	+0.41	+0.52	+0.07	+0.42	-0.10	+0.04
$M_S 2 - M_T 3$	-0.26	-0.42	+0.43	-0.45	+0.07	+0.13	$T 2 - M_S 3$	-0.10	+0.43	+0.16	+0.10	-0.03	-0.00
$M_S 3 - M_T 1$	+0.25	+0.35	+0.09	+0.38	+0.21	0.00	$T 3 - M_S 1$	+0.10	+0.28	+0.02	+0.17	+0.03	+0.01
$M_S 3 - M_T 2$	+0.15	+0.21	+0.07	+0.08	-0.03	-0.00	$T 3 - M_S 2$	+0.19	+0.22	+0.09	+0.13	+0.01	+0.02
$M_S 3 - M_T 3$	-0.04	+0.82	+0.41	+0.28	+0.11	+0.04	$T 3 - M_S 3$	+0.19	+0.30	+0.13	+0.17	+0.01	-0.01
$P_S 1 - P_T 1$	+0.68	-0.02	+0.45	-0.21	-0.11	-0.22	$T 1 - P_S 1$	+0.71	+0.82	+0.53	+0.11	+0.12	+0.09
$P_S 1 - P_T 2$	+0.53	+0.78	+0.13	+0.08	-0.00	-0.32	$T 1 - P_S 2$	-0.08	+0.30	+0.48	+0.11	-0.11	+0.01
$P_S 1 - P_T 3$	+0.91	+0.98	+0.85	+0.37	+0.03	-0.29	$T 1 - P_S 3$	-0.27	+0.79	+0.45	+0.21	+0.12	-0.18
$P_S 2 - P_T 1$	+0.31	+0.42	-0.24	+0.28	-0.01	+0.44	$T 2 - P_S 1$	-0.07	+0.15	+0.44	+0.12	-0.00	+0.14
$P_S 2 - P_T 2$	+0.19	+0.23	-0.22	+0.13	-0.39	-0.11	$T 2 - P_S 2$	+0.09	+0.83	+0.35	+0.47	+0.32	-0.10
$P_S 2 - P_T 3$	+0.44	-0.16	+0.04	-0.36	-0.39	+0.06	$T 2 - P_S 3$	+0.28	-0.09	-0.35	+0.05	+0.38	+0.20
$P_S 3 - P_T 1$	+0.31	+0.39	+0.04	+0.11	+0.04	-0.17	$T 3 - P_S 1$	+0.10	+0.31	+0.21	+0.11	+0.13	-0.01
$P_S 3 - P_T 2$	+0.21	+0.06	-0.21	-0.06	+0.11	-0.12	$T 3 - P_S 2$	+0.02	+0.66	+0.49	+0.35	+0.08	+0.02
$P_S 3 - P_T 3$	+0.54	+0.76	-0.19	+0.24	-0.44	-0.26	$T 3 - P_S 3$	+0.26	+0.16	+0.13	+0.08	-0.04	-0.02
$M_T 1 - T 1$	+0.83	+0.21	+0.40	+0.05	+0.03	+0.11	$M_S 1 - P_T 1$	+0.66	+0.75	-0.41	+0.39	-0.29	-0.23
$M_T 1 - T 2$	+0.10	+0.24	+0.10	+0.08	-0.04	-0.01	$M_S 1 - P_T 2$	-0.37	+0.41	-0.48	-0.15	-0.45	-0.31
$M_T 1 - T 3$	+0.54	-0.08	+0.02	+0.01	+0.13	+0.13	$M_S 1 - P_T 3$	—	—	—	—	—	—
$M_T 2 - T 1$	+0.29	+0.23	0.00	+0.20	-0.02	+0.03	$M_S 2 - P_T 1$	+0.20	-0.40	-0.22	-0.27	+0.11	-0.13
$M_T 2 - T 2$	+0.26	-0.09	+0.18	-0.08	+0.02	+0.06	$M_S 2 - P_T 2$	+0.54	+0.02	-0.11	+0.18	-0.33	-0.17
$M_T 2 - T 3$	+0.73	+0.23	+0.34	+0.44	-0.02	+0.05	$M_S 2 - P_T 3$	+0.12	+0.55	+0.52	+0.35	-0.12	-0.29
$M_T 3 - T 1$	+0.07	+0.13	+0.11	+0.03	+0.03	+0.02	$M_S 3 - P_T 1$	+0.25	+0.31	+0.02	+0.12	-0.19	-0.17
$M_T 3 - T 2$	+0.08	+0.08	+0.08	+0.04	-0.00	+0.03	$M_S 3 - P_T 2$	-0.05	+0.52	-0.08	+0.29	-0.34	-0.15
$M_T 3 - T 3$	+0.21	+0.11	+0.28	+0.06	-0.06	-0.09	$M_S 3 - P_T 3$	+0.04	-0.42	-0.05	+0.04	-0.35	+0.03
$P_T 1 - T 1$	+0.73	+0.50	+0.78	+0.19	+0.02	-0.16	$P_S 1 - M_T 1$	+0.04	+0.09	-0.47	+0.46	-0.19	+0.19
$P_T 1 - T 2$	+0.37	+0.60	-0.27	+0.16	+0.06	+0.21	$P_S 1 - M_T 2$	+0.20	+0.09	+0.60	+0.47	-0.22	-0.20
$P_T 1 - T 3$	-0.22	+0.31	+0.72	-0.30	+0.03	-0.16	$P_S 1 - M_T 3$	—	—	—	—	—	—
$P_T 2 - T 1$	+0.09	+0.30	+0.28	+0.18	+0.13	+0.26	$P_S 2 - M_T 1$	+0.19	+0.54	+0.34	+0.43	-0.10	-0.08
$P_T 2 - T 2$	+0.60	+0.07	+0.17	+0.45	+0.01	+0.25	$P_S 2 - M_T 2$	+0.07	-0.19	+0.29	+0.11	-0.18	-0.09
$P_T 2 - T 3$	+0.83	+0.55	+0.75	+0.40	+0.13	+0.26	$P_S 2 - M_T 3$	+0.24	+0.11	-0.43	-0.00	+0.30	-0.07
$P_T 3 - T 1$	+0.52	+0.36	-0.00	+0.24	+0.13	+0.18	$P_S 3 - M_T 1$	-0.32	+0.52	+0.27	-0.03	+0.03	-0.32
$P_T 3 - T 2$	+0.25	+0.16	+0.20	+0.07	+0.09	+0.16	$P_S 3 - M_T 2$	+0.32	-0.18	+0.10	-0.05	+0.01	+0.05
$P_T 3 - T 3$	0.00	-0.15	+0.53	+0.12	+0.14	+0.03	$P_S 3 - M_T 3$	-0.24	-0.34	-0.41	-0.05	-0.31	+0.44

Table 10.4: Correlations between the first nearest neighbor molecules within the layer in the partially polymerized structure with a conversion ratio of 0.22.

Fragments	cor_{11}^{AB}	cor_{22}^{AB}	cor_{33}^{AB}	cor_{12}^{AB}	cor_{23}^{AB}	cor_{31}^{AB}	Fragments	cor_{11}^{AB}	cor_{22}^{AB}	cor_{33}^{AB}	cor_{12}^{AB}	cor_{23}^{AB}	cor_{31}^{AB}
$M_S 1 - M_T 1$	+0.63	+0.74	+0.46	+0.42	+0.07	+0.07	$T 1 - M_S 1$	+0.31	+0.29	+0.17	+0.19	-0.01	+0.13
$M_S 1 - M_T 2$	+0.12	-0.23	+0.18	-0.03	-0.29	-0.05	$T 1 - M_S 2$	+0.20	+0.24	+0.20	+0.15	+0.03	+0.08
$M_S 1 - M_T 3$	+0.24	+0.83	+0.66	+0.12	-0.04	-0.05	$T 1 - M_S 3$	+0.12	+0.19	+0.18	+0.08	-0.08	-0.00
$M_S 2 - M_T 1$	+0.10	+0.29	-0.01	+0.14	+0.10	+0.01	$T 2 - M_S 1$	+0.02	+0.20	+0.06	+0.04	+0.01	-0.01
$M_S 2 - M_T 2$	-0.24	+0.13	+0.66	-0.15	-0.12	-0.16	$T 2 - M_S 2$	+0.35	+0.53	-0.05	+0.42	-0.18	+0.08
$M_S 2 - M_T 3$	-0.50	-0.58	+0.27	-0.42	-0.26	-0.06	$T 2 - M_S 3$	-0.11	+0.14	+0.29	-0.11	-0.06	-0.09
$M_S 3 - M_T 1$	+0.08	+0.45	-0.10	+0.42	+0.05	+0.20	$T 3 - M_S 1$	+0.09	+0.33	+0.05	+0.15	-0.04	+0.04
$M_S 3 - M_T 2$	-0.13	+0.11	+0.66	-0.41	-0.12	-0.05	$T 3 - M_S 2$	+0.17	+0.22	+0.16	+0.10	0.00	+0.08
$M_S 3 - M_T 3$	-0.53	+0.56	+0.48	-0.05	+0.20	+0.28	$T 3 - M_S 3$	+0.15	+0.18	+0.21	+0.07	-0.03	+0.04
$P_S 1 - P_T 1$	+0.02	+0.53	+0.71	+0.09	+0.01	-0.18	$T 1 - P_S 1$	+0.50	+0.59	+0.43	+0.09	-0.02	-0.16
$P_S 1 - P_T 2$	+0.31	+0.92	+0.06	+0.35	+0.29	-0.05	$T 1 - P_S 2$	+0.27	+0.41	+0.29	+0.33	-0.01	-0.02
$P_S 1 - P_T 3$	+0.83	+0.89	+0.97	-0.07	-0.14	-0.08	$T 1 - P_S 3$	-0.06	+0.39	+0.30	+0.07	+0.08	+0.09
$P_S 2 - P_T 1$	+0.49	+0.39	+0.11	+0.36	-0.04	+0.12	$T 2 - P_S 1$	+0.02	+0.28	+0.25	+0.12	+0.06	+0.01
$P_S 2 - P_T 2$	-0.47	-0.19	-0.61	+0.34	-0.32	-0.18	$T 2 - P_S 2$	+0.38	+0.47	+0.35	+0.33	+0.13	-0.01
$P_S 2 - P_T 3$	+0.55	-0.54	-0.21	-0.10	-0.43	-0.07	$T 2 - P_S 3$	+0.26	+0.27	+0.04	+0.25	+0.24	+0.07
$P_S 3 - P_T 1$	+0.04	+0.83	+0.70	-0.05	-0.07	-0.20	$T 3 - P_S 1$	+0.08	+0.30	+0.06	+0.09	-0.01	-0.04
$P_S 3 - P_T 2$	+0.40	+0.39	+0.43	+0.13	-0.12	-0.22	$T 3 - P_S 2$	+0.11	+0.40	+0.40	+0.27	-0.06	+0.04
$P_S 3 - P_T 3$	+0.22	+0.15	+0.37	+0.36	-0.38	+0.27	$T 3 - P_S 3$	+0.06	+0.26	+0.04	-0.02	-0.11	-0.10
$M_T 1 - T 1$	+0.80	+0.37	+0.26	+0.32	-0.10	+0.16	$M_S 1 - P_T 1$	+0.78	+0.84	-0.12	+0.24	-0.23	-0.30
$M_T 1 - T 2$	+0.12	+0.18	+0.15	+0.14	-0.08	-0.06	$M_S 1 - P_T 2$	+0.35	+0.54	-0.05	+0.06	-0.04	-0.03
$M_T 1 - T 3$	+0.13	+0.18	+0.12	+0.08	+0.04	+0.08	$M_S 1 - P_T 3$	—	—	—	—	—	—
$M_T 2 - T 1$	+0.32	+0.24	-0.01	+0.23	0.00	+0.07	$M_S 2 - P_T 1$	+0.15	-0.58	+0.18	-0.42	-0.07	-0.25
$M_T 2 - T 2$	+0.24	-0.28	+0.07	-0.17	-0.09	-0.11	$M_S 2 - P_T 2$	+0.51	+0.34	+0.19	+0.32	-0.14	-0.13
$M_T 2 - T 3$	+0.48	-0.09	-0.11	-0.08	+0.06	+0.03	$M_S 2 - P_T 3$	+0.41	+0.94	+0.65	+0.27	-0.04	-0.07
$M_T 3 - T 1$	+0.24	+0.13	+0.02	+0.09	+0.06	+0.11	$M_S 3 - P_T 1$	+0.35	+0.41	0.00	+0.25	-0.06	-0.03
$M_T 3 - T 2$	+0.08	+0.02	+0.09	-0.01	-0.06	+0.01	$M_S 3 - P_T 2$	+0.03	+0.70	+0.01	+0.32	-0.10	-0.07
$M_T 3 - T 3$	-0.16	-0.08	+0.33	-0.18	-0.13	-0.08	$M_S 3 - P_T 3$	-0.10	+0.10	+0.65	+0.31	+0.09	+0.17
$P_T 1 - T 1$	+0.78	+0.75	+0.57	+0.34	+0.08	+0.14	$P_S 1 - M_T 1$	+0.62	+0.41	-0.46	+0.38	+0.38	+0.25
$P_T 1 - T 2$	+0.32	+0.25	+0.08	+0.14	+0.01	-0.03	$P_S 1 - M_T 2$	+0.63	+0.68	-0.46	+0.33	-0.14	-0.22
$P_T 1 - T 3$	+0.04	+0.46	+0.41	-0.04	+0.04	-0.03	$P_S 1 - M_T 3$	—	—	—	—	—	—
$P_T 2 - T 1$	+0.26	+0.04	+0.29	+0.11	+0.08	+0.13	$P_S 2 - M_T 1$	+0.21	+0.67	-0.06	+0.43	-0.11	-0.03
$P_T 2 - T 2$	+0.45	+0.26	+0.28	+0.43	+0.06	+0.10	$P_S 2 - M_T 2$	+0.30	-0.21	+0.07	-0.14	-0.19	-0.22
$P_T 2 - T 3$	+0.15	+0.27	+0.11	+0.13	+0.10	+0.07	$P_S 2 - M_T 3$	+0.30	-0.51	-0.49	-0.03	+0.37	-0.05
$P_T 3 - T 1$	+0.09	+0.26	+0.22	+0.07	+0.03	+0.05	$P_S 3 - M_T 1$	-0.16	+0.51	-0.05	-0.12	+0.02	-0.09
$P_T 3 - T 2$	+0.17	+0.03	+0.14	+0.04	+0.15	+0.03	$P_S 3 - M_T 2$	+0.10	-0.61	-0.01	-0.21	-0.20	-0.12
$P_T 3 - T 3$	+0.35	+0.27	+0.12	+0.24	+0.20	+0.04	$P_S 3 - M_T 3$	-0.48	+0.07	-0.43	-0.28	-0.17	-0.06

Table 10.5: Correlations between the first nearest neighbor molecules within the layer in the partially polymerized structure with a conversion ratio of 0.44.

Simulated development of substitutional correlations

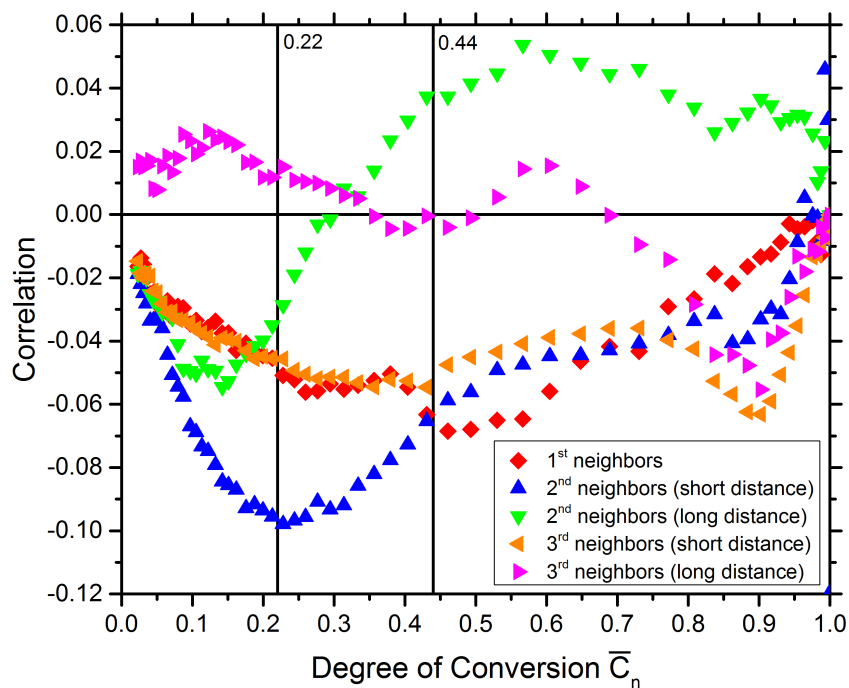


Figure 10.6: Simulated development of substitutional correlations within a polymer layer in different neighborhoods as obtained by DE minimization. Note that the minimization had only hard data at a \bar{C}_n of 0.22 and 0.44. Further details are given in *Section 6.2.2*.

List of Figures

2.1	Single crystal approach	7
2.2	Simple propagation models	11
3.1	Structure drawings of the monomer and solvent molecules	21
3.2	Average crystal structure	22
3.3	Construction of the rhombille tiling	26
3.4	Properties of the rhombille tiling	27
4.1	Possible crystal shapes	29
4.2	SEM and optical microscope image	30
4.3	Conceptual subdivision of molecules	41
4.4	Examples of possible blade pairings	45
4.5	Introduced substitutional correlation symmetry	47
5.1	Irradiation-time dependent conversion 100 K	51
5.2	Irradiation-time dependent conversion 293 K	52
5.3	Change in ADP during polymerization	53
5.4	Inter-molecular center-to-center distances at 100 K	54
5.5	Inter-molecular center-to-center distances at room temperature	55
5.6	Residual electron density during depolymerization	56
5.7	2cpy orientations	57
5.8	Reciprocal space reconstruction of the $hk0.2$ and $0kl$ section	60
5.8	Reciprocal space reconstruction of the $hk1.8$ and $hk3.2$ section	61
5.8	Reciprocal space reconstruction of the $hk5.6$ and $hk10.2$ section	62
5.8	Reciprocal space reconstruction of the $hk16.8$ and $hk17.4$ section	63
5.9	Reflection splitting in $CS1$	64
5.10	Diffuse scattering: best and average fit	66
5.10	Diffuse scattering: average and worst fit	67
5.11	PDF densities: typical fit	69
5.11	PDF densities: Best and worst fit	70
5.12	PDF densities: Outliers	71
5.13	Differentiation of displacive and substitutional disorder	72
5.14	Basic correlation models	78
5.15	Correlations from Yell	79
6.1	Solvent molecule mobility	81
6.2	Overexposed reciprocal space reconstruction	84
6.3	Avrami calculations	87
6.4	Anthracene - anthracene distance development	88

6.5	Selective polymerization changes correlations	91
6.6	Qualitative distribution of positive and negative correlations .	93
6.7	Quantitative correlations	94
6.8	Displacements caused by dimerization	95
8.1	Oligomers	105
8.2	Pentagonal tilings	106
8.3	Exploitable intermediate states during 2D polymerization . . .	107
10.1	Unchanged reactivity model	119
10.2	Enhanced reactivity model	120
10.3	Reduced reactivity model	121
10.4	Final reactivity model	122
10.5	Blade code for tables	123
10.6	Simulated development of correlations	129

List of Tables

4.1	Summary of used crystals	31
5.1	Refinement results — In-house experiments	49
5.2	Refinement results — Synchrotron experiments	50
5.3	Intra- and intermolecular correlations	74
5.4	blades and half-dimers in the column	75
5.5	Correlations between the template and pore walls	76
10.1	In-column correlations at conversion 0.00	124
10.2	In-column correlations at conversion 0.22	125
10.3	Inlayer correlations at conversion 0.00	126
10.4	Inlayer correlations at conversion 0.22	127
10.5	Inlayer correlations at conversion 0.44	128

Gregor Hofer

CONTACT INFORMATION	ETH Zürich Laboratory of Polymer Chemistry Vladimir-Prelog Weg 1-5/10 8093 Zürich, Switzerland	Voice: +41 446 336 679 E-mail: gregor.hofer@mat.ethz.ch
RESEARCH INTERESTS	Phase transformations, diffuse X-ray scattering, two-dimensional polymers, single-crystal diffraction, synchrotron radiation, high-pressure crystallography	
EDUCATION	Eidgenössische Technische Hochschule Zürich , Zürich, Switzerland Ph.D. student of crystallography and polymer chemistry, dissertation defense on 01.07.2019 <ul style="list-style-type: none">Thesis topic: "The two-dimensional polymerization mechanism of an anthracene based monomer: A single-crystal-to-single-crystal transformation investigated via total X-ray scattering." University of Vienna , Vienna, Austria M.Sc., mineralogy and crystallography, August, 2014 <ul style="list-style-type: none">Thesis topic: "Compressibility and high-pressure behavior of spodumene-type $\text{LiScGe}_2\text{O}_6$" University of Vienna , Vienna, Austria B.Sc., mineralogy and crystallography, September, 2012 <ul style="list-style-type: none">Thesis Topic: "Isothermale Kompressibilitätsmessung am Karbonat Norsethit, $\text{BaMg}(\text{CO}_3)_2$, durch Hochdruck in-situ Einkristallröntgendiffraktometrie"	
ACADEMIC EXPERIENCE	ETH Zürich , Zürich, Switzerland <i>Ph.D. Student</i> January, 2015 - present Includes current Ph.D. research, Ph.D. and Masters level coursework and research/consulting projects. X-ray Center , Vienna, Austria <i>Student trainee</i> June, 2013 - Oktober, 2014 Crystallographic service at the Vienna University of Technology, residual stress analysis and phase analysis of ongoing projects, supervision of users during their experiments University of Vienna , Vienna, Austria <i>Teaching Assistant</i> September, 2010 - February, 2014 Duties at various times have included reciting lectures with students, support of students and teachers during the lectures	
PUBLICATIONS	Müller, V., Schlüter, AD., Hinaut, A., Moradi, M., Baljovic, M., Jung, T.; Shahgaldian, P., Mhwald, H., Hofer, G., Kroeger, M., (2018) A twodimensional polymer synthesized at the air/water interface. <i>Angewandte Chemie International Edition</i> , 57, 33, 10584-10588 Hofer, G., Grieder, F., Kroeger, M., Schlüter, AD., Weber, T., (2018). Unraveling two-dimensional polymerization in the single crystal. <i>Journal of Applied Crystallography</i> , 51, 2, 481-497. Lange, R., Hofer, G., Weber, T., Schlüter, AD. (2017). A two-dimensional polymer synthesized through topochemical [2+ 2]-cycloaddition on the multigram scale. <i>Journal of the American Chemical Society</i> , 139, 5, 2053-2059. Beyer, H., Kory, M., Hofer, G., Stemmer, A., Schlüter, AD. (2017). Exfoliation of two-dimensional polymer single crystals into thin sheets and investigations of their surface structure by high-resolution atomic force microscopy. <i>Nanoscale</i> , 9, 27, 9481-9490.	

Zhao, Y., Bernitzky, R., Kory, M.,; Hofer, G.,; Hofkens, J., Schlüter, AD. (2016). Decorating the Edges of a 2D Polymer with a Fluorescence Label. *Journal of the American Chemical Society*, 138, 28, 8976-8981.

Hofer, G., Kuzel, J., Scheidl, K. S., Redhammer, G., and Miletich, R. (2015). High-pressure crystallography and compression behavior of the alkali-scandium-germanate end-members $\text{LiScGe}_2\text{O}_6$ and $\text{NaScGe}_2\text{O}_6$. *Journal of Solid State Chemistry*, 229, 188-196.

Pippinger, T., Miletich, R., Effenberger, H., Hofer, G., Lotti, P., and Merlini, M. (2014). High-pressure polymorphism and structural transitions of norsethite, $\text{BaMg}(\text{CO}_3)_2$. *Physics and Chemistry of Minerals*, 41(10), 737-755.

Miletich, R., Pippinger, T., Effenberger, H., Hofer, G., Lotti, P., and Merlini, M. (2014). Transformation pathways of structural transitions between $\text{BaMg}(\text{CO}_3)_2$ polymorphs. *Acta Cryst*, 70, C271.

INVITED TALKS

Employing real crystal structure analysis to understand two-dimensional polymerization. Department of Chemistry at the University of California. Berkeley, California, United States, August 2018.

Employing real crystal structure analysis to understand two-dimensional polymerization. University of Vienna, Topics in Crystallography and Mineralogy. Vienna, Austria, May 2018.

Two-Dimensional Polymers: From Monomer to Polymer Single-Crystals and Back. University of Technology Vienna, Seminar of the Institute of Materials Chemistry. Vienna, Austria, December, 2017.

Applications of the Pair Distribution Function in Crystallography, the Street Parade and Polymer Chemistry 30th European Crystallographic Meeting. Basel, Switzerland, August, 2017. *Science Slam presentation, awarded as the best presentation.*

ORAL PRESENTATIONS

Unraveling 2D polymerization: A topochemical reaction studied via total scattering 31st European Crystallographic Meeting Oviedo, Spain, August 2018

Two-Dimensional Polymers: From Monomer to Polymer Crystals and Back 24th Congress and General Assembly of the International Union of Crystallography Hyderabad, India, August 2017

The Reversible Single-Crystal-To-Single-Crystal Transformation of a 2D Polymer. 25th Annual meeting of the German Crystallographic Society. Karlsruhe, Germany, March, 2017.

Unraveling the Propagation of Two-Dimensional Polymerization. 2nd Conference on Two-Dimensional Polymers. Nara, Japan, June, 2016.

On the Mechanism and Accompanying Effects of Two-Dimensional Polymerization in a Novel Monolayered Monomer Crystal. 24th Annual meeting of the German Crystallographic Society. Stuttgart, Germany, March, 2016.

Intriguing Structural Features of a Novel Two-Dimensional Polymer. 23rd Conference on Applied Crystallography. Krynica, Poland, September, 2015.

Intriguing Structural Features of a Novel Two-Dimensional Polymer. 2nd STOE Lab Meeting. Darmstadt, Germany, September 2015.

Intriguing structural features of a novel two-dimensional polymer. 10th Materials and Processes

Graduate Symposium ETH Zürich. Zürich, Switzerland, June, 2015.

Polymer chemistry AND crystallography! In-house seminar of the polymer chemistry group. Zürich, Switzerland, May, 2015.

Calcite of Helgustadir. In-house seminar Institute of Mineralogy and Crystallography Vienna. Vienna, Austria, March, 2015.

Utilisation of phase transitions in earth sciences and polymer chemistry. In-house seminar Laboratory of Crystallography, ETH Zürich Zürich, Switzerland, February, 2015.

Public defense of master thesis. In-house seminar Institute of Mineralogy and Crystallography Vienna. Vienna, Austria, June, 2014.

Public defense of bachelor thesis. In-house seminar Institute of Mineralogy and Crystallography Vienna. Vienna, Austria, June, 2012.

POSTER
PRESENTATIONS

30th European Crystallographic Meeting Hysteresis of Two-Dimensional Polymerization and Depolymerization Basel, Switzerland, August, 2016.

24th Annual meeting of the German Crystallographic Society On the Mechanism and Accompanying Effects of Two-Dimensional Polymerization in a Novel Mono-Layered Monomer Crystal Stuttgart, Germany, March, 2016. *Received an award for the best poster*

2nd STOE Lab Meeting 11.09.2015, Darmstadt, Germany Intriguing Structural Features of a Novel Two-Dimensional Polymer Darmstadt, Germany, September 2015. *Received an award for the best poster*

ATTENDED
CONFERENCES

31st European Crystallographic Meeting Oviedo, Spain, August 2018

24th Congress and General Assembly of the International Union of Crystallography Hyderabad, India, August 2017

25th Annual meeting of the German Crystallographic Society Karlsruhe, Germany, March, 2017.

2nd Conference on Two-Dimensional Polymers. Nara, Japan, June, 2016.

30th European Crystallographic Meeting Basel, Switzerland, August, 2016.

24th Annual meeting of the German Crystallographic Society Stuttgart, Germany, March, 2016.

2nd STOE Lab Meeting 11.09.2015, Darmstadt, Germany Darmstadt, Germany, September 2015.

10th Materials and Processes Graduate Symposium ETH Zürich, Zürich, Switzerland, June, 2015.

SNBL Planning for the next decade, Grenoble, France, May, 2015.

Corals-2013: Raman and Luminescence Spectroscopy, Vienna, Austria, June, 2013.

29th Annual General Meeting of the Geological Society of Sri Lanka Kandy, Sri Lanka, February, 2013.

AWARDS

ECM30 Science Slam Award — Basel 2016

Best Poster — Stuttgart 2016

Best Poster — Darmstadt 2015

ATTENDED
WORKSHOPS

Analysis of Short Range Order, Vienna, Austria, March, 2015

Corals - 2013: Raman and Luminescence Spectroscopy, Vienna, Austria, June, 2013.

ADDITIONAL
WORKING
EXPERIENCES

German Crystallographic Society,
AK Young Crystallographers *Blog Author* **March 2015 - March 2018**
Researching and writing about topics of interest for Master Students, PhD Students and Post-Docs

R. Klinger Dichtungstechnik, Gumpoldskirchen, Austria *Summer intern* **2013, 2012, 2011**
Creating sample pieces with the means of a hydraulic press and calender, evaluation of sample pieces which were exposed to different physical and chemical conditions, creating resource and material reference samples under the microscope, supporting work in laboratory and pilot plant

Global2000, Vienna, Austria *Environmental representative* **March 2012 - March 2013**
Mentoring workshops and presenting current environmental issues

UNHCR, Rinkaby, Sweden *Workshop instructor* **August 2011**
Increasing situation awareness of refugees for teenagers

A. Kovar Sachverständigung, Vienna, Austria *Freelancer* **October 2010 - December 2010**
PC hardware repair and support

Austrian Post Office, Vienna, Austria *Summer intern* **June 2010 - September 2010**
Mail delivery

AComp, Vienna, Austria *Freelancer* **June 2009 - August 2009**
All kinds of programming work

A. Kovar Sachverständigung, Vienna, Austria *Freelancer* **January 2009 - March 2009**
PC hardware repair and support

AComp, Vienna, Austria *Freelancer* **August 2008 - November 2008**
All kinds of programming work

SPZ Schwarzringergasse, Vienna, Austria *Freelancer* **June 2009 - August 2009**
Regular civil service in a school for special needs

OMV, International oil and gas company, Vienna, Austria *Summer intern* **2006, 2005, 2004**
Database administration, network administration

SCIENTIFIC SKILLS

- Standard single-crystal diffraction (structure solution and refinement)
- Real crystal structure analysis via diffuse scattering and the 3D- Δ PDF Method
- Monte Carlo simulations
- Differential Evolution minimization
- Phase analysis using powder diffraction
- Stress and strain analysis with the $\sin^2\psi$ method

- COMPUTER SKILLS
- Different scientific software for single-crystal and powder diffraction measurements and their further evaluation, different kinds of kinds of crystal structure visualisation software, self programmed software for the evaluation of diffuse X-ray scattering
 - Languages: Python, Java, C#, C, Unix shell scripts, Delphi, C++(basics)
 - Parallel computing on clusters
 - Applications: common Windows applications such as MS Office, artistic 3D modeling, GIMP
 - Operating Systems: Mac OSX, Unix/Linux, Windows.